

ABSTRACT

Title of Document: MITIGATION SYSTEMS FOR CONFINED
BLAST LOADING – CREW PROTECTION IN
ARMORED VEHICLES.

Katherine Marie Gaulke, PhD, 2009

Directed By: Amde M. Amde, Professor, Department of Civil
and Environmental Engineering

Confined blast behavior and blast mitigation structures for the protection of occupants within a confined space subjected to high explosive blast, were examined through numerical analysis and laboratory testing. The mitigating structure's weight and geometry were of particular interest since performance was targeted for inclusion within the limited interior space of an armored vehicle. Numerical analysis using eta/VPG modeling software and LS DYNA dynamic analysis software examined the effects of blast mitigation compartments of varying geometries and dimensions for extremely close standoff distances for free field and confined blast events. Large 150 pound steel plates were used to occupy the confined space and examine occupant risk for head and chest acceleration injuries. Cylinders varied in wall thickness, diameter and shielding height. The energy absorption capability of these varying mitigation compartments produced counterintuitive results. Full scale laboratory tests of open ended cylindrical mitigation shields for free-field and confined blast correlation were

conducted. Numerical “blast-test” dummies are introduced and found to produce analogous results to the aforementioned steel plates for chest accelerations. This dummy study shows the potential and necessity for additional research into a valuable, more advanced FEA tool to evaluate human response to direct blast.

MITIGATION SYSTEMS FOR CONFINED BLAST LOADING – CREW
PROTECTION IN ARMORED VEHICLES.

By

Katherine Marie Gaulke

Dissertation submitted to the Faculty of the Graduate School of the
University of Maryland, College Park, in partial fulfillment
of the requirements for the degree of
Doctor of Philosophy
2009

Advisory Committee:
Professor Amde M Amde, Co-Chair
Professor William Fourney, Co-Chair
Professor Bilal Ayyub
Professor Ali Haghani
Dr. Rahul Gupta

© Copyright by
Katherine M Gaulke
2009

Preface

The views expressed in this article are those of the author and do not reflect the official policy or position of the United States Air Force, Department of Defense, or the U.S. Government.

Dedication

This research is dedicated to my fellow men and women in uniform and their families. Especially, to my father, my hero.

Acknowledgements

I would like to thank my advisor, Dr Amde M Amde, for his support and expertise. I would also like to thank my dissertation committee members and the United States Air Force for the opportunity to contribute to the field of structural engineering and protective technology.

Dr Rahul Gupta, Army Research Laboratory (ARL) Aberdeen Proving Ground, deserves much acknowledgment. His unwavering support, belief and indispensable knowledge made this research a reality. Rob Bitting generously shared his office and time in ensuring I was well equipped and well taken care of. I owe much gratitude to Dr Reed Skaggs, Dr Patrick Baker, Nora Eldredge, Dr Scott Kukuck, Dr Brendan McAndrew, Rachel Ehlers, Mike McFadden and Brian Michael and the entire staff of Terminal Effects Division at the Army Research Laboratory (ARL), Aberdeen Proving Ground, for making me at home and part of the ARL team. ARL's generous financial, laboratory and administrative support was vital to the success and completion of this research. I would like to thank the support teams of eta/VPG and LSTC for their assistance with my numerical analysis. In particular, Dr Ian Do and Dr Sarba Guha of LSTC, whose aid was the catalyst for timely progress.

I will never be able to adequately express my gratitude to my mom and dad. Their bravery, fortitude, faith, integrity, selflessness, love and generosity are unparalleled in this broken world. I am blessed to be your child.

To my husband and daughter, you are the greatest gifts ever given to me.

My Lord, all blessing flow from you; thank you for the many times you carried me during this journey.

Table of Contents

Preface.....	ii
Dedication.....	iii
Acknowledgements.....	iv
Table of Contents.....	vi
List of Tables.....	viii
List of Figures.....	ix
List of Abbreviations.....	xi
Chapter 1: Introduction.....	12
1.1 Problem Statement.....	12
1.2 Purpose of Study.....	12
1.3 Theoretical Perspective.....	14
1.4 Assumptions.....	15
Chapter 2: Literature Review.....	16
2.1 Blast Behavior.....	17
2.2 Numerical Analysis.....	24
2.3 Mitigation Compartment Design.....	27
2.4 Mitigation Compartment Materials.....	32
2.5 Additional Design Considerations.....	42
Chapter 3: Injury Criteria.....	44
3.1 Background.....	44
3.2 Selected Injury Thresholds.....	44
Chapter 4: Dummy Model for Blast Numerical Analysis.....	47
4.1 Background.....	47
4.2 Dummy Modification.....	47
Chapter 5: Mitigation Compartment Shape Study.....	54
5.1 Numerical Model.....	54
5.2 Results.....	56
5.3 Conclusion.....	63
Chapter 6: Confined Blast Cylinder and Plate Study.....	65
6.1 Numerical Model.....	66
6.2 Numerical Results.....	69
6.3 Conclusion.....	76
Chapter 7: Free Field Blast Cylindrical Mitigation Study.....	78
7.1 Numerical Model.....	78
7.2 Numerical Results.....	81
7.3 Experimental Approach.....	85
7.4 Comparison of Numerical Analysis and Experimental Data.....	88
7.5 Conclusion.....	91
Chapter 8: Confined Blast of Cylindrical Compartment.....	93
8.1 Experimental Field Test Set-up.....	93
8.2 Experimental Field Test Results.....	96
8.3 Numerical Analysis Model.....	107

8.4 Comparison of Results	110
8.5 Conclusion	113
Chapter 9: Introduction of “Blast-Test” Dummy.....	115
9.1 Numerical Model	116
9.2 Dummy Analysis Results.....	121
9.3 Comparison of Dummy and Confined Plate Numerical Results	128
9.4 Conclusion	132
Chapter 10: Conclusion.....	134
10.1 Mitigation Compartment Design and Confined Blast Effects	134
10.2 Numerical Analysis Model and Experimental Correlation.....	138
10.3 Further Research	139
Bibliography	141

List of Tables

Table 2.1. Advantages and disadvantages of fiber reinforced composites to conventional metal materials [Bond, 2005].....	34
Table 2.2. Common types of polymeric matrices [Bond, 2005].....	35
Table 2.3. Summary of common fiber materials. [Bond, 2005].....	40
Table 3.1. Recommended injury criteria for landmine testing. [Tabiei, 2007]	45
Table 3.2. Blast Injuries a) overpressure and b) cutoff ΔP values [Morka, 2005]	46
Table 5.1. Shape study compartment statistics.....	55
Table 5.2. FEM summary of shape study	56
Table 6.1. Cylinders (a) listed by size (b) listed by mass.....	66
Table 6.2. FEM snapshot of the confined plate study.....	68
Table 7.1. Free field cylinder dimensions.....	78
Table 7.2. FEM summary of free field model.....	80
Table 7.3. Comparison of cylinder mid-line deformation.....	91
Table 8.1. Cylinder properties for confined field test.....	93
Table 8.2. FEM snapshot of the confined plate study, $1/8^{\text{th}}$ symmetry.....	108
Table 9.1. FEM summary of the dummy models	121
Table 9.2. Key for dummy result figure legends	124

List of Figures

Figure 2.2. a) T55 Enigma armored Iraqi tank and b) close-up of spaced armor cross-section [Piggott, 2004].....	30
Figure 2.3. Example of composite armor [Defense, 2004].....	34
Figure 2.4. Comparison of composites and metals [Bond, 2005].....	35
Figure 2.5. Metal matrix composites [Bond, 2005].....	37
Figure 2.6. Example of hybrid SMAs [Quidwai, 2004]	42
Figure 4.1. Overview of dummy model.....	48
Figure 4.2. Location of acceleration nodes within dummy model, parts hidden.....	49
Figure 4.3. Location of acceleration nodes within dummy model.	50
Figure 5.1. Shape study mitigation compartments.....	54
Figure 5.2. Compartment material energy, normalized by mass.	57
Figure 5.3. Cubic compartment maximum element pressure snapshot.	59
Figure 5.4. Cylindrical compartment maximum element pressure snapshot.....	59
Figure 5.5. Spherical compartment maximum element pressure snapshot.....	60
Figure 5.6. Cubic compartment plastic strain at 5 msec.	61
Figure 5.7. Cylindrical compartment plastic strain at 5 msec.....	62
Figure 5.8. Spherical compartment plastic strain at 5 msec.	62
Figure 6.1. Graphical representation of cylinders arranged in order of mass.....	66
Figure 6.3. One-eighth symmetric model, air mesh hidden.....	69
Figure 6.4. Explosive event at $t=0.0007$ sec, air mesh hidden.....	70
Figure 6.5. Plate acceleration, 12 in diameter cylinders.	70
Figure 6.6. Plate acceleration, 15 in diameter cylinders.	72
Figure 6.8. Plate center element overpressure, 15 in diameter cylinders.	74
Figure 6.9. 12 in diameter cylinder material kinetic energy, normalized by mass.	75
Figure 6.10. 15 in diameter cylinder material kinetic energy, normalized by mass. ..	76
Figure 7.1. Free field model perspective view, gages located 30 in from charge center.	80
Figure 7.2. Free field model mesh view.	80
Figure 7.3. FE model animation of dominate fluid for 10.75 in diameter cylinder....	81
Figure 7.4. FE model animation of dominate fluid for 12.75 in diameter cylinder....	81
Figure 7.5. FE model center-line deformation plot for cylinders.	83
Figure 7.6. Pressure history for 10.75 in diameter cylinder.....	84
Figure 7.7. Kinetic energy plot for cylinders.....	85
Figure 7.10. Post experiment center-line deformation of 12.75 in cylinder.....	87
Figure 7.11. Post experiment center-line deformation of 10.75 in cylinder.....	88
Figure 7.12. Pressure history for 10.75 in diameter free field experiment.	88
Figure 7.13. Pressure history comparison, Gage 1.	89
Figure 7.14. Pressure history comparison, Gage 3.	90
Figure 7.15. Pressure history comparison, Gage 2.	91
Figure 8.1. Chamber interior, 30 in tall cylinder; rotating plate removed.....	94
Figure 8.2. Chamber interior, 15 in tall cylinder	95
Figure 8.3. Gages (a) Wall flush mounted (b) Pencil gage exterior view	95

Figure 8.4. Access holes (a) Wall flush mounted, exterior view (b) HE access hole.	95
Figure 8.5. Confined blast post-test #1 view of chamber and chamber door.	96
Figure 8.6. Confined blast post-test #1 view of interior	97
Figure 8.7. Confined blast post-test #1 exterior view of gage stands.	97
Figure 8.8. Confined blast post-test #1, wall flush mounted gage stand.	98
Figure 8.9. Confined blast post-test #1, view A of 15 in high cylinder deformation	98
Figure 8.10. Confined blast post-test #1, view B of 15 in high cylinder deformation.	99
.....	99
Figure 8.11. Pressure history of test #1	100
Figure 8.12. Pressure history of test #1, side-on pencil gage	101
Figure 8.13. Pressure history of test #1, plate flush mounted gage	101
Figure 8.14. Pressure history of test #1, chamber wall flush mounted gage	102
Figure 8.15. Confined blast post-test #2, exterior view and door hinge failure	102
Figure 8.16. Confined blast post-test #2 post-test, chamber door deformation.	103
Figure 8.17. Confined blast post-test #2, pressure gage displacement.	103
Figure 8.18. Confined blast post-test #2, view A of 30 in high cylinder deformation.	103
.....	103
Figure 8.19. Confined blast post-test #2, view B of 30 in high cylinder deformation.	104
.....	104
Figure 8.20. Pressure history of test #2	105
Figure 8.21. Pressure history of test #2, side-on pencil gage.	106
Figure 8.22. Pressure history of test #2, plate flush mounted gage.	106
Figure 8.23. Pressure history of test #2, chamber wall flush mounted gage.	106
Figure 8.24. Confined blast full model, reflected about symmetric planes.	109
Figure 8.25. Confined blast 1/8 th symmetry.	109
Figure 8.26. FEA confined blast pressure history	110
Figure 8.27. Pressure history comparison, chamber wall center.	111
Figure 8.28. Pressure history comparison, side-on gage	111
Figure 8.29. Pressure history comparison, plate center	112
Figure 9.1. ALE mesh section cut of cubic charge	117
Figure 9.2. Model 1: Dummy free field blast, unmitigated.	118
Figure 9.3. Model 2: Dummy free field blast, mitigated	118
Figure 9.4. Model 3: Dummy confined blast, unmitigated	119
Figure 9.5. Model 4: Dummy confined blast, mitigated	119
Figure 9.6. Snapshot of mitigated confined dummy and free field dummy events..	122
Figure 9.6 Head acceleration, free field blast.	124
Graph 9.7. Head acceleration, confined blast	125
Figure 9.8 Chest acceleration, free field blast, no mitigation	126
Figure 9.9 Chest acceleration, free field blast, with mitigation	126
Figure 9.10 Chest acceleration, confined blast, no mitigation	127
Figure 9.11 Chest acceleration, confined blast, with mitigation	127
Figure 9.12. Confined blast, mitigation cylinder and plate FEM	129
Figure 9.13. Confined blast, mitigation cylinder and dummy FEM	129
Figure 9.14. Comparison of dummy chest and plate center-node accelerations.	130
Figure 9.15. Cylinder mitigation compartment deformation at 10 msec.	131
Figure 9.16. Cylinder mitigation compartment deformation.	132

List of Abbreviations

ALE	Arbitrary Lagrangian Eulerian
ARL	Army Research Laboratory
CFD	Computational Fluid Dynamic
CONWEP	Conventional Weapons Effect Program
CSM	Computational Solid Mechanics
DDT	Deflagration to Detonation Transition
DRI	Dynamic Response Index
EOS	Equation of State
FE	Finite Element
FMVSS	Federal Motor Vehicle Safety Standards
HE	High Energy (Explosive)
HIC	Head Injury Criterion
HIP	Head Impact Power
IE	Internal Energy
KE	Kinetic Energy
LSTC	Livermore Software Technology Corporation
NIC	Neck Injury Criterion
PFAC	Penalty Factor
RHA	Rolled Homogeneous Armor
SPH	Smooth Particle Hydrodynamics
TTI	Thoracic Trauma Index
VPG	Virtual Proving Ground

Chapter 1: Introduction

1.1 Problem Statement

Mitigation can be defined as a protective approach to reducing the magnitude or likelihood of an event or exposure of persons or property. Blast mitigation should reduce the overpressure, impulse, fragments, projectile, thermal and toxic hazards that occur during an explosive event. Research dedicated to portable sized mitigation compartments is growing, with performance criteria concentrating on the compartment's response to the blast event; few reports contain the effects of the mitigating effects on surround structures or persons. In addition, an explosive event dually confined by both a mitigation compartment and a subsequent enclosure, produces overpressures and impulses vastly different from a singularly confined explosive event. As this research will demonstrate, a "well-performing" mitigation compartment may increase the lethality of the explosive event. In order to develop improved compartment protective technologies, the dynamic interaction of confined blast loading within structures needs to be understood in addition to the implications of compartment shock mitigating mechanisms.

1.2 Purpose of Study

This research was conducted in conjunction with the Army Research Laboratory, Aberdeen Proving Ground. Historically research dedicated to armoring military vehicles has concentrated on hull reinforcement to withstand the impact of shrapnel, bullets, missiles, or shells. However, the crews of even the most advanced armored hull face the risk of disturbance to the ammunition carried inside their

vehicle. Few developments have been made to provide crew shielding from an internal event, e.g. misloaded or unstable stored munitions. Under the demanding rigors of the battlefield, the new age of lightweight military vehicles has emerged with many of the heavy internal protective elements moderated or removed.

The primary objective of this research is to use a robust computational approach to evaluate the occupant protective effectiveness of a light-weight mitigation compartment during confined blast. Confined blast behaves drastically different depending on the mass and volumes of objects within the confined space. This study's application is specifically targeted for protecting personnel within an armored vehicle. However, this research is significant to any blast mitigation application that occurs within an enclosed space. Laboratories, mailrooms, storage lockers, building entry-control points, shipping stores, airline cargo holds, etc. are a few examples.

The secondary objective of this research is to introduce the use of a numerical blast-test dummy. Calibrated blast-test dummies do not exist. The automotive industry and the US Air Force have successfully calibrated dummies to appropriately examine specific human injuries from high speed, high impact crash and ejection events. Blast loading occurs much faster and usually in much greater magnitude than crash and ejection events. The introduction of a rudimentary numerical blast-test dummy provides an interesting comparison (compared to pressure plates or void space) of possible acceleration injuries, even though a correlated test dummy is not available at this time.

1.3 Theoretical Perspective

“Energy can neither be created, nor destroyed. It can only be transformed from one form to another.”

Efficient energy absorbing material and structural design are fundamental to blast protective systems. When detonation or deflagration occurs within a confined space, blast effects are further compounded. The multiple reflections of the blast wave cause longer durations and complex pressure loading on the enclosure walls. Additionally, when a charge is placed within a short distance from a blast shield, the shock can perforate the shield, a phenomenon called shock holing. The nonlinear dynamic analysis of shells with combined membrane and bending behavior is particularly complex and challenging. Analytical solutions are inaccurate except in all but the most simplified of blast resistant structures. Therefore, numerical models need to be developed. Numerical computer analysis provides critical information about dynamic deformations and damage during the load blast wave, allowing for detailed, rigorous analyses of time histories of accelerations, velocities, deformations, and stresses. This study uses eta/VPG 3.3 PrePost processor and LS DYNA explicit dynamic nonlinear FE software. Explosive gas flow is visible in LS DYNA analysis when arbitrary Lagrangian Eulerian (ALE) methodology is applied. However, integration of fire effects with the blast analysis is not available at this time.

Thermal and toxic hazards from burning energetic materials cannot be ignored when evaluating crew survivability, however, fire performance is not the focus of this research. Due to time and numerical modeling limitations, mitigating heat and toxic vapor hazards for crew survivability will not be addressed. Since the proposed internal event is of short duration fire resistant coatings, as well as active fire

suppression systems are ineffective with the burning of energetic material. Venting for controlling thermal and toxic vapor effects would be appropriate areas to examine further.

1.4 Assumptions

Assumptions/Confines are listed below:

- Internal event is an isolated event – single high explosive detonation
- Munition deflagration to detonation transition (DDT) is instantaneous; high explosive behavior
- Compartment is considered to be fixed to the frame of the vehicle; no acceleration differentials between compartment, explosive charge, occupants, and vehicle chamber
- FE modeling of vehicle chamber is restricted for unclassified presentations and publications simulations and will have the generic geometry of a simplified box structure
- Vehicle speed, direction and vibration are not taken into account
- Thermal effects of fire are not included nor coupled with LS DYNA blast modeling
- Duration of the blast and burning events are relatively short
- Any weld and bolt failure criteria are modeled as constraints only
- Small holes and negligible internal obstructions (pressure gage stands, plate supports and compartment cables) in the laboratory environment do not effect the initial response

Chapter 2: Literature Review

Current world events continue to necessitate advancement of protective technologies. Researchers have made enormous strides in understanding and modeling blast loads and energy absorbing systems. Advanced computer technology has accelerated the ability to handle complex dynamic problems with greater accuracy, providing greater insight into the performance of energy absorbing materials and advanced structural designs.

However, despite the plethora of literature on blast mitigation technology, little publicly available research exists on the complex dynamics of confined blast. Of the few accessible experimental studies, one thing is certain; the complexity of internal blast loads is further problematic by the capricious nature of the containment chamber's construction and/or material defects. Any mass within the confined space increases the unpredictability of the response during the internal blast event.

When the confined space is the cramped interior of a vehicle, there are additional difficulties with protecting occupants and equipment should a blast event occur. The incorporation of the most cutting edge armor within a vehicle is a double edge sword. While mitigation materials provide critical protection, the mitigation mechanism itself adds weight, thereby decreasing vehicle mobility and efficiency. Heavier vehicles also require larger engines, which consume larger quantities of fuel, taking a greater toll on the mobility and subsequent survivability of the vehicle. Advances in energy absorbing systems for vehicle armament must concentrate on light-weight designs.

Mitigation compartment geometry and material choices are crucial design choices when considering the survivability of occupants within the enclosed space. The author's selection of geometry and material was not based on performance only. The predominate need was to maintain focus on occupant survivability during confined blast without added complexity detracting from the analysis in conjunction with time, cost and availability considerations. The focus of this research was not to construct a prototype mitigation compartment, yet certain criteria, e.g. weight, allow for appropriate decision making design parameters. This research is limited to simple geometries and common armor metals; the following paragraphs are included for completeness. This section reviews previous scholar and researcher contributions applicable to this research in the areas of confined blast, numerical modeling, and confined blast mitigating structures.

2.1 Blast Behavior

Detonation is characterized by a violent release of energy in a gaseous medium giving rise to sudden pressure increase. This instantaneous rise from the normal pressure is called "peak-incident overpressure" and it forms the blast wave or shock front that travels at sonic speeds. The type of explosive, energy output, weight, location (often described in standoff distance and angle of incidence, angle between the moving direction of a blast wave and the target surface) and blast environment determine the magnitude and distribution of the blast load. The effects of a blast onto a nearby structures or containment vessels are described by numerous authors such as Gregory, Kingery, Ewing and Schumacher, Baker et al, Norris et al, Bulson and Tedosco et al.

The overpressures associated with the blast load impinge the structure as side-on or incident overpressure, windward-side or reflected overpressure, or leeward-side or diffracted overpressures. Figure 2.1 shows an example of a pressure profile parameterized by peak overpressure P_{s0} , time of duration t_0 , and arrival time of the blast wave front t_a . The overpressure profile is defined as the positive phase of pressure profile and, in general, considered the most important part of the pressure profile.

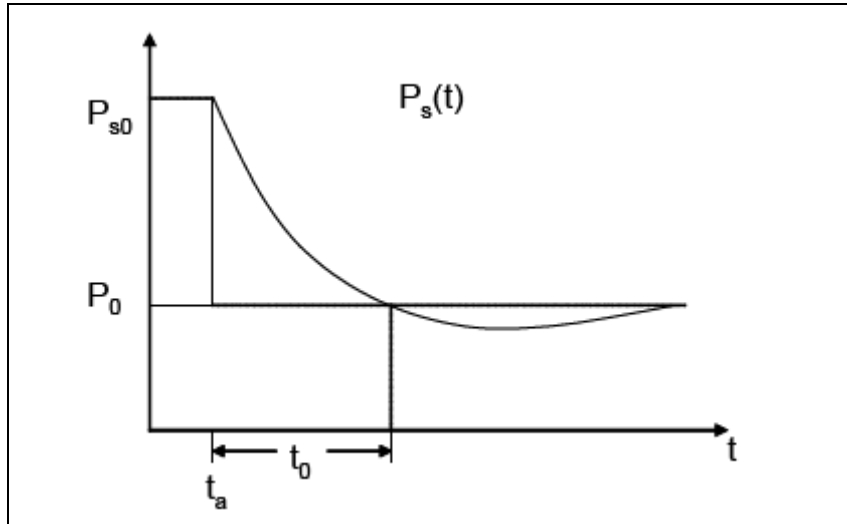


Figure 2.1 Overpressure profile.

Free air blast is defined as an explosion that occurs sufficiently above the ground that the shock front impacts the structure before interacting with the ground surface. Good to excellent results can be obtained from empirical equations for unobstructed free air blast. Bulson [1997] references the US Army Technical Manual TM5-855-1 with providing the following equation for the peak pressure, p_0 (psi) for a specific weight charge, W , at a specific standoff distance, R , from the charge:

$$p_0 = \frac{4120}{z^3} - \frac{105}{z^2} + \frac{39.5}{z} \quad (2.1)$$

Where,

$$z = \frac{R}{W^{1/3}} \text{ (R in feet, W in equivalent TNT lbs)}$$

Equation 2.1 is only valid when $160 > p_0 > 2$ psi and $20 > z = \frac{R}{W^{1/3}} > 3$ ft/lb^{1/3}.

For unconfined plate like structures subjected to free air blast, equation 2.2 has a good degree of accuracy in predicting the overpressure profile on the structure [Kotzialis, 2005].

$$P_s(t) = P_s \cdot \left(1 - \frac{t-t_a}{t_d}\right) \cdot \exp\left(-a \frac{t-t_a}{t_d}\right) \quad (2.2)$$

Where,

P_s = intensity of blast wave

t = time

t_d = time interval when overpressure is positive

a = dimensionless calibration constant for pressure profile.

The pressure profile is characterized by the orientation of the structure to the shock front. When the shock front reaches the structure, the blast waves may be oriented normally or obliquely to the surface. Oblique reflections involve incident, reflected and/or Mach stem shock waves. Incident pressures are defined as the direct shock wave pressures measured at a point in time in the air space. These are also referred to as “side-on” pressures. Reflected pressures are defined as the blast loadings felt by the structure, or the pressure imposed on the structure’s surface by the reflecting shock wave. Reflected pressures are always higher than the incident pressures for the same standoff distance. The angle of incidence, measure of

deviation from "straight on", dictates the magnitude by which the reflected pressures increase from the incident pressures. The reflected pressures can be as much as 4 times the incident pressure depending on incident overpressure, the angle of incidence and proximity [Bulson, 1997]. This behavior of overpressure magnification between the incident and oblique reflecting shock waves is discussed in detail in a report by Glasstone and Dolan (1962), *The Effects of Nuclear Weapons*, U.S. Department of Defense and U.S. Department of Energy.

When a solid body is impacted, the deformation efficiency of the structure to absorb this force is defined by the following:

$$n = \frac{U_e}{m \cdot d} \quad (2.3)$$

Where,

U_e = absorbed energy

m = mass

d = collapsed distance

Kotzialis modified this equation for use with sacrificial cladding calculations to the following:

$$n = \frac{U_e \cdot c_w}{I_w \cdot d}; \text{ where } I_w = \int_{t_1}^{t_2} \int_{A_t} p dA_t dt \quad (2.4)$$

Where,

I_w = impulse of blast wave

p = pressure profile of wave

A_t = area of the surface where pressure p acts

c_w = initial velocity

The stiffness and shape of the mitigation must be chosen to optimize n , yet this is dependent on the development of plastic zones and the formation of plastic hinges. Prediction of the plastic deformations can be accomplished through deliberate placement of specific armor curves. The optimal design of Kotzialis's sacrificial cladding for unconfined blast loading was achieved when the force between the main structure and the armor was close to zero, thus the collapse space efficiency satisfied the following equation:

$$n \approx \frac{m_c \cdot c_w}{I_w} \cdot n_c \quad (2.5)$$

Where,

n_c = mean acceleration developed inside the mitigation armor

n = deceleration that the sacrificial cladding provides

m_c = armor mass

Analytically it is difficult to solve all but the most simplified of blast resistant structures.

The other categories of blast quickly deviate from the free air blast in both structural response complexity and ability to predict the overpressure profiles. Air blast occurs when the detonation occurs above the ground, but the initial shock wave is amplified by the interaction of reflected pressure waves from the ground before arrival at the structure. Surface blast is when the charge is on or very close to the ground where the incident and reflected shock waves merge at the point of detonation. Confined blast is the occurrence of the explosion within a structure.

When an explosion occurs within a confined space, both shock loading and quasi-static gas loading contribute to the pressure loads. Peak pressures are very high and shock fronts, which occur a few milliseconds before the gas loading stage, can reflect and magnify causing the “mach fronts” to occur [Zukas, 1998]. If detonation occurs in a confined space, reinforced by infinitely strong inflexible and airtight boundaries, the shock wave will reflect from all faces and a rise in the ambient gas pressure will occur. The shock wave will continue to reflect until the energy of the explosion is expended in heat and perhaps some form of absorption by the confining walls [Bulson, 1997]. The peak amplitude of the shock front is generally significantly larger than the peak gas pressure; however, the duration of the gas pressure phase will be much longer than the shock loading phase and unlike the shock front, will apply a uniform pressure throughout the entire containment vessel [Esparza, 1996]. Baker et al [1989] show higher pressures occurring in the corners of the chambers attributed to incident and reflective shock waves combining to generate Mach waves. While the shock front is the primary mechanism for energy transfer to the containment vessel, White et al [1977] found that somewhat less than 1% of the energy of the explosion is transferred to the containment vessel walls by the air shock wave. The high-temperature and high-pressure gases account for the majority of the explosive energy. Without venting, the accumulation of gaseous pressure and blast overpressure subject the confined structure to not only higher pressures, but longer duration loads. The impulse the containment vessel experiences is calculated as the area under the overpressure-time duration curve. The overpressure history for even simple geometry compartments is complex and highly dependent on many factors, to

include compartment venting, deformation, size of explosive, internal volume, inclusion of objects within the confined space, relative position of explosive charge to structural elements, and duration of the event.

Baker [1960] details the equation of motion and linear-elastic response of thin walled spherical containment vessels subjected to a centrally located, spherical shock wave. Thin (1/16th inch thick) steel shells, radii of 15 and 30 inches, were subjected 1/8 lb Pentolite explosive charges during laboratory tests conducted at the Army Research Laboratory (ARL). The smaller shells ruptured along the weld lines but data collected showed fairly good correlations to the linear theory and non-linear, no strain hardening, predictive calculations. White et al [1977] provide a nice brief overview of the collection of the solutions derived for spherical blast containment. They conclude that the main advantage of allowing elastic-plastic behavior in a spherical metal containment vessel is the substantial allowable reduction in vessel weight.

Previous research on spherical, cylindrical, cubic and other variations of these geometries points to the singularly unique response of each compartment design based on the material, precise construction and design, and explosive charge size and placement. Structurally, panels resist blast primarily through both membrane and bending behavior. This nonlinear dynamic analysis of shell structures is particularly complex and challenging. Analytical approaches provide only a limited understanding of the nature of this behavior. Thus they do not apply to nonlinear problems in general, and numerical approaches have to be used [Koh et al, 2003].

2.2 Numerical Analysis

Numerical computer analysis provides critical information about dynamic deformations and damage during the blast event, allowing for detailed, rigorous analyses of time histories of accelerations, velocities, deformations, and stresses. Resulting acceleration and overpressure histories can be correlated with expected blast injuries of the vehicle crew. In explicit formulation the solutions, typically displacements, are expressed as a function of other variables and parameters. In implicit formulation solutions are contained within a function and the values must be extracted, normally through numerical algorithms. Explicit formulation is particularly suitable for problems with short duration such as impact or explosion. Experimental investigation must also be used to assess the appropriateness and predictive capabilities of any numerical modeling.

CONWEP (Conventional Weapons Effect Program) is a program distributed by the United States government that allows for the calculation of overpressure one location at a time, to include allowing for simple interactions with plates and shells. CONWEP models free air blast or surface detonation of spherical and hemi-spherical charges. Despite the popularity of CONWEP, this blast modeling method does not have the ability to do complex structural interactions nor predict confined blast scenarios.

The advancement of computer technology has surged the ability to perform rigorous numerical models for blast and material behavior prediction. As early as the 1940's non-linear time dependant wave propagation models were being used to analyze explosive events. The 1960's replaced these earlier CFD (Computational

Fluid Dynamic) and CSM (Computational Solid Mechanics) models with hydrocodes, which based the explosive behavior on the hydrodynamic material behavior and ignored material strengths [Zukas, 2004]. Today's hydrocodes are much more complex and complete than those first developed. Hydrocode methodologies can be characterized as Lagrangian, Eulerian, Coupled Eulerian-Lagrangian, and Arbitrary Lagrangian-Eulerian [Mair, 1999].

In Finite Element (FE) modeling and analysis the deformation of a continuous medium is described as either Eulerian or Lagrangian. Pure Lagrangian formulation, as typically used in structural FE analysis, is efficient and accurate for small to moderate deformations where the computational mesh deforms with the material, automatically following the material deformation [Ozel, 2006]. Lagrangian cell boundaries occur at free surfaces and material boundaries and the mesh distorts to match the distortion of the material. While the free surfaces and material interfaces are well defined, Lagrange solvers perform very poorly for large deformations, often resulting in severely distorted meshes, negative volumes, small timesteps with overall inaccuracy. Lagrangian solvers biggest advantage is the ability to track the element's deformation over time. A spin-off of the Lagrange solver is Smooth Particle Hydrodynamics (SPH). This technique groups the materials together in the form of particles. The particles can be related to Lagrangian nodes; subsequently as the part moves, the nodes move.

In Eulerian analysis the computational mesh is fixed in space. Eulerian meshes occur over a space, allowing the materials to flow through the cells. While grid distortions are eliminated, Eulerian solvers require high mesh densities or

simplified geometry, affecting either the run time or the accuracy of the results.

Tracking the deformation of a particular part is difficult with this method and not appropriate for modeling solids.

The Arbitrary Lagrangian Eulerian (ALE) technique combines the features of pure Lagrangian analysis and Eulerian analysis. This solver allows for different parts of the model to behave either as Lagrangian (solids) or Eulerian (fluids). ALE formulation allows the modeling of fluid structure interactions with a fluid structure coupling algorithm. ALE in LS DYNA involves modeling the charge and surrounding fluid, namely air in this study, with an Eulerian mesh, which is coupled with the Lagrangian mesh of the structures. Equations of state (EOS) are used for the high energy (HE) charge and air. The ALE method models the explosion and calculates the pressure profile through the fluid. The coupling between the Lagrangian elements (structure) and ALE elements (charge and air) is accomplished using the LS DYNA's `CONSTRAINED_LAGRANGE_IN_SOLID`.

Both cubic and spherical surfaces are chosen for the Detonation Wave (DW) front for this study. The explosive's contained energy is immediately released into the DW, assuming no net loss in mass:

$$HE \rightarrow PD + Q \quad (2.6)$$

Where:

HE = High Explosive
PD = Products of detonation
Q = Heat effect of reaction

The PD is characterized by the EOS Jones Wilkin Lee (JWL) equation:

$$p = A \left(1 - \frac{\omega}{R_1 \bar{\rho}} \right) \exp(-R_1 \bar{\rho}) + B \left(1 - \frac{\omega}{R_2 \bar{\rho}} \right) \exp(-R_2 \bar{\rho}) + \frac{\omega \bar{e}}{\bar{\rho}} \quad (2.7)$$

Where:

P = pressure of PD

$\bar{\rho} = \rho_{HE} / \rho$

$\bar{e} = \rho_{HE} e$; energy per unit volume

ρ_{HE} = density of HE

ρ = density of PD

e = specific enternal energy of HE

A, B, R_1, R_2, ω = HE specific emperical constants

Yen et al [2005] discuss the contributions of ALE for accuracy and stability.

ALE is consistently used in complex dynamic analysis by today's leading researchers with excellent correlation to experimental results. Gupta et al [2006] provides a detailed and thorough description of ALE and LS DYNA interactions with experimental correlation.

The penalty factor (PFAC) in the CONSTRAINED_LAGRANGE_IN_SOLID card allows the penetration of the HE explosive/air volume fraction into the Lagrangian mesh to be controlled. When the charge is spherical the ALE mesh's element shape transitions from spherical to square; this mesh allows for a faster moving and concentrated pressure wave.

2.3 Mitigation Compartment Design

Confined blast loading research can be traced back to E. B. Philip's report in 1944 on air blast through tunnels and D. G. Christopherson's 1945 work on empirical blast pressure relationships for vented and rigid enclosures. Yet, it was not until the 1970's with the advent of computer processing that internal blast loading received thorough analysis. The forefather's of this confined blast loading research include Baker [1960], Baker et al [1983], Gregory [1976], and Kingery, Ewing and

Schumacher [1975]. Their work is reviewed in brevity in Bulson's [1997] textbook. Yet even with the greater understanding of confined blast loading the detailed design of a containment vessel has received guarded attention. Few publicly released reports are available, most likely attributed to national security and proprietary safeguards.

White et al [1977] discuss the merits of a simple lightweight door constructed of one-piece round port overlapping a full 360 degrees on a reinforcing ring from the inside of the vessel. All vessels tested were spherical in shape with ductile steel of inside diameter's ranging from 61-152 cm and wall thickness ranging from 1.27 - 3.56 cm. Vessels were unvented and catastrophic failure occurred in only one tested vessel, concluded to occur from the effects of the confined gas pressure. The diameter to wall thickness ratio combination for the lowest weight vessel and maximum allowable contained-charge weight was cited as an area for continued research. Continued research did indeed occur, with vessels of cylindrical, cubic and spherical shapes, vented and unvented, with large openings, with frangible elements, in empty and obstructed enclosures. Park et al [2007] provide a comprehensive comparison of the predictive capabilities of explosion venting in chambers with internal obstacles and offer a new experimentally validated empirical equation. This equation described the overpressures occurring in a chamber based on the obstacle geometry, boundary conditions, length to diameter ratio of the vessel and a turbulence factor.

Esparza et al [1996] proof tested an 11.5 ft diameter cylindrical 1.5 inch thick steel vessel fabricated to contain explosion of up to 10 kg of TNT. The Jaycor [1999] report steps away from large steel containment vessels with a rounded edged 2 ft by 2

ft by 2 ft cubic vessel constructed of lightweight man-made fibers found in ballistic armor. This vessel had removal panels that could be added based on the desired containment

The geometry of armor has significant impact on the efficiency of blast mitigation and energy absorption. The principles of sacrificial cladding can be applied to confined blast mitigation structures through “weak” or “soft” zones. The elements of the confined structure can be designed to fail so as to minimize the amplification of gaseous pressures and blast overpressures. Burman et al [1993] conducted numerous experimental tests to examine deformation and failure models of internally explosively loaded cubic, welded steel compartments. Their work showed compartment failure depended on not only the size and location of the explosive charge, but heavily the compartment’s joint and seam manufacturing quality. Their work also highlighted the detrimental effects of “haphazardly modifying, ie strengthening or weakening, individual parts of structures which may be subjected to internal blast loading.” Properly designed sacrificial layers dissipate energy through large plastic deformation subsequently limiting the forces transmitted to the main structure. These energy absorbing layers are typically collapsible structures constructed from a ductile material. This concept of armor with sacrificial layers is referred to as spaced armor.

Spaced armor is the simplest protective arrangement after homogeneous armor. Spaced armor is defined by the structural design or geometric configuration of the armor. This armor uses buffering zones between material layers; with the exterior layers acting as sacrificial barriers to the protected structure, see Figure 2.2. Spaces

between layers may contain nothing but air, cross-bracing, or other energy absorbing filler materials.



Figure 2.2. a) T55 Enigma armored Iraqi tank and b) close-up of spaced armor cross-section [Piggott, 2004]

Spaced armor can cause bullets and solid shot to tumble, deflect, and disintegrate, reducing their penetrating ability—for which effect spaced armor was used as early as WWI, on the Schneider CA1 and St Chamond tanks. Hollow spaces between panels of armor increase the length of travel from the exterior of the vehicle to the interior, reducing the penetrating power; sometimes the interior surfaces of these hollow cavities are sloped, presenting angles to further dissuade penetration. Replacing a single 12 in layer of steel armor with two 6 in layers spaced apart provide greater protection against shaped charges with no penalty in additional weight. Theobald and Nurick [2007] examined square tubular elements which absorb energy through the progressive folding of a shell wall. The layered structure used mild steel ‘web plates’ sandwiched between layers of similar material. Energy was absorbed through large plastic deformations in the web plates, with each layer successively collapsing. Buckling stability of tubular elements is highly sensitive to loading angle

and if the face plate is not rigid, the transferred load must be assumed to be applied at an oblique angle. Oblique loading, strain rates and inertia effects become significant when analyzing the response of an absorber. Theobald and Nurick found there was a clear correlation between absorber performance and crushing mode. The absorption process was defined by two distinct phases of panel motion. First, the axial compression and bending created the first lobe and plastic hinges formed at the supports (tubes) in the top plate. Second, energy absorption was almost entirely through progressive and global buckling of the tubes. The top plate moved rigidly and energy absorption in the top plate became insignificant. An increased number of tubes increased the number of hinges formed in the top plate, as well as significantly increasing the energy absorbed per unit time in the core. Theobald and Nurick concluded that to determine the ideal number of tubes, the maximum applied impulse to the panel must be known in addition to the loading requirements of the protected structure. If these values are known spaced armor geometry can distribute the loading evenly, producing similar stroke usage and crushing behavior in each tube, and the highest core energy absorption will be achieved. Thus, if the size of the HE explosive is known, this type of design can be decidedly successful.

Variations in containment wall's cross-sectional shape not only have the potential to enhance energy absorption but also can greatly reduce the overall weight of the system. Corrugation of single panels has been studied and found to reduce panel weight without reducing performance. This wavy design was tested in Boeing 737 compartments retrofitted for blast protection. Reduction of blast shield weight without sacrificing strength was achieved, however, wave amplitude infringed upon

the internal compartment space [Dang and Chan, 2006]. Porous barriers or venting can potentially reduce peak dynamic overpressures; allowing little resistance to gas flow and can prevent the passage of a flame by cooling effects. HE explosion pressures arise primarily from reaction of the last compressed third by volume of the original reactants; this volume contains about 80 percent of the original reactants by weight. Sintered bronze barriers were found to be effective in segmenting the internal volumes internal explosion pressure [Boyd, et al, 1981]. Contradictorily, Cheng and Quan [1998] found that venting provided no significant advantages based on early-time response of the structure which governs the blast resistance of the structure.

2.4 Mitigation Compartment Materials

The author's research was limited by low cost (mild steel) and experimental readily available (RHA) materials. The following paragraphs are presented for completeness and to frame the need for further consideration in material selection for a light-weight, high performance mitigation compartment.

An efficient energy absorbing material will experience significant deformation; the rate and range of deformation are paramount to performance. Historically metals have held prominence in armament. Steel armor was the first armor used on tanks at their invention in the early twentieth century. Conventional steel armor absorbs the kinetic energy of an incoming projectile through ductile deformation. Mild steel, the work horse of industrial construction, is highly strain rate sensitive and temperature dependent. However, mild steel exhibits linear elastic behavior and isotropic strain hardening behavior when subject to plastic deformations [Theobald, 2007]. Mitigating blast in an enclosed space requires a material to remain

ductile and energy absorbent for the reflected and often magnified shock waves. Thus, mild steel is not the best suited material for the complex overpressure loading of a confined blast. However, a materials study conducted by Cheng and Quan [1998] found RHA, a hard steel alloy often referred as “armor steel”, to be the best metal for blast compartments when compared with Aluminum alloy 5083 and Titanium alloy Ti-6Al-4V. Their study compared equal weight and volume box compartments of these three materials when subjected to an internal blast load from a half-pound TNT spherical charge. The materials were ranked based on their reserve strength resulting from the blast loading and the transient pressure 2 feet away from the compartment. Al 1050-0 was used by Kotzialis et al [2005] for sacrificial cladding, allowing for the quick development of plastic deformations due to low yield stress and high failure strains. Aluminum’s highly ductile behavior allows for excellent energy absorption. They used Al 1050-H18 for the other parts of the structure. In general, metal armor has the advantages of developing large plastic deformations, handling multiple hits, and has low environmental sensitivity (temperature, moisture, dust, etc). Yet, metals can also fail catastrophically under large blast loads, often ripping open. In the particular case of vehicle armament, the heavy weight of metals is a clear disadvantage.

Composite armors were developed in the late twentieth century. Composite armor consists of layers of different material such as metals, plastics, ceramics or air. For example, in a ceramic based composite armor the exterior hard-layer deforms the projectile, increasing the cross-section. Figure 2.3 shows how the bullet is fragmented upon impact, thereby greatly reducing its kinetic energy. The smaller

fragments and their residual energy are absorbed by the softer, sub-layers. Most composite armors are lighter than their metal equivalent, but occupy larger volumes for the same resistance to penetration. It is possible to design composite armor stronger, lighter and less voluminous than traditional armor, see Table 2.1 and Figure 2.4, but the cost is often prohibitively high, restricting its use to especially vulnerable parts of a vehicle. Fiber reinforced composite materials are a structural system comprised of a matrix of one type of material, reinforced with a fibrous form of another material. Advanced composites include high-modulus, high strength fibers such as graphite, boron, high tensile glass, ceramic and aramid used in conjunction with polyester/vinyl-ester, epoxy, ceramic and metal matrices [Bond, 2005].

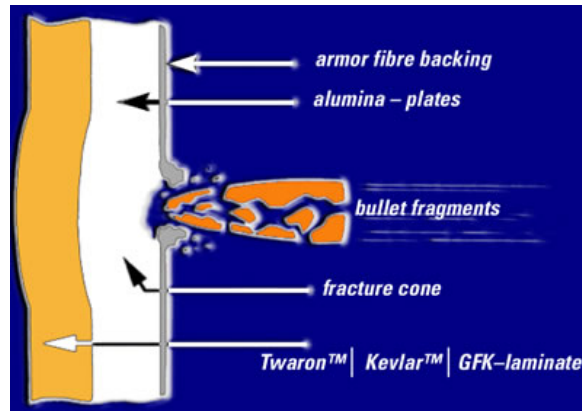


Figure 2.3. Example of composite armor [Defense, 2004]

ADVANTAGES	DISADVANTAGES
Light weight	Expensive raw materials
Resistant to corrosion	Lack of established design allowables
High resistance to fatigue damage	Galvanic corrosion from improper coupling with metals
Reduced machining	Susceptible to environmental degradation
Tapered sections & compound contours easily accomplished	Poor energy absorption and impact damage
Can tailor material for strength /stiffness requirements	May require lightning strike protection
Reduce part number in complex assemblies	Expensive and complicated inspection methods
Absorbs radar microwaves	Reliable detection of substandard bonds difficult
Low thermal expansion	Difficult to locate defects in
	Linear elastic to failure

Table 2.1. Advantages and disadvantages of fiber reinforced composites to conventional metal materials [Bond, 2005]

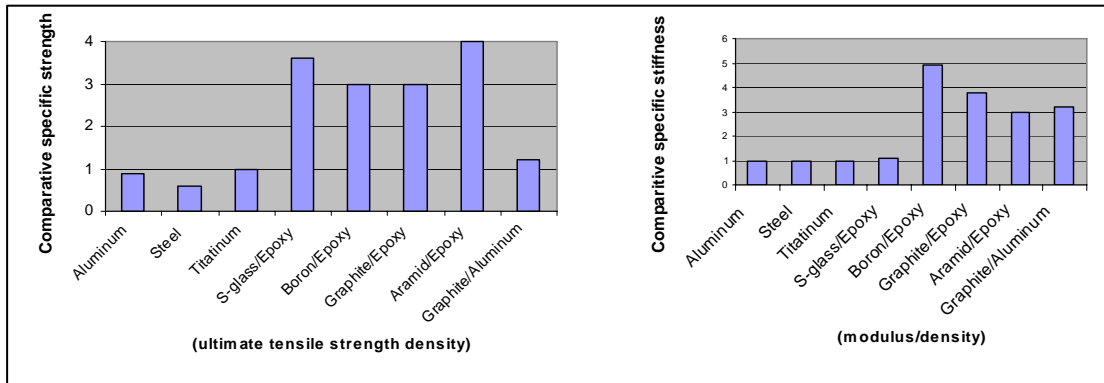


Figure 2.4. Comparison of composites and metals [Bond, 2005]

Typical composite matrix polymers may be categorized as either thermosets or thermoplastics. A thermosetting material becomes permanently hard when heated above a critical temperature and will not soften again on reheating. A thermoplastic material will soften when heated above its glass transition temperature. In general thermoplastic composites are often tougher, with better flexural and impact properties over thermosets. Thermoplastics also have excellent strain capabilities and better resistance to moisture and industrial solvents. They do not appear to have any advantage in static properties or fatigue over thermosets. Thermosets often have higher compression strengths and superior abrasion and dimensional characteristics over thermoplastics. Examples of common thermosets and thermoplastics are shown in Table 2.2 below.

THERMOSET	THERMOPLASTIC
Epoxy	Polyethylene
Polyester	Polystyrene
Phenolics	Polypropylene
Bismaleimides (BMI)	Polyetheretherketone (PEEK)
Polyimides	Polyetherimide (PEI)
	Polyethersulphone (PES)
	Polyphenylene Sulfide
	Polyamide-imide (PAI)

Table 2.2. Common types of polymeric matrices [Bond, 2005]

Other matrix materials include ceramic matrix composites (CMC) and metal matrix composites (MMC). CMCs focus on improving the mechanical properties of the ceramic composite over the unreinforced ceramic matrix and providing higher temperature capability. Ceramics have the advantages of refractoriness, high hardness, wear resistance and chemical durability. Their major disadvantage is their brittleness, thus they do not deform plastically under normal conditions. Additionally, the strength of each specimen is a function of the critical flaw present within the specimen, thus the structural reliability of a component cannot be guaranteed. CMCs are poor candidates for armament due to their low tensile strength, poor impact resistance, and poor thermal shock resistance. [Bond, 2005]

MMCs are a relatively new materials developed for Army applications such as armor, armaments, and vehicle structures [Chin, 1999]. High-strength ceramic-particulate-reinforced MMCs increase penetration resistance against light to medium threats using a hard frontal surface and a softer backing, see Figure 2.5. The hard surface blunts and induces a destructive shock wave on to the impacting projectile, while the softer backing materials act as a “safety net” for residual broken fragments in preventing target penetration. Chin [1999] describes the hard frontal materials as typically ceramics or hardened metallics and Al and fiber-reinforced polymer (FRP) composites are commonly used for backing the harder frontal materials. While a hard frontal material will typically provide the best level of ballistic protection, it is also typically the most brittle and has the potential to exhibit a large collateral damage area from dynamic impact. Fiber-Metal Laminates (FMLs) are lightweight alternatives to structural metals, comprised of layers of metal alloy and reinforced

composite layers. Langdon et al [2007] compared two types of Al-based FMLs: Al layers laminated with (i) glass-fiber reinforced polypropylene (GFPP, a thermoplastic) and with (ii) glass-fiber reinforced phenolic resin (a thermoset). These FMLs were subjected to localized blast loading obtained by detonating PE4 plastic explosive on a 14mm thick polystyrene pad, which attenuated the blast, in the center of the panel. Panel damage demonstrated the blast energy was dissipated through debonding at the Al-GFPP interfaces, matrix cracking and fiber fracture, and Al stretching/tearing. Delamination within the GFPP occurred much less frequently. Thinner panel behavior mimicked that of a monolithic metal plate, as panel thickness increased this behavior changed with debonding failures. Front and rear face damage was controlled by the panel thickness or number of layers. Langdon et al [2007], suggest the spalling of the back face is due to the through-thickness reflected tensile wave propagation and the back face damage shape is influenced by the lateral wave propagation. Repeat/multiple blast loading and fire performance were not examined.

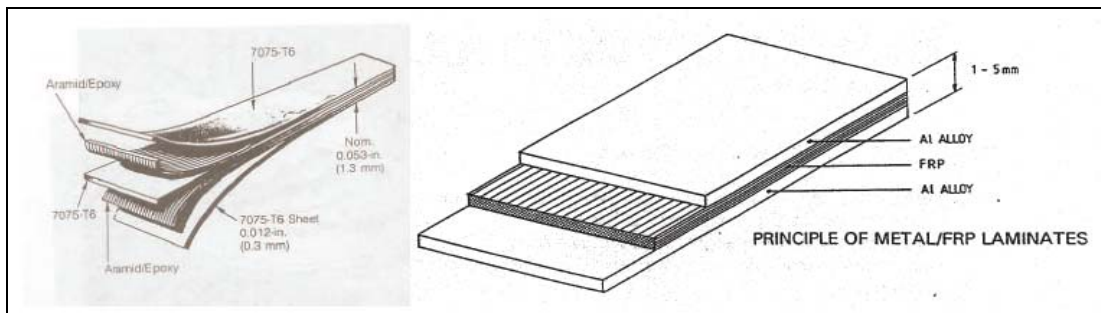


Figure 2.5. Metal matrix composites [Bond, 2005]

Fibers provide the composite with its high stiffness and strength properties. Table 2.3 lists different types of common armament fiber materials and their selection considerations. Performance requirements, processing possibilities and cost

effectiveness vary widely in the selection of fibers. Glass fibers offer excellent strength and durability, and are relatively cheap. E-Glass is the most common glass used for reinforcement, with high strength and good resistance to chemical attack. S-Glass is stiffer and stronger, up to 25 % stiffer and 50 % stronger than 'E', but are more difficult to process and hence much more costly. C-Glass is a chemical resistant formulation. Cheng and Quan [1998] investigated the material performance of traditional military armor metals and a woven composite in blast compartment performance. Cheng and Quan examined RHA, Al alloy 5083, Titanium alloy Ti-6Al-4V, and Woven Roven S-2 glass reinforced polyester composites. Compartment dimensions were modified to keep weights and internal volumes equal. RHA was determined to be the best metal alloy material for compartment design, but overall the S-2 glass fiber reinforced polyester composites provided the best material for mitigating blast loading based on its specific strength and stiffness. Fire performance, repeat/multiple blast loading and fragmentation prevention were not examined.

Boron fibers have a high strength and modulus. They hold the distinction of being the first high performance reinforcement available for use in advanced composites, and were used on the USAF F-15 and the USN F-14 aircraft. However, now carbon fibers are available with better properties and are considerably cheaper. Modern carbon fibers are much stiffer than glass with comparable strengths. Aramid fibers are the principal fibers used in advanced composites since the early 1970s [Bond, 2005]. They are a very low density fiber with their stiffness falling between glass and carbon. Aramid fiber's strength and modulus are considerably higher than S-glass. The fibers are very tough and split rather than fracture, a rationale for their

use in armor. However, aramid fibers perform poorly in compression due to their long kinked molecular backbone, resulting in very low composite compression strengths. The most common type of aramid used in armor is Kevlar. The three types of Kevlar are Kevlar 29, Kevlar 49, and Kevlar 149; their modulus indicated by their designation (i.e. 29, 49 and 149 MPa) [Bond, 2005]. Kevlar 49 fibers in an epoxy matrix are commonly used for engineering composites. When compared to carbon, Kevlar has poor compression strength, but its high tensile strength, high moduli and very high toughness are why Kevlar is used for light-weight armor on vehicles, aircraft, and personal armor. Kevlar was used by Dang and Chan [2006] to laminate a blast shield which demonstrated an increase in resistance to shock perforation and contained fragments. Spectra® is another form of aramid fibers. They have moduli over 120GPa, very low densities, very high specific stiffness and strength, excellent toughness and high solvent resistance [Bond, 2005]. These fibers, however, are difficult to bond to polymeric matrices and melt at 120°C. Interest in ceramic fibers is primarily for their elevated temperature properties and chemical stability, especially in MMCs. While they have high stiffness, they have relatively lower strengths than glass, carbon and aramid.

FIBRE MATERIAL	PROPERTIES
Glass	High strength Low density Small fibre diameter Cheap Low elastic modulus
Boron	High elastic modulus High strength Low density Large fibre diameter Very hard Expensive Low thermal expansion Good compressive properties
Carbon	Moderate to high strength Moderate to high modulus Low density Small fibre diameter Easily machined Relatively cheap Conductive Low thermal expansion
Aramid (Kevlar®)	Very high tensile strength Moderate elastic modulus Low density High strain to failure Poor compression and shear strength Difficult to machine Absorbs moisture

Table 2.3. Summary of common fiber materials. [Bond, 2005]

Foams or cellular materials have also been investigated for blast mitigation. Ma and Ye [2007] investigated ultra-light and non-flammable metallic foam materials for use as sacrificial claddings. These foams were able to undergo large deformation at nearly constant nominal stress, absorbing remarkable energy by plastic deformation. They describe the compressive deformation of the metallic foams into three regions: a linear-elastic region, a plateau region and a densification region. It is interesting to note that cellular materials reduce blast loads if the external load is below a certain value, when external loads became more intensive, the cellular material may reach the densification regime and the pressure transmitted to the

protected structure could be enhanced. Therefore, to achieve an effective structural protection, the plateau stress of the foam material should be appropriately selected to match with the resistance of the structure.

New materials continue to be developed for smart structures. Piezoelectric ceramics and films, shape memory alloys (SMAs) and nanotechnology coatings are a few of these cutting edge materials currently being explored in armament applications. Piezoelectric materials deform when an electric field is applied. SMAs are alloys that, after being deformed, can recover their original shape when heated. See Figure 2.6 for an example of a SMA composite. Experiments on composite structures with embedded SMA wires show a significant increase in energy absorbing ability and penetration prevention [Resonance, 2007]. Research has found that SMA fibers were more effective when embedded in more ballistically compatible, higher strain, thermoplastic rubber ECPE resin when compared to embedment in graphite epoxy composites [Ellis, 1996]. The experimental failures resulted from SMA single fiber shear pullout, thus, the SMA did not strain to failure. Nanostructured metals have nanosized grains, which make the metals stronger and harder. Heralded as alternatives to toxic materials like chrome for coatings as well as structural applications, nanostructured metals can be hampered by increased brittleness, nature, and intensive processing requirements. Typical fiber fillers in composites greatly increase the density of the composite, which leads to a decrease in the flexibility and fracture toughness of the polymer [Savage, 2004]. The major advantage of using nanosized grains is that the mechanical properties of the matrix are not negatively affected; in fact tensile strength is often improved.

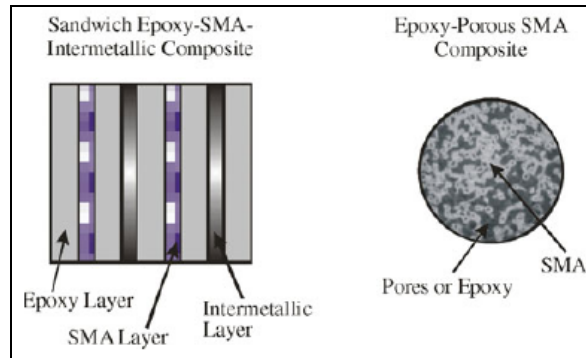


Figure 2.6. Example of hybrid SMAs [Quidwai, 2004]

As a final note on material selection for confinement of a HE explosive event, the containment vessel made of the best material is only as good as the strength of joints. Thus, manufacturing seams and vessel door blast resistance may ultimately prove to be the weakest links.

2.5 Additional Design Considerations

In experiments conducted by Kim, Liu and Crampton [2004] high pressure/FM-200 and hybrid gas generator/FM-200 extinguishing systems successfully provided explosion suppression in armored vehicle crew compartments. The extinguishment of fires has traditionally been attributed to three actions: removal of heat (e.g. water), the physical separation of the fuel and the oxidizer (e.g. foams) or the removal of the oxidizer (e.g. oxygen depletion by carbon dioxide) – physical mechanisms. Halon agents extinguish fires by chemically interacting with key flame species, leading to breaking of the chain reactions of the combustion process – chemical mechanism [Robin, 2007]. The suppressant was rapidly discharged to directly terminate the explosion reaction and flame propagation before a destructive pressure rise was reached. These experiments found the direction of the extinguisher nozzle was important. When nozzles were aimed sideways towards the back of the

compartment, they extinguished the explosion sooner and prevented the re-ignition of the explosion.

The proposed research deals with the detonation/deflagration of a munition, not a fuel fire. In this case, the burning of the energetic material would be unaffected by efforts to separate or remove the oxidizer, since the material is a solid phase burn. Mitigation of thermal and toxic hazards from burning, which is not addressed in this research, is best approached through venting design.

Chapter 3: Injury Criteria

3.1 Background

Since the early 1970's numerous organizations have categorized human injuries to predict survivability during high speed crash events. The American Association for Automotive Medicine's Abbreviated Injury Scale is the most well known. The Federal Aviation Administration, National Highway Traffic Safety Administration, U.S. Air Force, U.S. Army and others have also developed additional significant thresholds and injury criterion. This study uses the U.S. Army Aberdeen Test Center's established injury criteria for mine blast testing of high mobility wheeled-vehicles, as shown in Table 3.1. This multi-criteria method looks to predict the incidence of injury, i.e. only if injury will occur, not the severity of the injury.

3.2 Selected Injury Thresholds

Head Injury Criterion (HIC) is a widely used injury criterion and method for crash test dummy calibration. HIC is based on the impact of the skull to an unyielding surface, such as the windshield, measured as the period of acceleration. Table 3.1 lists the HIC value of 750 to be associated with 5% risk of brain injury. HIC is based on the average value of acceleration over the most critical time period of the deceleration event. Recently a new HIC, called Head Impact Power (HIP) considers not only kinematics of the head for skull rigid body motion, but also the change in kinematic energy which affects non-rigid brain matter. The Dynamic Response Index (DRI) looks at the maximum dynamic compression of the vertebral column. Lumbar Load Criterion addresses maximum compressive loads for

predominant impact parallel to the vertical axis of the spinal column. Neck Injury Criterion (NIC), chest acceleration, femur forces, Thoracic Trauma Index (TTI(d)) are additional criteria for injury assessment.

HYBRID III Simulant Response Parameter	Symbol (units)	Assessment Reference Values
Head Injury Criteria	HIC	750 ~5% risk of brain injury
Head resultant acceleration	A (G)	150 G (2ms)
Neck forward flexion moment	+ My (N-m)	190 N-m
Neck rearward extension moment	- My (N-m)	57 N-m
Chest resultant acceleration	A (G)	60 G (3ms), 40 G (7ms)
Lumbar spine axial compression force	Fz (N)	3800 N (30ms), 6672 N (0ms)
Lumbar spine flexion moment	+ My (N-m)	1235 N-m
Lumbar spine extension moment	- My (N-m)	370 N-m
Pelvis vertical acceleration	Az (G)	15, 18, 23 G (low, med, high risk)
Tibia axial compressive force	F (N)	$F/F_c - M/M_c < 1$
combined with Tibia bending moment	M (N-m)	where $F_c=35,584\text{N}$ and $M_c=225\text{N-m}$
Femur or Tibia axial compression force	Fz (N)	7562 N (10ms), 9074 N (0ms)

Table 3.1. Recommended injury criteria for landmine testing. [Tabiei, 2007]

Fatal injury may occur even if the head, chest and pelvic injury thresholds are not violated. Shrapnel from fragmentation, shattering of bones, and complex loading on non-rigid matter (tissues and organs) as well as thermal and hazardous vapor injuries are just a few additional criteria necessary to understand the overall lethality of the blast environment. Thus head, chest and pelvic integrated effects and accelerations only provide a limited assessment of the risk of severe injury.

Table 3.1 is effective when evaluating landmine injuries because the occupants are assumed to be sufficiently shielded by the vehicle hull. However, in this research, occupants within the vehicle chamber do not have the buffer of a heavy vehicle hull. Additionally, the exposure may include larger magnitude, more complex and prolonged overpressures. Direct blast injuries experienced by rabbits and pigs, shown in Tables 3.2a-b, were produced to evaluate the possible injuries to

humans in the event of a mine explosion. Pigs are very similar to humans in mass and structure of body tissues [Morka, 2005].

<i>Injury</i>	<i>Overpressure Values* [kPa]</i>		<i>Injury</i>	<i>Cutoff ΔP Values* [kPa]</i>	
	<i>Rabbits</i>	<i>Pigs</i>		<i>Rabbits</i>	<i>Pigs</i>
Barotrauma	56	56	Barotrauma	33	113
Mild contusion	134	130	Lung hemorrhage	43	102
Moderate injury	217	237	Lethal (death)	180	880
Heavy injury	280	371			
Lethal injury	490	1074			

*Turin, unpublished materials.

(a)

(b)

Table 3.2. Blast Injuries a) overpressure and b) cutoff ΔP values [Morka, 2005]

The first part of this study uses large steel plates as witness plates, to measure the effects of the blast overpressure (FEA only) and accelerations. The latter part of this study uses a FEM blast-test dummy, described in Chapter 4, to measure head and chest accelerations. This modified blast-test dummy is not correlated for direct-blast. Additionally, Table 3.1 was created for vertical blast loading; this study's main blast loading is horizontal. Therefore, head and chest accelerations were selected as the overarching injury threshold criteria since acceleration effects are universal to the targeted witness nodes and applicable regardless of the blast loading direction.

Chapter 4: Dummy Model for Blast Numerical Analysis

4.1 Background

Since 1949 crash test dummies have been incorporated into the safety analysis and testing of automobiles. The original dummies were unreliable and often inaccurate. In the 1970's new HYBRID dummies were unveiled by General Motors. The HYBRID II was the first dummy to meet the Federal Motor Vehicle Safety Standards (FMVSS). The automotive companies have spent countless hours and funds attempting to make the crash test dummies respond as humanly realistic as possible with accurate and reliable data collection equipment. The physical test HYBRID III dummy has been around since the mid 1970's and the finite element version was expounded in the early 1990's by Lars Fredriksson, this is the most commonly used numerical dummy in automotive crash simulations.

4.2 Dummy Modification

The LSTC HYBRID III finite element dummies are included in LS DYNA as a separate finite element model; this model is a mix of rigid and deformable parts. The HYBRID III dummy used in this simulation has fully deformable parts with the exception of the neck, hands, legs and shoes, which are rigid. The neck is the most difficult to model correctly and still provide correct neck forces and moments. Five calibration tests are simulated and laboratory tested to validate the HYBRID III dummy: head drop test, neck flexion test, neck extension test, thorax ballistic pendulum test and the knee ballistic pendulum test. Masses of the numerical dummy's major assemblies must match the physical dummy. The dummy contact

was provided by extraction of a null-shell from the surface elements of the dummy model. This null-shell provided the “skin” for the contact definition between the other Lagrangian elements and the HE.



Figure 4.1. Overview of dummy model.

Human blast lethality depends on many factors. This research has chosen to restrict the injury criteria to head and chest acceleration. While blast overpressures and accelerations may meet head and chest acceleration tolerance levels, high temperatures, toxic fumes, rupturing of critical arteries, crushing of bones and impalement from shrapnel and other debris can cause life threatening injuries along with many other fatal blast phenomena. At the time of this study, the numerical dummy and dynamic analysis were not capable of measuring these more advanced and refined injuries. A calibrated direct blast-test dummy does not currently exist. The injury criteria listed in Table 3.1 assumes the blast impulse is applied vertically, as appropriate for landmine applications. However, in this study the blast load

impacts the dummy horizontally. Modifications were made to the HYBRID III – 50th percentile rigid dummy allowed for some expository LS DYNA simulations of a dummy subjected to confined blast. The chest and pelvis foam materials were intentionally given very high stiffness. This did not affect the final response of the dummy because the applied load was very high. The head and chest accelerations were determined to be the most appropriate injury criteria to use in this confined blast study. Chapter 9 details the numerical models and results of free field and confined blast on the dummy model.

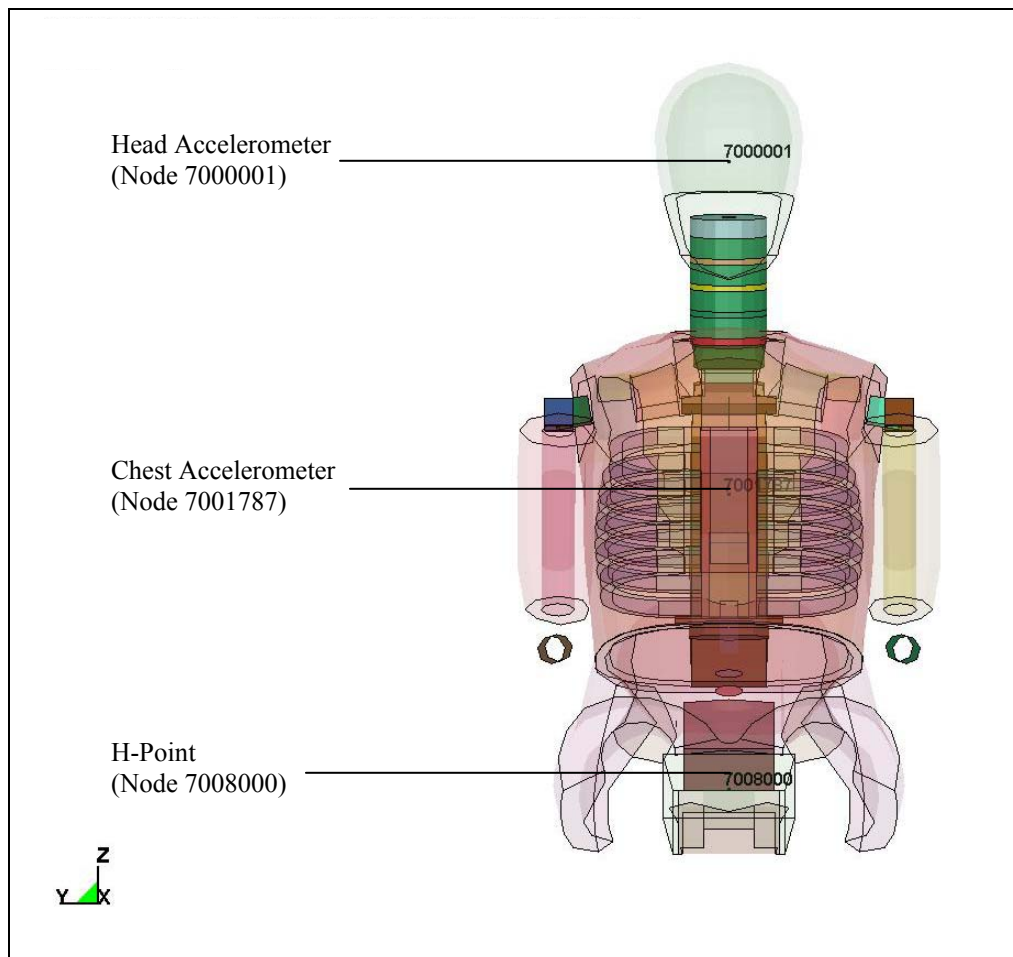


Figure 4.2. Location of acceleration nodes within dummy model, parts hidden.

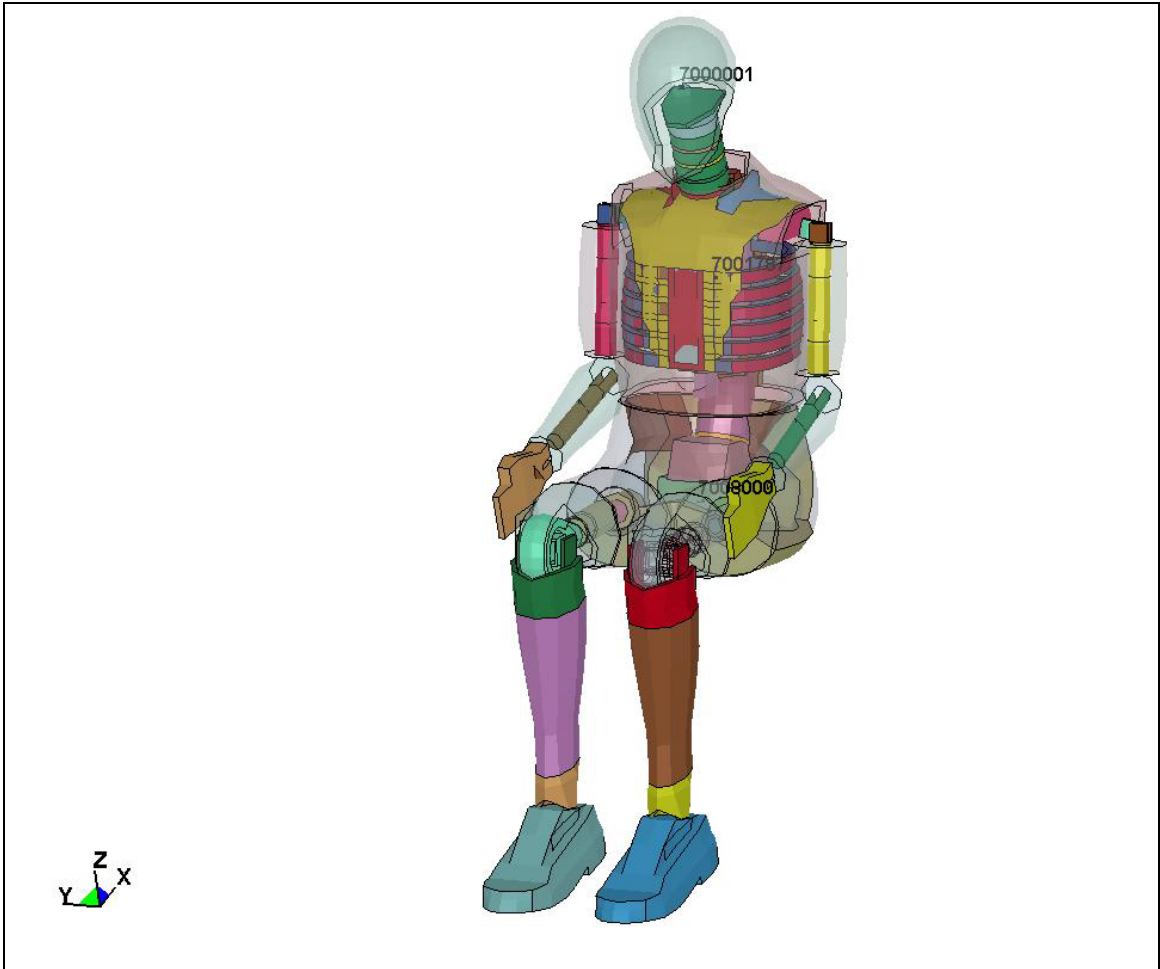


Figure 4.3. Location of acceleration nodes within dummy model.

Excerpt of LS-DYNA code for modifications to the HYBRID-III dummy:

This contains the FE-Chest (P256-P262) and the FE-Pelvis Foam (P263). An Offset of 7000000 has been applied to all IDs. This is a Trial Version for the Special Application of Air Blast Loading. a) This version is still being experimented on. b) The Chest and Pelvis Foam Materials have been intentionally made a lot stiffer than reality to make the job run. However, that does not seem to affect the final response because the applied load is so high. Date of this Release : 11/26/2007 Sarba Guha On behalf of LSTC, Troy, Michigan, USA)

```
*PART
PSHELL      :      1      CQUAD4:BIBURETH
      7000256  7000256  7000256      0  7000256      0
0           0
*SECTION_SHELL
      7000256      2  0.000E+00  0.000E+00  0.000E+00      0
0           0
      3.180E-03  3.180E-03  3.180E-03  3.180E-03  0.000E+00  0.000E+00
0.000E+00  0.000E+00
*MAT_ELASTIC
```

```

7000256 1.140E+03 5.000E+08 3.000E-01 0.000E+00 0.000E+00
*HOURGLASS
7000256          5 0.000E+00          0 0.000E+00 0.000E+00
0.000E+00 0.000E+00
*PART
PSHELL   :          1          CQUAD4:RIB
7000257 7000257 7000257          0 7000257          0
0          0
*SECTION_SHELL
7000257          7 0.000E+00 3.000E+00 0.000E+00          0
0          0
2.300E-03 2.300E-03 2.300E-03 2.300E-03 0.000E+00 0.000E+00
0.000E+00 0.000E+00
*MAT_PLASTIC_KINEMATIC
7000257 7.850E+03 2.050E+11 3.100E-01 6.000E+08 1.000E+04
0.000E+00
0.000E+00 0.000E+00 0.000E+00 0.000E+00
*HOURGLASS
7000257          5 0.000E+00          0 0.000E+00 0.000E+00
0.000E+00 0.000E+00
*PART
PSHELL   :          1          CQUAD4:RIB2
7000258 7000258 7000258          0 7000258          0
0          0
*SECTION_SHELL
7000258          7 0.000E+00 3.000E+00 0.000E+00          0
0          0
2.000E-03 2.000E-03 2.000E-03 2.000E-03 0.000E+00 0.000E+00
0.000E+00 0.000E+00
*MAT_PLASTIC_KINEMATIC
7000258 7.850E+03 2.050E+11 3.100E-01 6.000E+08 1.000E+04
0.000E+00
0.000E+00 0.000E+00 0.000E+00 0.000E+00
*HOURGLASS
7000258          5 0.000E+00          0 0.000E+00 0.000E+00
0.000E+00 0.000E+00
*PART
PSOLID   :          1          CHEXA :RIB_DAMP
7000259 7000259 7000259          0 7000259          0
0          0
*SECTION_SOLID
7000259          2          0 0.000E+00
*MAT_VISCOELASTIC
$      259 1.8460E-6 0.333300 0.110000 0.025300 0.200000
$$     259 1.7000E-6 0.333300 0.110000 0.025300 0.200000
7000259 1.700E+03 3.333E+08 1.100E+08 2.530E+07 1.500E+02
*HOURGLASS
7000259          5 0.000E+00          0 0.000E+00 0.000E+00
0.000E+00 0.000E+00
*PART
PSHELL   :          1          CQUAD4:RIB
7000260 7000260 7000260          0 7000260          0
0          0
*SECTION_SHELL
7000260          7 0.000E+00 3.000E+00 0.000E+00          0
0          0

```

```

2.300E-03 2.300E-03 2.300E-03 2.300E-03 0.000E+00 0.000E+00
0.000E+00 0.000E+00
*MAT_PLASTIC_KINEMATIC
$      260 7.8500E-6 205.00000 0.310000 0.600000 1.0000E-5
$$     260 23.550E-6 205.00000 0.310000 0.600000 1.0000E-5
      7000260 2.747E+04 2.050E+11 3.100E-01 6.000E+08 1.000E+04
0.000E+00
0.000E+00 0.000E+00 0.000E+00 0.000E+00
*HOURGLASS
      7000260          5 0.000E+00          0 0.000E+00 0.000E+00
0.000E+00 0.000E+00
*PART
PSHELL   :          1          CQUAD4:RIB2
      7000261  7000261  7000261          0  7000261          0
0          0
*SECTION_SHELL
      7000261          7 0.000E+00 3.000E+00 0.000E+00          0
0          0
      2.000E-03 2.000E-03 2.000E-03 2.000E-03 0.000E+00 0.000E+00
0.000E+00 0.000E+00
*MAT_PLASTIC_KINEMATIC
$      261 7.8500E-6 205.00000 0.310000 0.600000 1.0000E-5
$      261 11.775E-6 205.00000 0.310000 0.600000 1.0000E-5
      7000261 1.570E+04 2.050E+11 3.100E-01 6.000E+08 1.000E+04
0.000E+00
0.000E+00 0.000E+00 0.000E+00 0.000E+00
*HOURGLASS
      7000261          5 0.000E+00          0 0.000E+00 0.000E+00
0.000E+00 0.000E+00
*PART
PSHELL   :          1          CQUAD4:RIB
      7000262  7000262  7000262          0  7000262          0
0          0
*SECTION_SHELL
      7000262          7 0.000E+00 3.000E+00 0.000E+00          0
0          0
      2.300E-03 2.300E-03 2.300E-03 2.300E-03 0.000E+00 0.000E+00
0.000E+00 0.000E+00
*MAT_PLASTIC_KINEMATIC
$      262 7.8500E-6 205.00000 0.310000 0.600000 1.0000E-5
      7000262 1.177E+04 2.050E+11 3.100E-01 6.000E+08 1.000E+04
0.000E+00
0.000E+00 0.000E+00 0.000E+00 0.000E+00
*HOURGLASS
      7000262          5 0.000E+00          0 0.000E+00 0.000E+00
0.000E+00 0.000E+00
*PART
AbdomenInsertFoam
      7000263  7000263  7000263          0  7000263          0
0          0
*SECTION_SOLID
      7000263          0          0 0.000E+00
$
$$$*MAT_VISCOUS_FOAM
$$$$  7000263 4.500E+02 2.300E+04 3.000E+00 1.500E+04 1.000E+08
4.000E+00 5.000E-02
$

```

```
*MAT_LOW_DENSITY_FOAM
$ 7000263 4.500E+02 5.000E+06 7000009 1.000E+10 1.000E+00
0.000E+00 0.000E+00
  7000263 4.500E+02 25.00E+06 7000057 1.000E+10 1.000E+00
0.000E+00 0.000E+00
  0.000E+00 0.000E+00 0.000E+00 0.000E+00 0.000E+00 0.000E+00
0.000E+00
$
*HOURGLASS
  7000263 7 1.000E-01 0 0.000E+00 0.000E+00
0.000E+00 0.000E+00
.
.
.
.
*END
```

Chapter 5: Mitigation Compartment Shape Study

To understand the role of geometry during confined blast, three simple shapes were examined. As stated previously, compartment performance is found to largely depend on the construction methods used in manufacturing the compartment, e.g. the behavior of welded and bolted seams. The structural joints of this study's hypothetical mitigation compartments were modeled as continuous material, no weld or bolt failure criteria were used. While this is a manufacturing impossibility, it allowed for pure shape comparison due to the internal shock interactions without the uncertainty of seam strength.

5.1 Numerical Model

Keeping the volume constant at one cubic foot, a cube, sphere and cylinder compartment of $\frac{1}{4}$ inch thick RHA were subjected to the detonation of an explosive (HE) spherical charge. RHA was chosen for this study based on the findings from Cheng and Quan's [1998] analysis of unvented compartments subjected to blast loading.

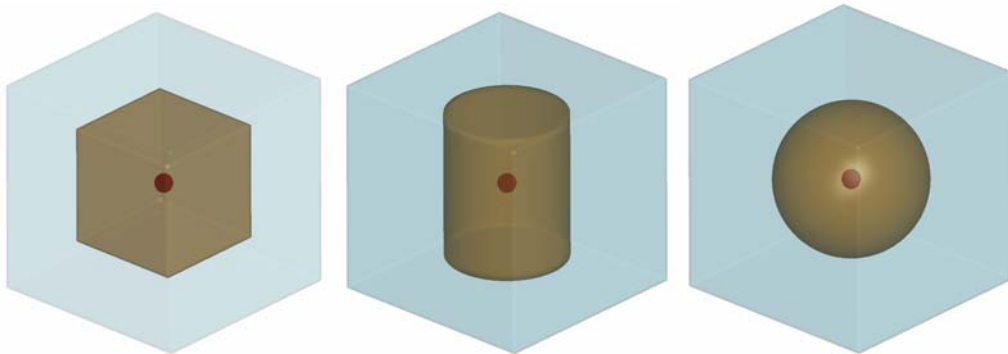


Figure 5.1. Shape study mitigation compartments.

Shape	Dimension	Mass (lbs)
Cubic Box	12 in x 12 in x 12 in	61.1
Cylinder	6.055 in radius, 15 in height	56.7
Sphere	7.44 in radius	49.2

Table 5.1. Shape study compartment statistics.

The Lagrangian elements (mitigation compartment) and multi-material ALE elements (HE and air) were coupled using the LS DYNA's penalty-based algorithm `CONSTRAINED_LAGRANGE_IN_SOLID`. HE was modeled as `*MAT_HIGH_EXPLOSIVE_BURN` with the equation of state (EOS) defined as `EOS_JWL`. Air was modeled as `*MAT_NULL` defined by `EOS_LINEAR_POLYNOMIAL`. Mitigation compartment was modeled as `*MAT_PLASTIC_KINEMATIC` with the material properties of RHA. Mesh densities for each mitigation compartment are summarized in Table 5.2. Air ALE elements had an edge length of 10 mm, HE ALE elements had a max edge element length of 20 mm. The cubic compartment Lagrangian elements had an edge length of 10 mm, the cylinder and sphere Lagrangian elements had edge lengths of 20 mm. The ALE mesh extended from the center of the charge to at least 100 mm surrounding the compartment. A full model, no symmetry, was run for all cases in LS DYNA. A dual CPU considerably reduced the computational total run time. The simulations were terminated after 5 msec, as the initial response of the compartments was adequately demonstrated after this time interval.

ALE	No. Of Nodes	185629
	No. Of Elements	176048 (HE = 53)
	No. Of Materials	2
	HEXAGONS	176048
Cubic	No. Of Nodes	5402
	No. Of Elements	5400
	No. Of Materials	1
	QUAD. ELEMENTS	5400
Cylinder	No. Of Nodes	1538
	No. Of Elements	1536
	No. Of Materials	1
	QUAD. ELEMENTS	1536
Sphere	No. Of Nodes	1538
	No. Of Elements	1536
	No. Of Materials	1
	QUAD. ELEMENTS	1536

Table 5.2. FEM summary of shape study

5.2 Results

Select results from this study are presented below. Internal (IE) and kinetic (KE) energy plots compare the energy absorbing performance of each compartment shape. Since energy is mass dependent, to examine the pure geometric effects of the compartment the y-axis of Figure 5.2 is normalized by the mass of each compartment. The spherical compartment most rapidly absorbs and dissipates the blast energy as shown in the IE and KE plots below, followed by the cylindrical and cubic shapes.

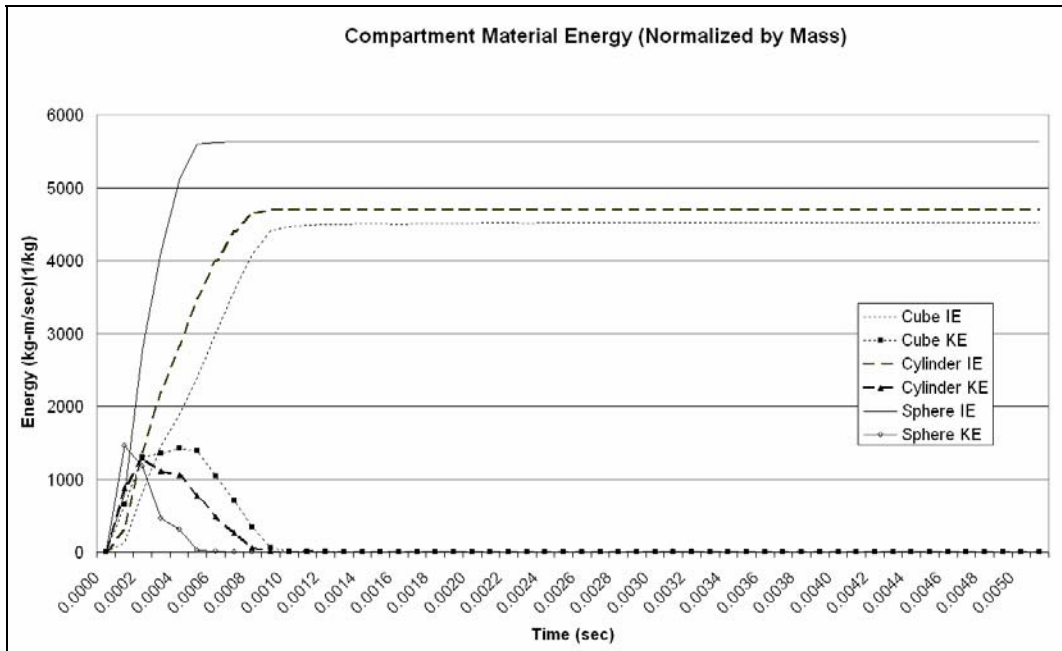


Figure 5.2. Compartment material energy, normalized by mass.

Animations of the pressure contours during the period of 5 msec show several peak pressures occurred within the compartments. The first peak pressure can be attributed to the momentum transferred from the HE and the subsequent peaks from the reflecting overpressures. Figures 5.3, 5.4, and 5.5 show the overpressure contours of the mitigation compartment at the time of peak element overpressure occurring within the first 5 msec. The peak pressure locations imply that the results are highly dependent on the Eulerian mesh used. Figure 5.5 demonstrates this finding most clearly; with a spherical charge perfectly centered in the spherical compartment, one would expect the compartment wall elements to all reach their maximum peak overpressure simultaneously. However, the blast wave propagation through the Cartesian space of air results in small numerical approximations, reshaping the spherical blast wave into a more angular shaped wave front. Therefore, the following

overpressure and strain rate results must be evaluated with acknowledgment of this numerical approximation error.

The cubic compartment reaches a maximum peak elemental overpressure of $1.775e+08 \text{ kg/m}^2$ at 0.001 sec, see Figure 5.3. The corner elements experience the highest overpressures in the cubic compartment. The cylindrical compartment reaches a maximum peak elemental overpressure of $1.28e+08 \text{ kg/m}^2$ at 0.0016 sec, see Figure 5.4. The top and bottom center elements experience the highest overpressures in the cylindrical compartment. The spherical compartment reaches a maximum peak elemental overpressure of $6.5e+07 \text{ kg/m}^2$ at 0.0005 sec, see Figure 5.5. Note the eight evenly distributed elements that experience the highest overpressures in the spherical compartment, which as stated previously, show the numerical approximation error of the pressure wave propagation through the Cartesian air mesh. The cubic compartment experiences overpressures 2.7 times higher than the spherical compartment. The cylindrical compartment experience overpressures nearly two times higher than the spherical compartment. The time of these peak elemental pressures draws attention to the effects of rebounding pressure waves and edge effects. Notice spherical peak element overpressure occurs at 0.0005 sec, where as the cubic and cylindrical peak elemental overpressures occur much (relatively) later. This time variance may be attributed to the sharp corners and stand-off differentials of the compartment walls as based on the geometry of the shape. The variance may also be attributed to the numerical error created by the air mesh as described above.

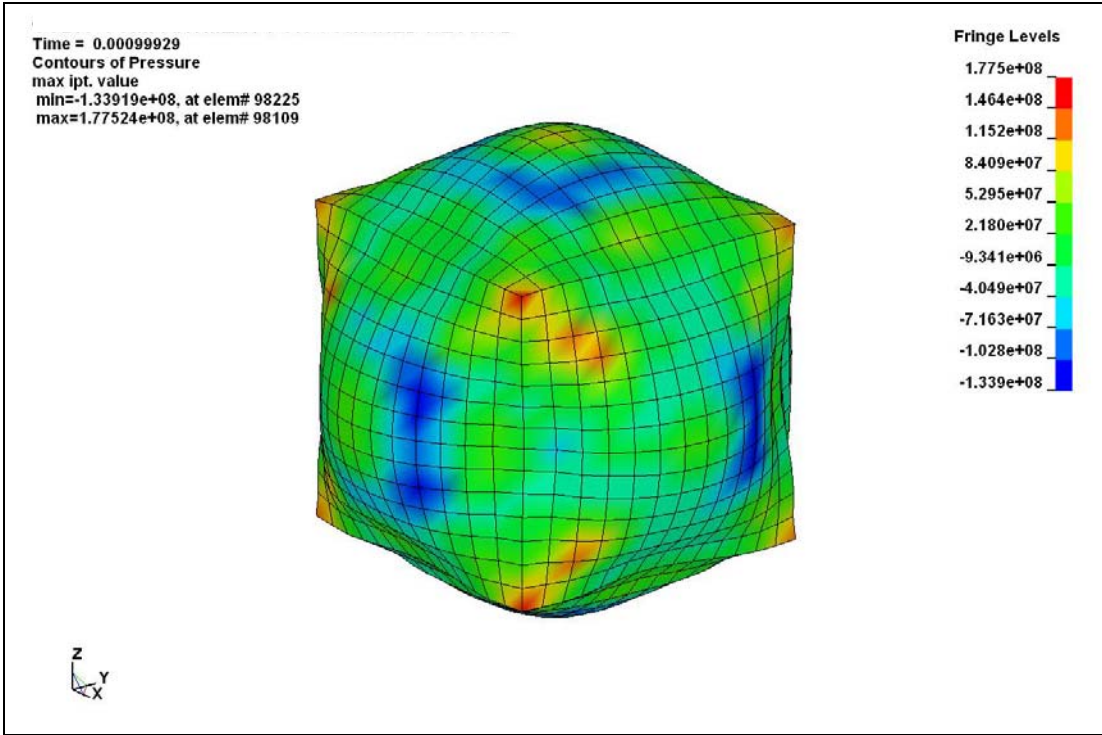


Figure 5.3. Cubic compartment maximum element pressure snapshot.

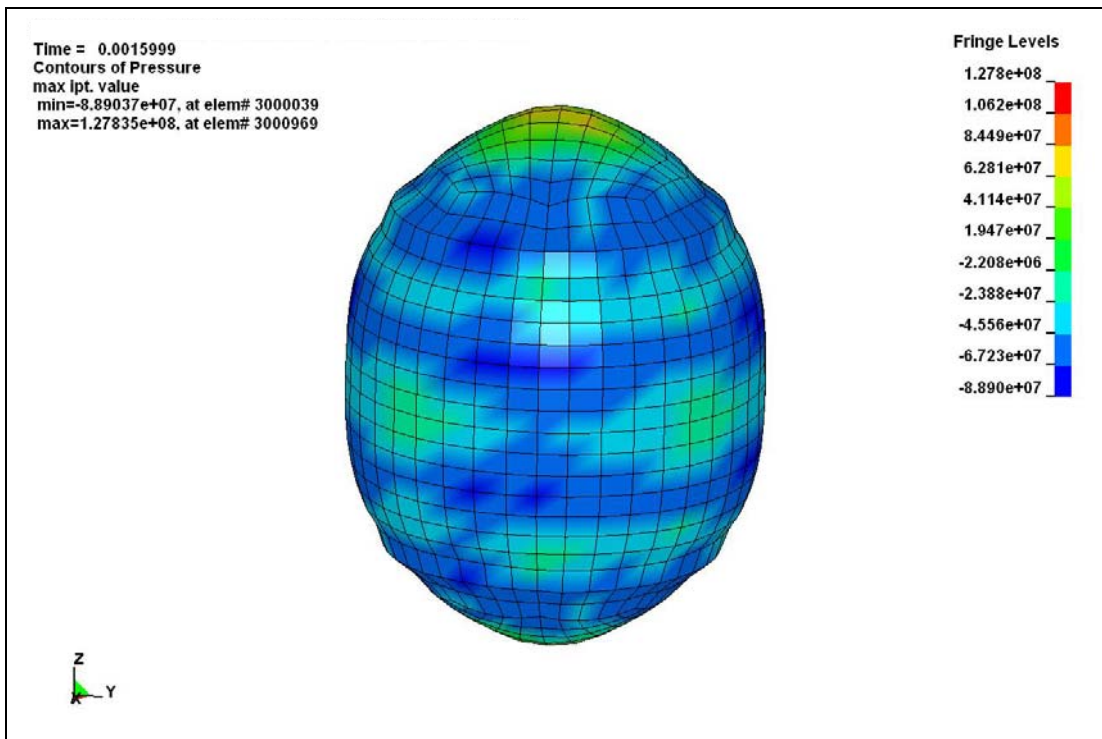


Figure 5.4. Cylindrical compartment maximum element pressure snapshot.

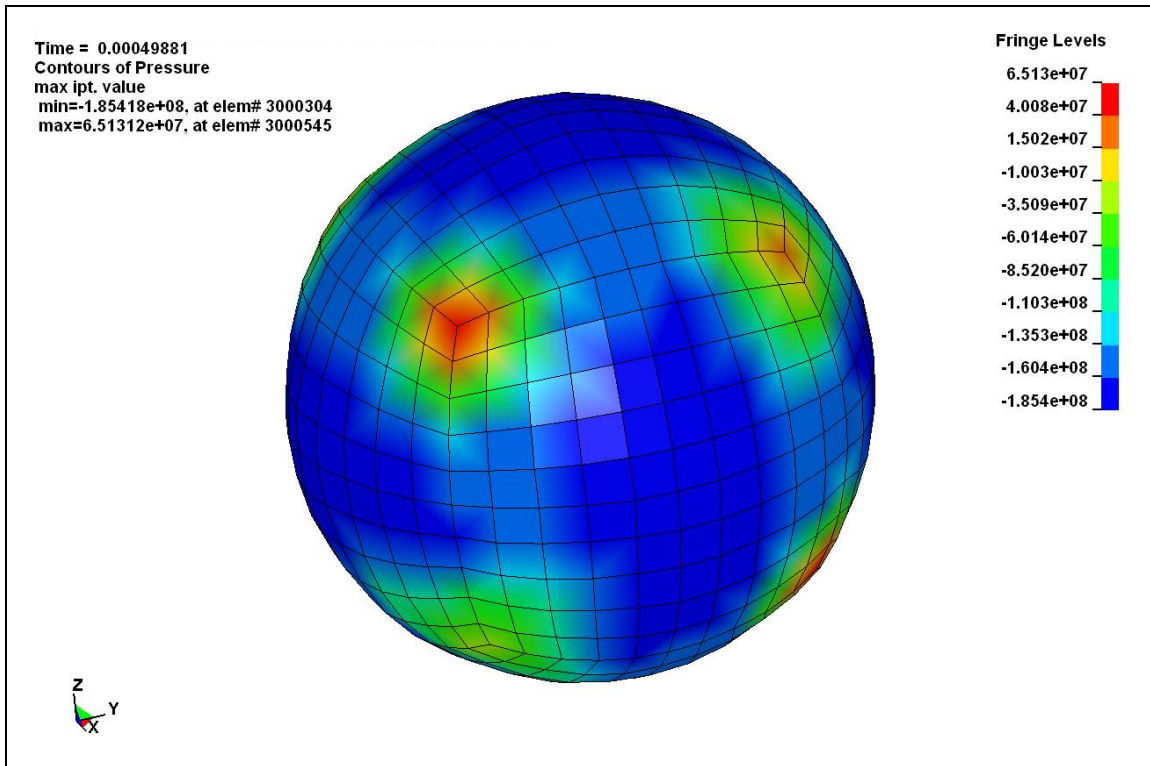


Figure 5.5. Spherical compartment maximum element pressure snapshot.

Since this numerical study has idealized the construction of the mitigation compartments, it is important to note the location of maximum overpressure is not necessarily the location of failure. Indeed, it is the common locations of seams and welds that experience the greatest plastic strains, see Figures 5.6 – 5.8. All three compartments reached their maximum strain values within the first millisecond. The maximum strain of the cubic compartment is 0.518, the maximum strain of the cylindrical compartment is 0.411, and the maximum strain of the spherical compartment is 0.332. The membrane behavior of the compartment walls creates localized areas of high plastic strain in the cube and cylinder shapes. The cylindrical shape offers a small advantage over the cubic shape with the minor savings of 5 lbs of weight for this particular one cubic foot volume compartment. Note the large deformation of the compartments, this highlights that material failure is to be

expected in a non-idealized, real-world scenario at these manufacturing junctures.

The strain values calculated are for a fictitious seamless RHA material.

Incorporation of highly variable weld material or bolted connections will dominate the failure performance of the compartment. Figures 5.6-8 should be evaluated in terms of this idealized material performance. Plastic strain is very unlikely to fully develop in the locations shown since the extent of deformation prior to compartment failure will be considerable less in reality. However, the contours of effective plastic strain shown in the cubic, spherical and cylindrical compartments below emphasize the impact of compartment geometry on the occurrence of localized pressure effects. The ability to deform without failure allows a compartment to reach its maximum energy absorbing potential. The development of localized, concentrated pressures and strains increases the risk of material failure.

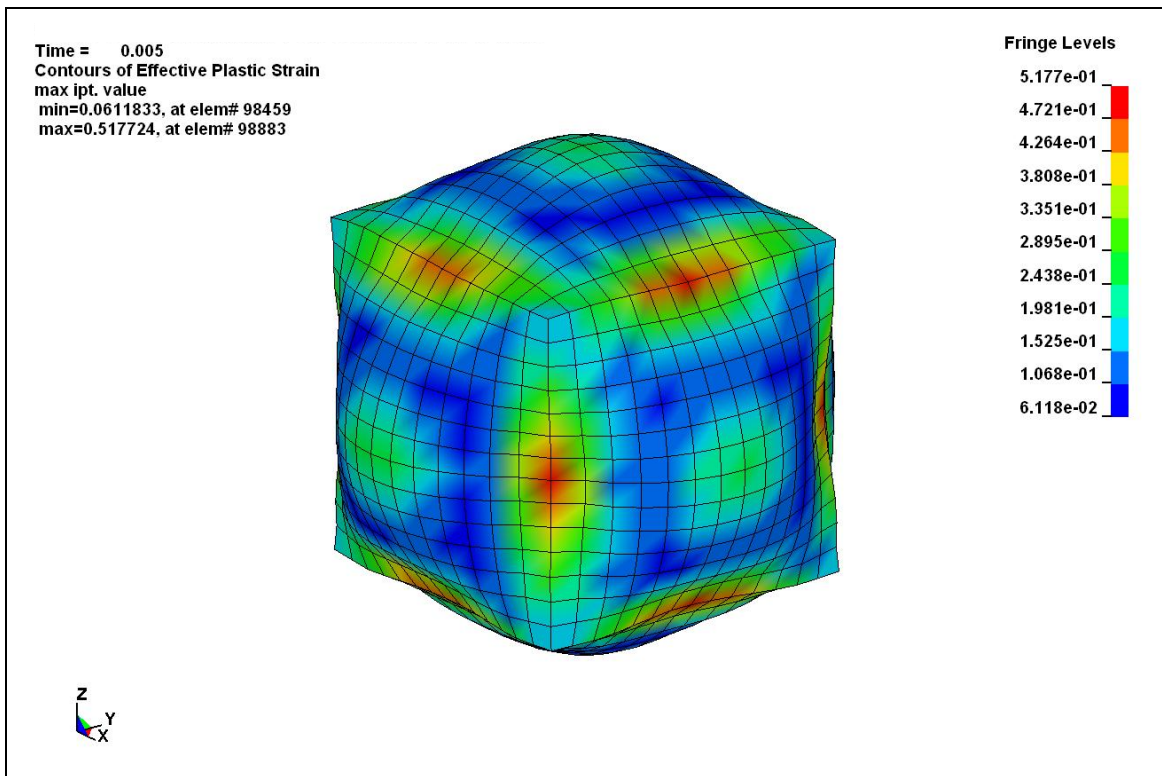


Figure 5.6. Cubic compartment plastic strain at 5 msec.

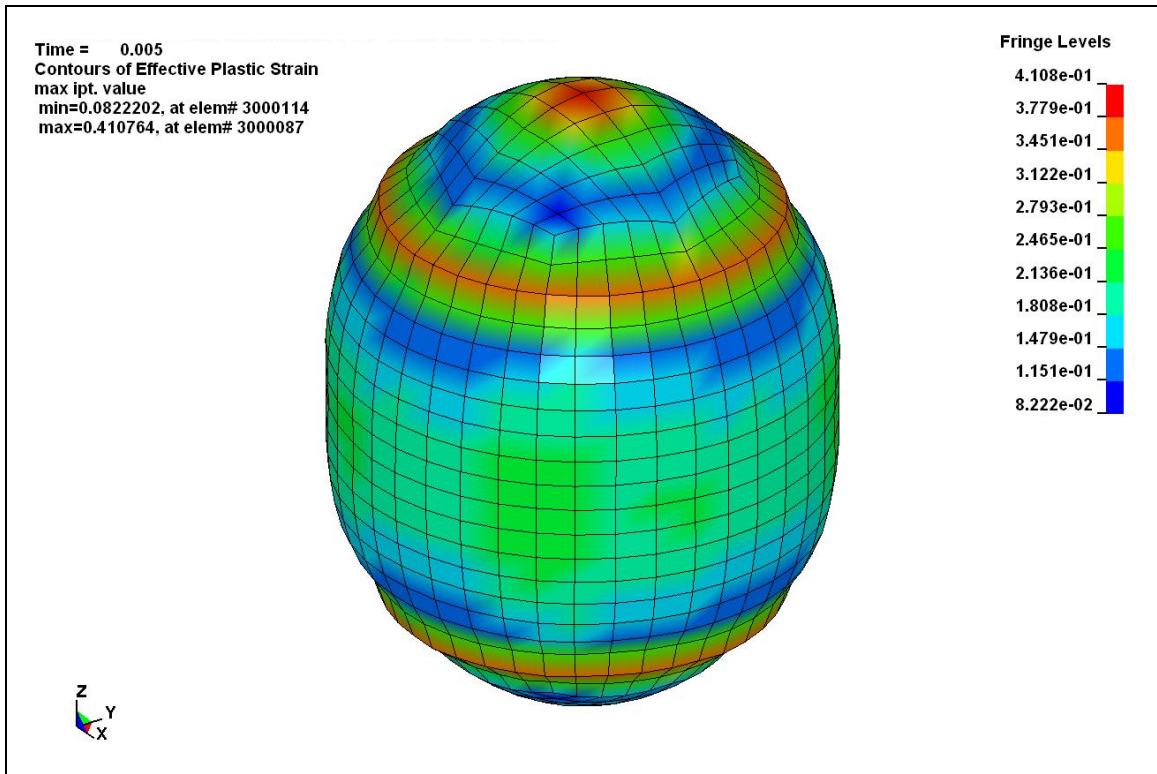


Figure 5.7. Cylindrical compartment plastic strain at 5 msec.

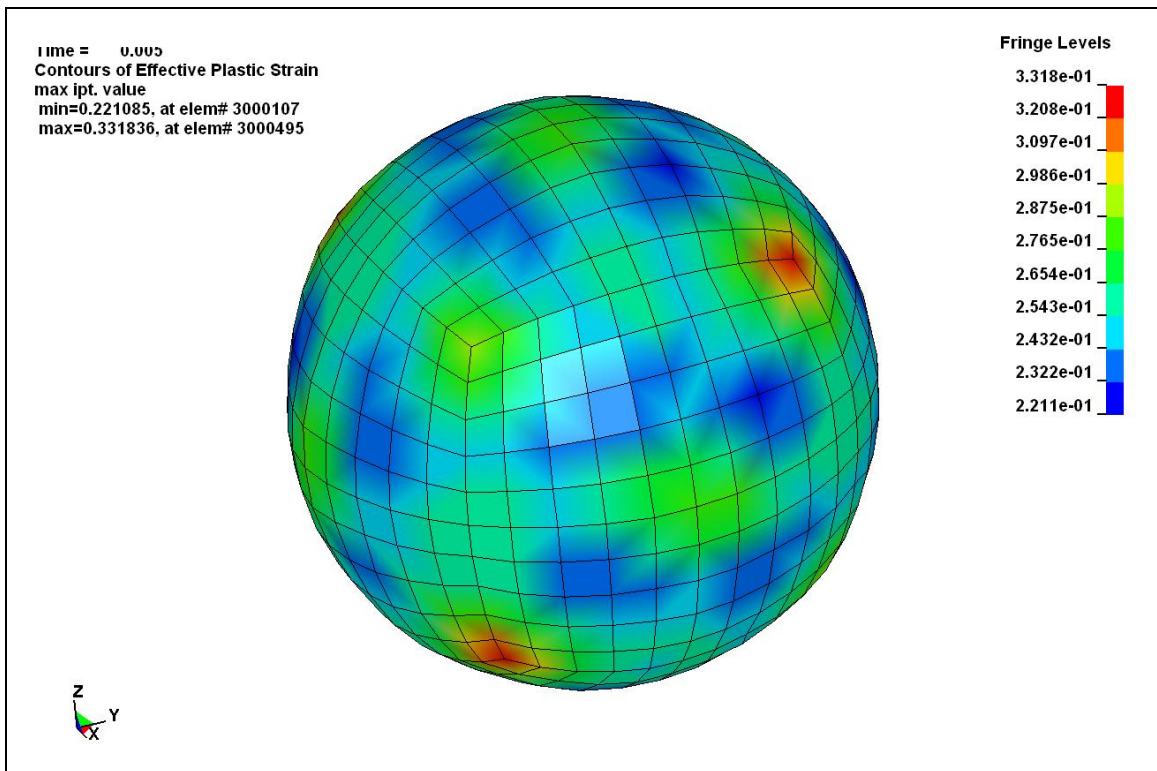


Figure 5.8. Spherical compartment plastic strain at 5 msec.

5.3 Conclusion

The purpose of this study was to examine the performance of three different mitigation compartment geometries of equal containment volume. The analysis was performed using the numerical code of LS DYNA and modeled with ALE techniques and multi-materials. Hypothetical cubic, cylindrical and spherical ¼ inch thick RHA mitigation compartments were subjected to the detonation of an explosive charge. The structural joints of this study's hypothetical mitigation compartments were modeled as continuous material, no weld or bolt failure criteria were used. LS DYNA does not account for heat dissipation to reduce the energy momentum of the HE within the confined space. A spherical Eulerian air mesh could have reduced the pressure wave propagation numerical error by more accurately maintaining the shock front shape.

The spherical compartment most rapidly absorbs and dissipates the blast energy, despite being the lightest weight compartment, followed by the cylindrical and cubic shapes in performance. The spherical compartment experienced overpressures 2.7 times lower than the cubic compartment and 2 times lower than the cylindrical compartment. Both the cubic and cylinder compartments' sharp edges attracted greater relative pressures, "edge-effects". Their flat plate sections' membrane action contributed to the increased material response. The membrane behavior of the compartment walls created localized areas of high plastic strain in the cube and cylinder shapes. These edges would be the location of welded or bolted connections and thus the most vulnerable to manufacturing defects, i.e. the most

unpredictably performing area of the compartment. The strain values calculated were for the idealized seamless RHA material and not for a possibly weaker, highly variable weld material or bolted connection. The greater magnitudes of fluctuating deformation as exhibited in the cubic and cylindrical compartments could also lead to fatigue failure overtime. The spherical compartment exhibited the least amount of deformation. Manufacturing consideration, however, would point to the cubic or cylindrical compartments for easy of construction, despite the better performing and lighter weight spherical compartment. The cylindrical shape offers a small advantage over the cubic shape with a minor savings of 5 lbs of weight for this particular one cubic foot volume compartment. All three compartments reached their maximum strain values within the first millisecond.

Chapter 6: Confined Blast Cylinder and Plate Study

Mitigation structures face amplified stresses when forced to perform within an enclosed space. To distinguish between confining spaces, the name “chamber” is given to the space that the occupant and the mitigation structure are enclosed within. “Compartment” is the title given to the mitigation structure enclosing the explosive. In the following confined plate study, eight cylinders of varying diameter, height and thickness were compared through numerical analysis; see Table 6.1 and Figure 6.1. Cylindrical mitigation compartments enclosed an explosive charge centered within a large 6 ft x 5 ft x 4.5 ft rectangular chamber. The chamber was idealized and considered to be unvented with airtight boundaries. When the overpressure profile is examined for a HE event, direct correlation to an injury scale is not appropriate unless the overpressure is read from a structure appropriate for human scaling. Without the availability of a “blast-test” dummy, large flat plates of equal mass occupied the chamber to provide physical obstruction necessary to review the effectiveness of the mitigation compartment in reducing overpressures and accelerations. The structural joints of this study’s hypothetical mitigation compartments and chamber were modeled as continuous material, no weld or bolt failure criteria were used. LS DYNA does not account for heat dissipation to reduce the energy momentum of the HE within the confined space. Simulations were run with one eighth symmetry to reduce total run time.

The goal of this numerical study was to gain insight into the parameters that affect a mitigation compartment’s performance most appreciably with the greatest

savings in overall weight. The results of this study aided compartment design selections for subsequent analysis and laboratory testing in this research.

Diameter, Height, Thickness (inches)	Mass (kg)		Diameter, Height, Thickness (inches)	Mass (kg)
12 15 1/16	2.263	A	12 15 1/16	2.263
12 15 1/8	4.5133	B	15 15 1/16	2.829
12 30 1/16	4.525	C	12 15 1/8	4.5133
12 30 1/8	9.0267	D	12 30 1/16	4.525
15 15 1/16	2.829	E	15 30 1/16	5.55
15 15 1/8	5.648	F	15 15 1/8	5.648
15 30 1/16	5.55	G	12 30 1/8	9.0267
15 30 1/8	11.295	H	15 30 1/8	11.295

(a) (b)
Table 6.1 Cylinders (a) listed by size (b) listed by mass.

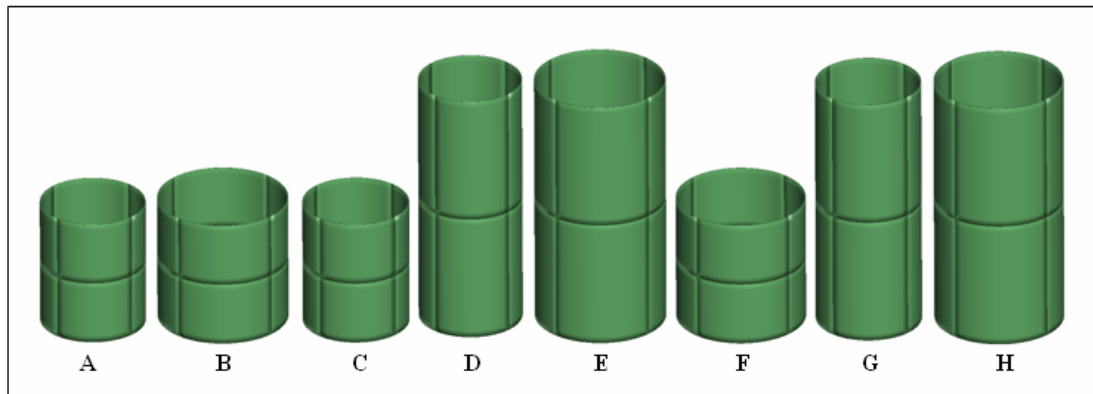


Figure 6.1. Graphical representation of cylinders arranged in order of mass.

6.1 Numerical Model

The Lagrangian elements (plates, chamber and mitigation compartment) and multi-material ALE elements (HE and air) were coupled using the LS DYNA's penalty-based algorithm CONSTRAINED_LAGRANGE_IN_SOLID. HE was modeled as *MAT_HIGH_EXPLOSIVE_BURN with the equation of state (EOS) defined as EOS_JWL. Air was modeled as *MAT_NULL defined by EOS_LINEAR_POLYNOMIAL. Chamber was modeled as *MAT_PLASTIC_

KINEMATIC with the material properties for RHA. Plates and mitigation compartments were modeled as *MAT_SIMPLIFIED_JOHNSON_COOK with the material properties for mild steel. Mesh densities for each mitigation compartment are summarized in Table 6.2.

Air elements had an edge length of 20 mm. The spherical HE elements had a max edge element length of 10 mm. The compartment and plate solid elements had edge lengths of 20 mm. The two inch thick chamber walls were modeled as shell elements with an edge length of 30 mm.

The chamber's overall interior dimensions were 6 ft x 5 ft x 4.5 ft. The mitigation compartment was modeled as free standing, eliminating restrictions to movement or deformation. To simulate the mass of two human occupants, two 150 pound, 29 in x 18 in x 1 in steel plates were positioned 18 inches from chamber center, centered in their respective planes, see Figure 6.2. These plates were modeled with a fixed boundary edge. The ALE mesh extended from the center of the charge to at least 100 mm surrounding the chamber. The one-eighth symmetric model was built using eta/VPG 3.2 and run in LS DYNA, see Figure 6.3. Simulations took approximately 36 to 74 hours each to run. A dual CPU considerably reduced the computational total run time. The simulations were terminated after 10 msec, as the initial overpressure effects within the chamber were adequately demonstrated after this time interval.

ALE	No. Of Nodes	95273
	No. Of Elements	88254 (HE = 54)
	No. Of Materials	2
	HEXAGONS	88254
Chamber	No. Of Nodes	8105
	No. Of Elements	7949
	No. Of Materials	1
	QUAD. ELEMENTS	7949
Cylinder 15" diameter 15" tall 1/16" thick	No. Of Nodes	329
	No. Of Elements	139
	No. Of Materials	1
	QUAD. ELEMENTS	139
Plate	No. Of Nodes	1140
	No. Of Elements	522
	No. Of Materials	1
	QUAD. ELEMENTS	522

Table 6.2. FEM snapshot of the confined plate study

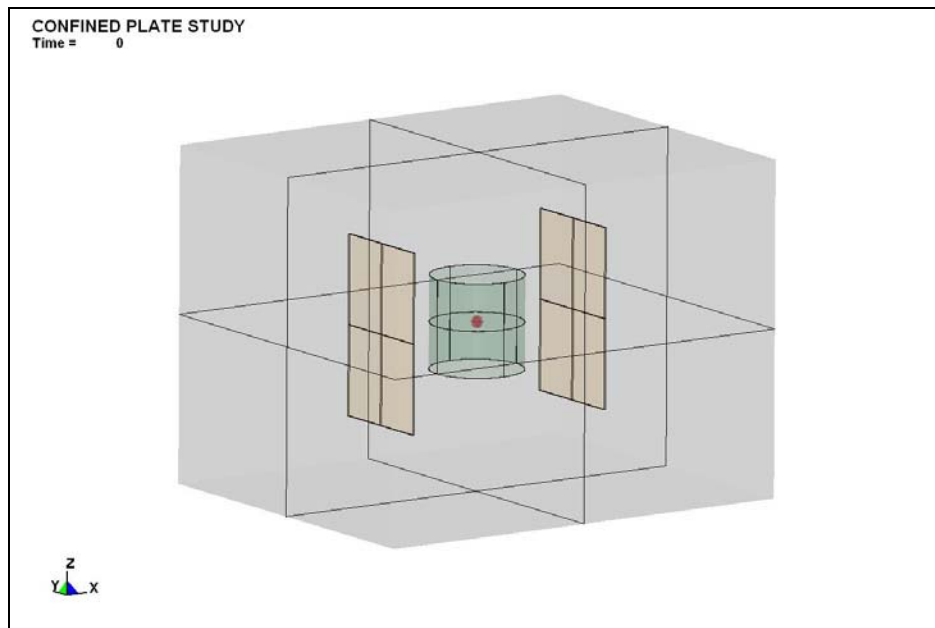


Figure 6.2. Full model represented, air mesh hidden.

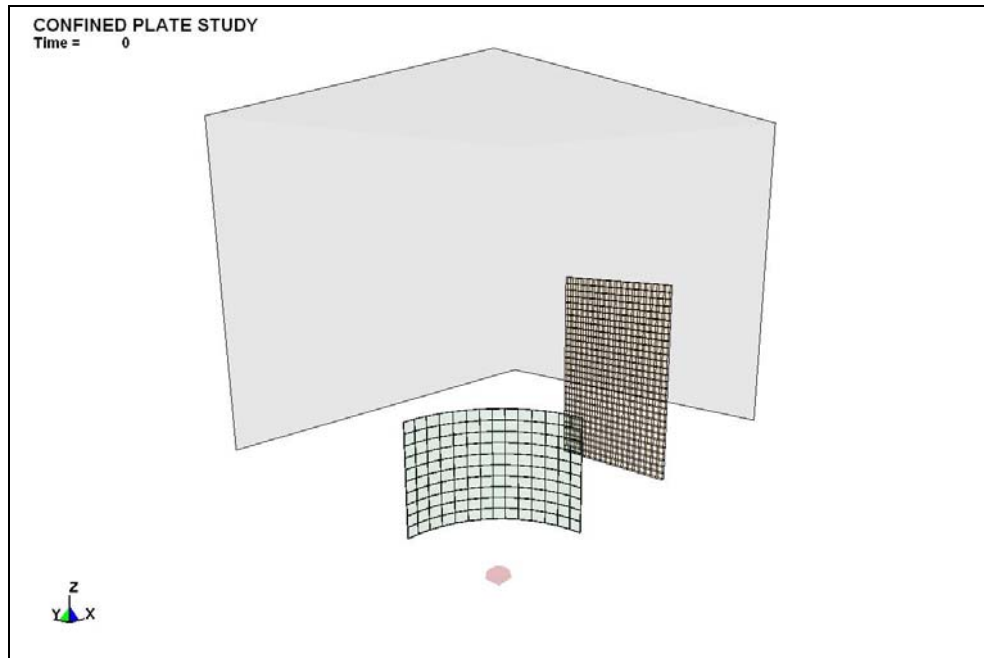


Figure 6.3. One-eighth symmetric model, air mesh hidden.

6.2 Numerical Results

The goal of this numerical study was to gain insight into the parameters that affect a mitigation compartment's performance the most appreciably while achieving the lightest overall weight. The selected compartment(s) will be further examined in laboratory experiments. The three performance criteria are:

- 1) Acceleration witnessed by the midpoint of the plate for consideration with chest acceleration values. (see Table 3.1)
- 2) Peak overpressure and duration witnessed at plate midpoint
- 3) Kinetic energy decay of the cylinder material for energy absorption comparisons

None of the mitigation compartments ruptured. No movement of the cylinders was recorded, an expected outcome based on the symmetric nature of this particular blast scenario, see Figure 6.4.

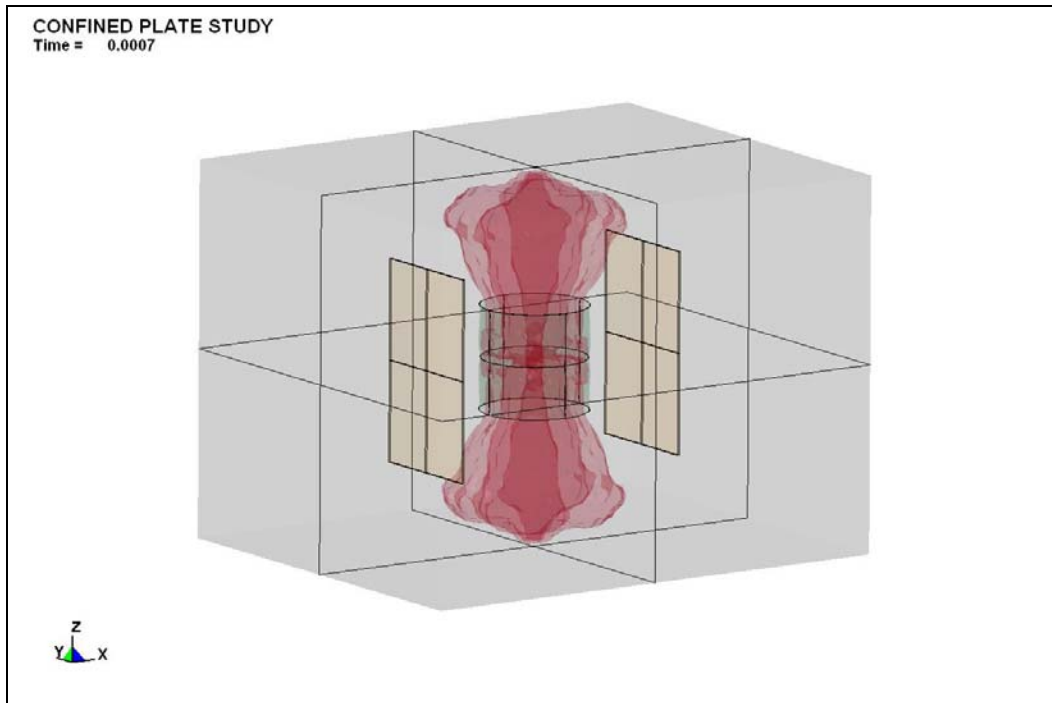


Figure 6.4. Explosive event at $t = 0.0007$ sec, air mesh hidden

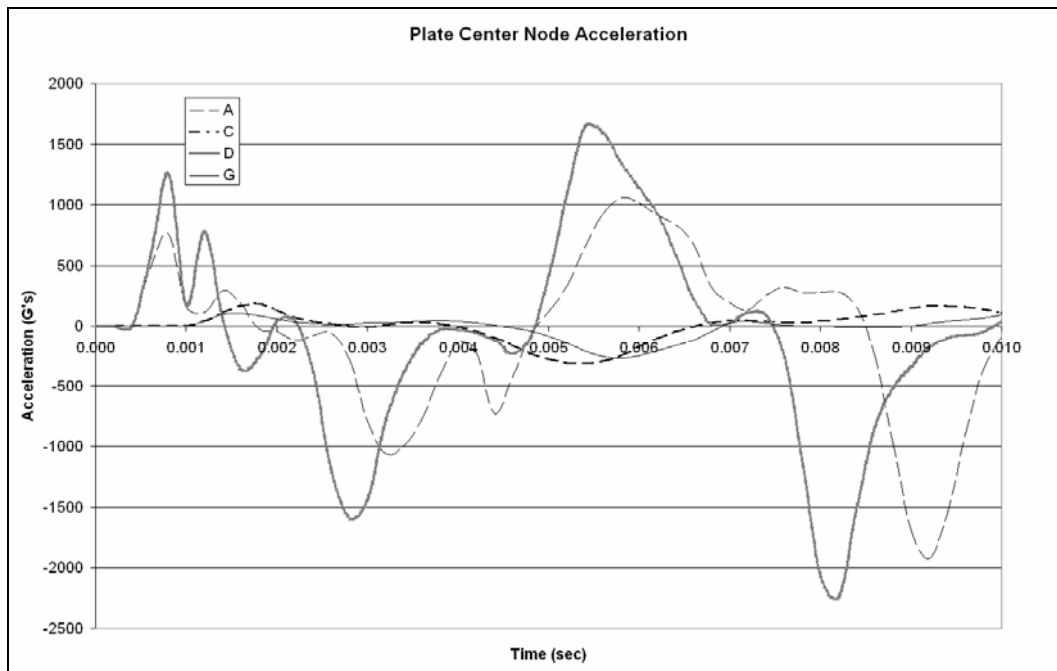


Figure 6.5. Plate acceleration, 12 in diameter cylinders.

From Figure 6.5 the 12 in diameter cylinders of 1/16 in thickness (A and D) perform poorly in reducing plate accelerations. For a constant diameter and

thickness, doubling the height of the mitigation compartment did not reduce plate accelerations nor delay the time of arrival for the 12 in diameter cylinders. Doubling the height of the cylinder even appears to increase the loading applied to the plate for thin walled cylinders. This additional height may have provided additional surface area for shock wave reflection and amplification. The gross differential between these 12 in diameter, 1/16 in thick cylinders and the others, see Figures 6.5 and 6.6, is possibly from the interaction occurring between the cylinder wall deformation and the rebounding pressure waves. This physical movement of the cylinder wall coupled with a shorter distance from the HE to the compartment wall caused magnified reflected pressures to form within the cylinder, thus impacting the plates with higher magnitude and faster moving shock waves. The confined blast environment allows for a greater frequency of Mach wave occurrence, the magnitude of this effect is most noticeable with the smaller 12 in diameter, 1/16 in thick cylinders when compared to the same diameter 1/8 in thick or the same thickness, larger 15 in diameter cylinders.

Cylinders of 1/8 in thickness (C, F, G, and H) perform remarkably similar during the first 10 msec of the blast event, despite variations in the cylinder diameter and height, see Figures 6.5 and 6.6. The 30 in tall, 15 in diameter cylinder (H) reduces the acceleration seen by the plate slightly more than the other 1/8 in thick cylinders. From Table 3.1, the chest acceleration threshold of 60 G's is still moderately violated even by the best performing cylinders. Most notable is the minimal advantage of doubling the cylinder height to reduce the plate mid-point accelerations. This finding is limited to plate mid-point accelerations and conclusions should not be drawn to possible effects on accelerations at differing heights. As the

blast waves reflect and magnify, an increase in the cylinder shielding height would be expected to provide additional mass and surface area to absorb the blast energy, and assist in delaying the blast wave from reaching other locations on the plate. However, a review of the taller cylinders (D, E, G, and H) shows the increased height does little to delay the arrival of the subsequent shock waves to the plate mid-point.

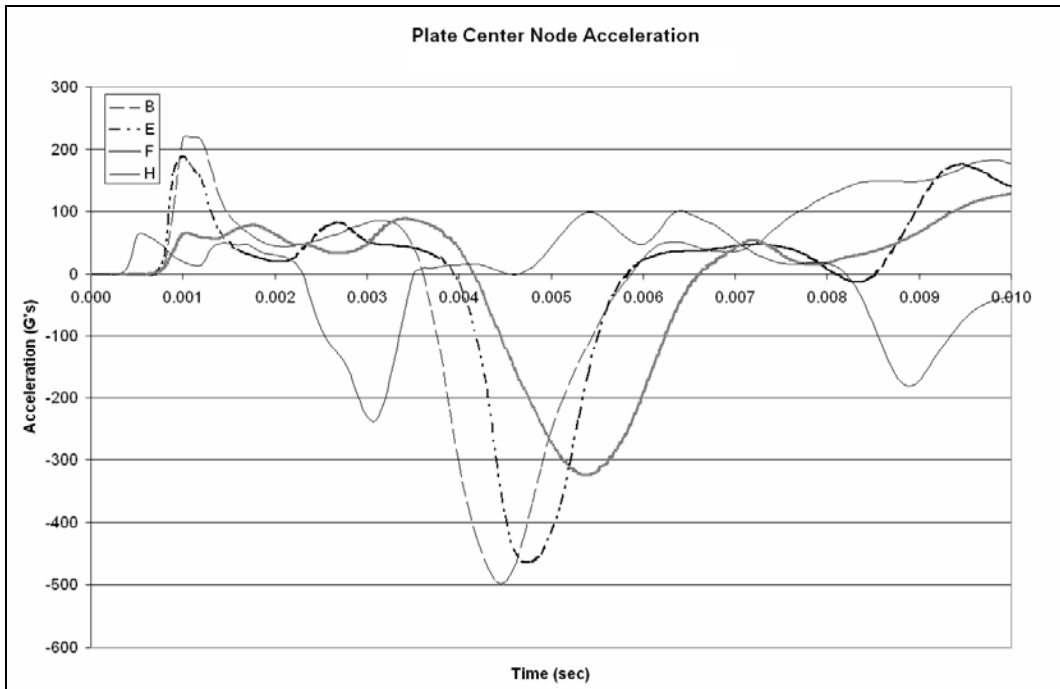


Figure 6.6. Plate acceleration, 15 in diameter cylinders.

Review of Figures 6.7 and 6.8 show the taller cylinders are effective in reducing the overpressures at the plate mid-point for constant diameter and wall thickness, with the exception of the 12 in diameter 1/16 in thick cylinder (D). The narrower 12 in diameter cylinder has the potential to reflect and magnify the shockwaves at a greater rate than the wider cylinders since the stand off distance to the HE is less. These amplified shockwaves are eventually projected out into the chamber to impact the plate. Of concern is the increased frequency and greater

magnitude peak overpressures seen after the initial shock loading, especially with cylinders A and D. In general, the thin walls of the smaller 12 in diameter cylinders produced much larger overpressures than the thicker 1/8 in thick cylinders, regardless of height, see Figure 6.7. When compared to Figure 6.8, the 15 in diameter cylinders did not exhibit this large overpressure variance between the two different wall thicknesses. Plate center overpressures recorded for the 12 in diameter, 1/8 in thick cylinders (C and G) more closely resemble those overpressures seen for the 15 in diameter cylinders. The combination of smaller diameter cylinders and thin walls needs to be further investigated to better understand the cause of the greatly magnified overpressures; and accelerations as discussed above. For cylinders of equal diameter, this overpressure difference is most apparent for the 30 in tall cylinders than for the shorter 15 in tall cylinders. Cylinder wall thickness has more impact on reducing plate overpressures as the height of the compartment increases.

The increase in quasi-static pressure from gaseous vapor release for the size explosive used in this study was calculated to be less than 35 psi based on loading density [as read from Figure 5.18, Bulson, 1977]. Figures 6.7 and 6.8 show a trend of slightly increasing peak overpressures, this maybe attributed to the increase in quasi-static pressure. However, this increase in quasi-static pressure is insignificant when compared with the initial shock loading pressures.

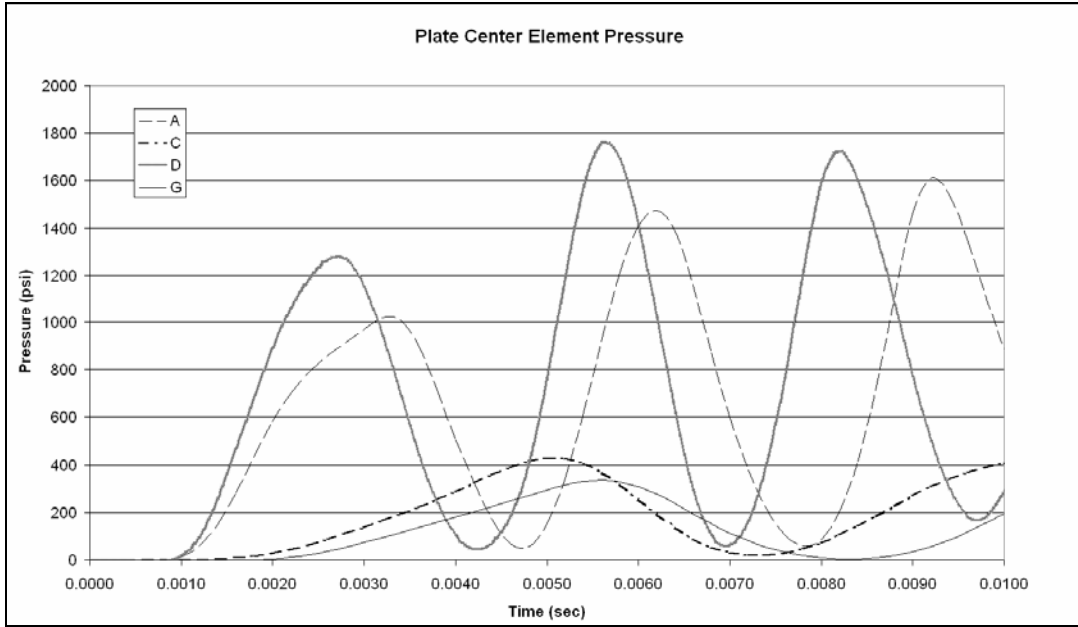


Figure 6.7. Plate center element overpressure, 12 in diameter cylinders

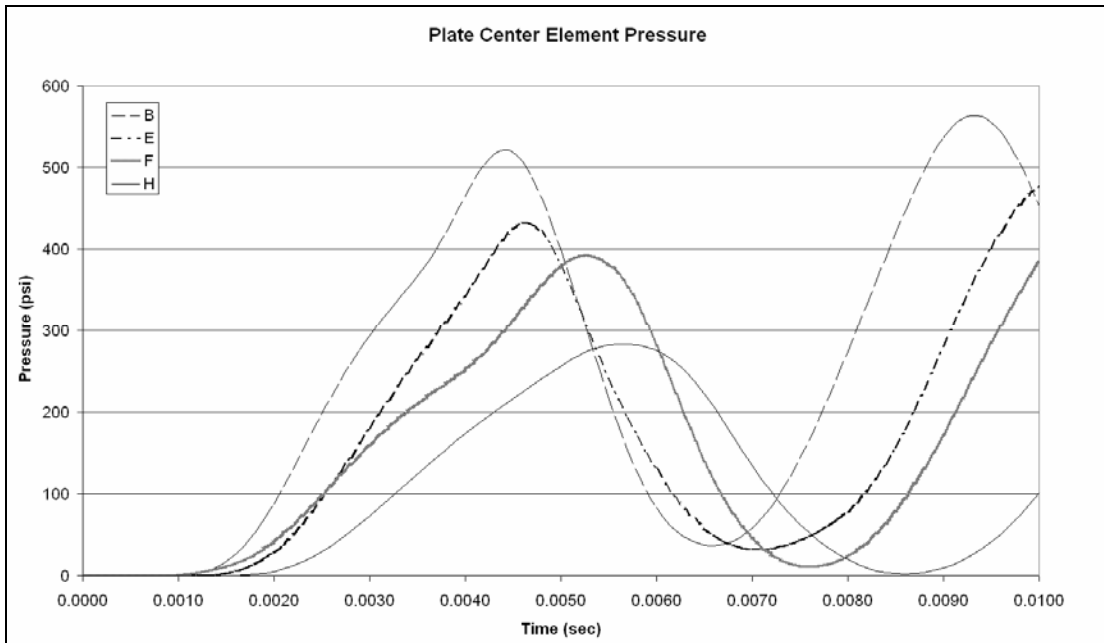


Figure 6.8. Plate center element overpressure, 15 in diameter cylinders.

Since kinetic energy is mass dependent, it is expected that heavier cylinders will absorb a greater amount of blast energy than lighter cylinders. Normalizing the kinetic energy plots by cylinder mass allows comparison of cylinder diameter, height

and thickness without regard to these increased mass effects. Examination of the kinetic energy plots, see Figures 6.9 and 6.10, for each cylinder shows the thin walled cylinders (A, B, D and E) achieved the greatest levels of kinetic energy. These thin walls deformed more easily, directly absorbing the energy of the blast. Recall that blast energy is directly related to the distance from the HE; therefore, the 12 in diameter cylinder's closer proximity to the blast allowed for increased energy absorption opportunity. The larger diameter cylinders also allow more incident shock waves to escape out of the top and bottom of the cylinder without impinging the cylinder walls, thus lower kinetic energies are achieved. The narrow, 12 in diameter cylinders took slightly longer to return back to their equilibrium state.

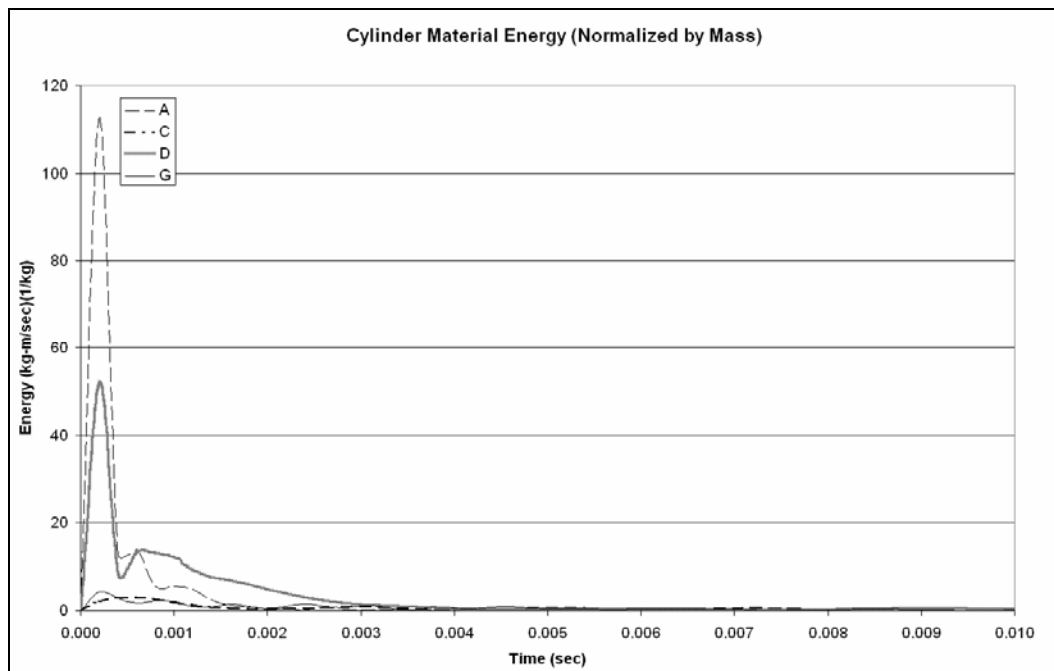


Figure 6.9. 12 in diameter cylinder material kinetic energy, normalized by mass.

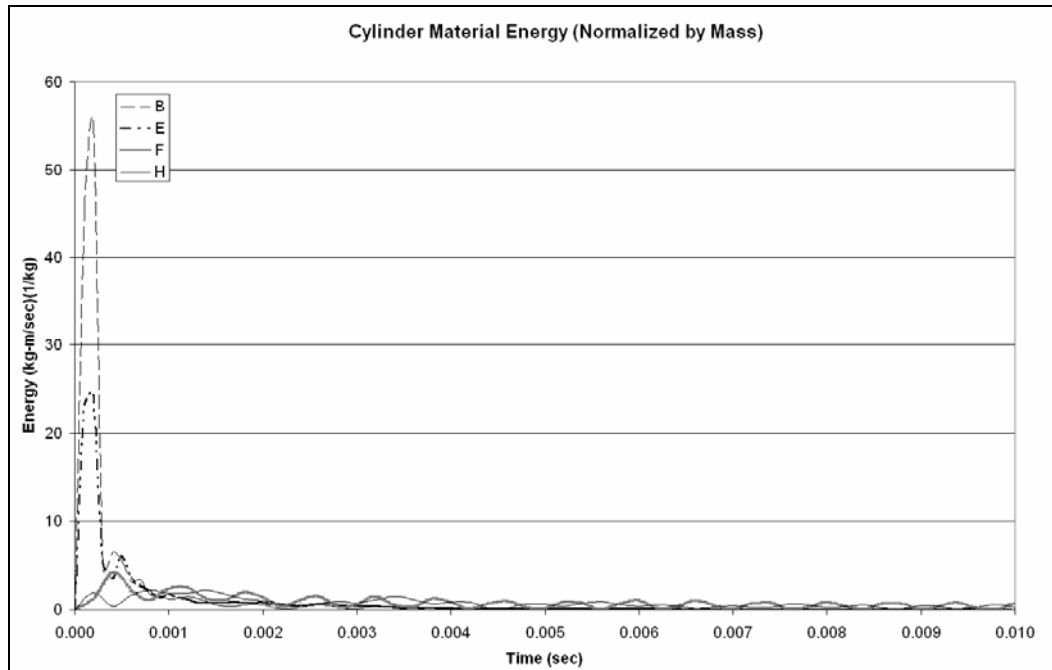


Figure 6.10. 15 in diameter cylinder material kinetic energy, normalized by mass.

6.3 Conclusion

The numerical analysis of eight cylinders of two different thickness, two different heights and two different diameters provides greater insight into how a mitigation compartment geometric properties can affect the confined blast environment within the chamber.

Compartment wall thickness reduced the plate's mid-point acceleration and overpressures with greater efficiency than the effects of the cylinder height or diameter. The thicker, 30 in tall, cylinders (G and H) reduced the plate center node accelerations the greatest. Most notable is the minimal advantage of doubling the cylinder height in comparison to doubling the wall thickness. The overpressure experienced by the 150 lb plate at mid-point was best mitigated with the larger diameter, thicker, 30 in tall cylinder (H). The lighter weight cylinders did not reduce the plate overpressures as effectively as the heavier cylinders (G and H). The thin,

smaller diameter, cylinders reached the greatest kinetic energy levels, thus implying the greatest energy absorbing capabilities. Again, the thickness of the cylinder was more important to energy absorption than height. Venting effects also must be considered when comparing the energy absorption capabilities of the cylinders, since the larger diameter cylinders allow more of the initial shock front to escape without impinging the compartment walls. Thus, while the energy absorbing potential of the thin walled cylinders are the greatest, these cylinders performed the least favorable in protecting the plates from high accelerations and overpressures for this particular scenario. This highlights the necessity to study blast effects on nearby structures and personnel in addition to evaluating the performance of the mitigation compartment itself.

Chapter 7: Free Field Blast Cylindrical Mitigation Study

From Chapter 6's numerical analysis comparison, cylinders of at least 1/8 in thickness were chosen for further investigation and field testing. To obtain industry standard cylinders without welded seams for field testing, mild steel schedule 5s tubing was selected. The numerical analysis cylinder dimensions were modified to the following:

Outside diameter	Inside diameter	Thickness	Weight (lb/ft)
10.750 in	10.482 in	0.134 in	15.19
12.750 in	12.420 in	0.165 in	22.18

Table 7.1. Free field cylinder dimensions.

Both cylinders were field tested at heights of 15 inches. Unfortunately only the 10.75 in diameter pressure data was successfully retrieved from the scopes. Therefore, direct comparison of pressures between numerical and field results is limited to this cylinder.

The goals of this study were to ensure the selected cylinders would not rupture for the selected HE size and to assess the FEA correlation with laboratory tests.

7.1 Numerical Model

The Lagrangian elements (cylinder) and multi-material ALE elements (HE and air) were coupled using the LS DYNA's penalty-based algorithm `CONSTRAINED_LAGRANGE_IN_SOLID`. HE was modeled as `*MAT_HIGH_EXPLOSIVE_BURN` with the equation of state (EOS) defined as `EOS_JWL`. Air was modeled as `*MAT_NULL` defined by `EOS_LINEAR_POLYNOMIAL`. Mitigation compartments were modeled as `*MAT_SIMPLIFIED_JOHNSON_COOK`

with the material properties for mild steel. The 1 in thick, 12 in x 36 in test stand was modeled as *MAT_PLASTIC_KINEMATIC with the material properties for RHA

Air ALE elements had an edge length of 20 mm, HE ALE elements had a max edge element length of 10 mm. The compartment and test stand solid elements had edge lengths of 20 mm. Mesh densities for each mitigation compartment are summarized in Table 7.2. A full model, no symmetry, was run for both cases in LS DYNA.

The mitigation compartment was positioned 1 in above the test stand with restriction to top and bottom edge movement and deformation, see Figure 7.1, to coincide with the experimental set-up which included a 1 in thick foam pad between the cylinder and test stand to permit compartment deformation, see Figure 7.8 . Incident pressures were measured 30 inches from the charge center; location “Gage 1” is located over the open end of the cylinder and location “Gage 2” is located at cylinder mid-height. Since this simulation was for free field blast, the blast waves flowing out of the ALE mesh were not of interest. Therefore, the air mesh extends unequally over the top and sides of the cylinder to reach the necessary 30 in stand-off distances to include the pressure measurement locations while minimizing the ALE domain size, see Figures 7.1 and 7.2. Even with this restricted ALE mesh domain the simulation took two weeks to run. A dual CPU considerably reduced the computational total run time (335 hours). The simulations were terminated after 8 and 10 msec, as the initial overpressure response of the compartments was adequately demonstrated after this time interval.

ALE	No. Of Nodes	315153
	No. Of Elements	300433 (HE = 53)
	No. Of Materials	2
Cylinder (10.75 in diam)	No. Of Nodes	3279
	No. Of Elements	1599
	No. Of Materials	1

Table 7.2. FEM summary of free field model.

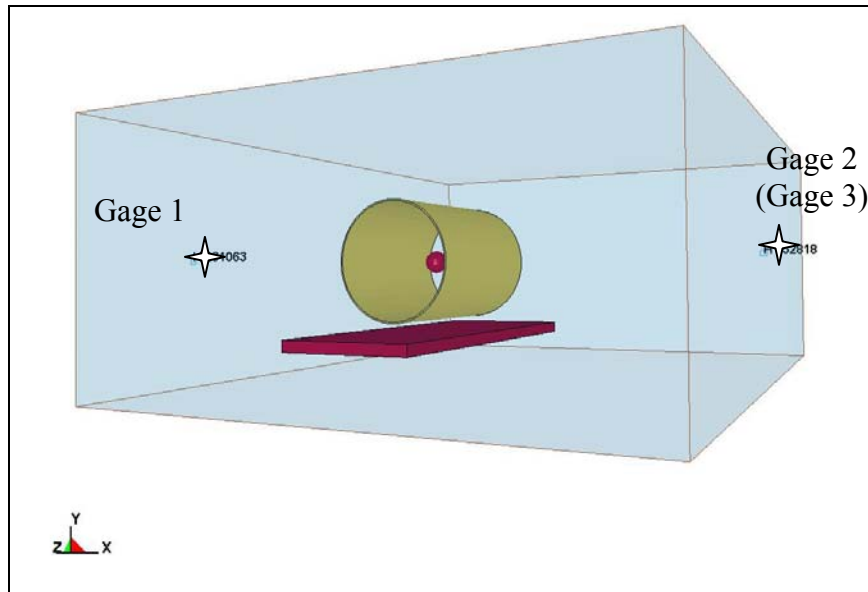


Figure 7.1. Free field model, gages located 30 in from charge center.

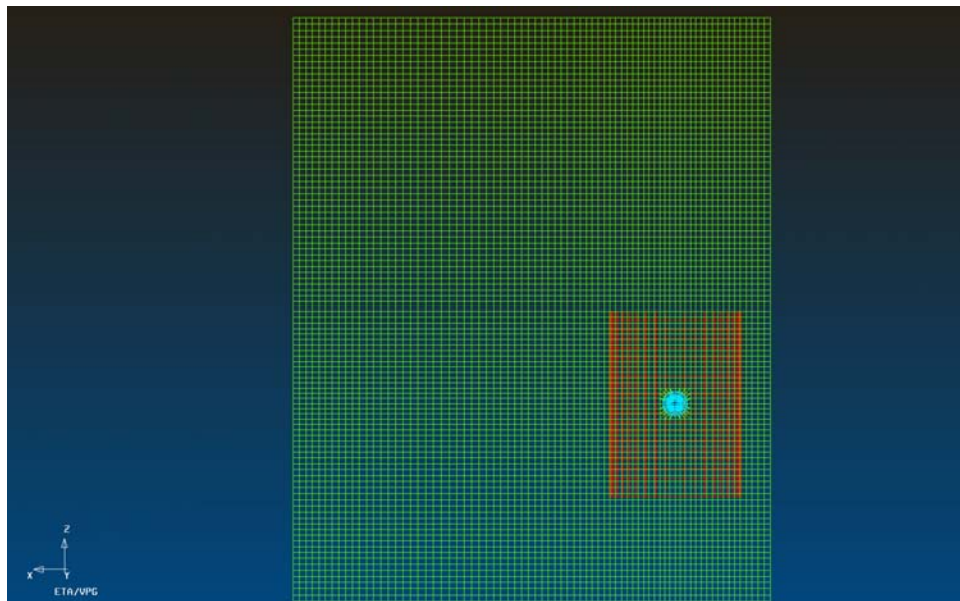


Figure 7.2. Free field model mesh view, test stand FEM hidden.

7.2 Numerical Results

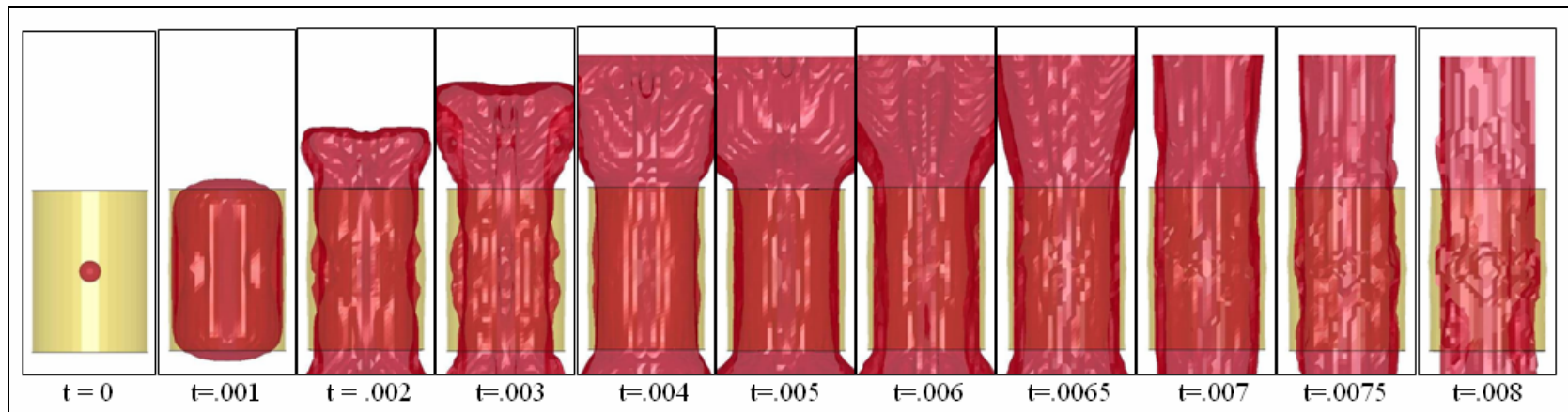


Figure 7.3. FE model animation of dominate fluid for 10.75 in diameter cylinder.

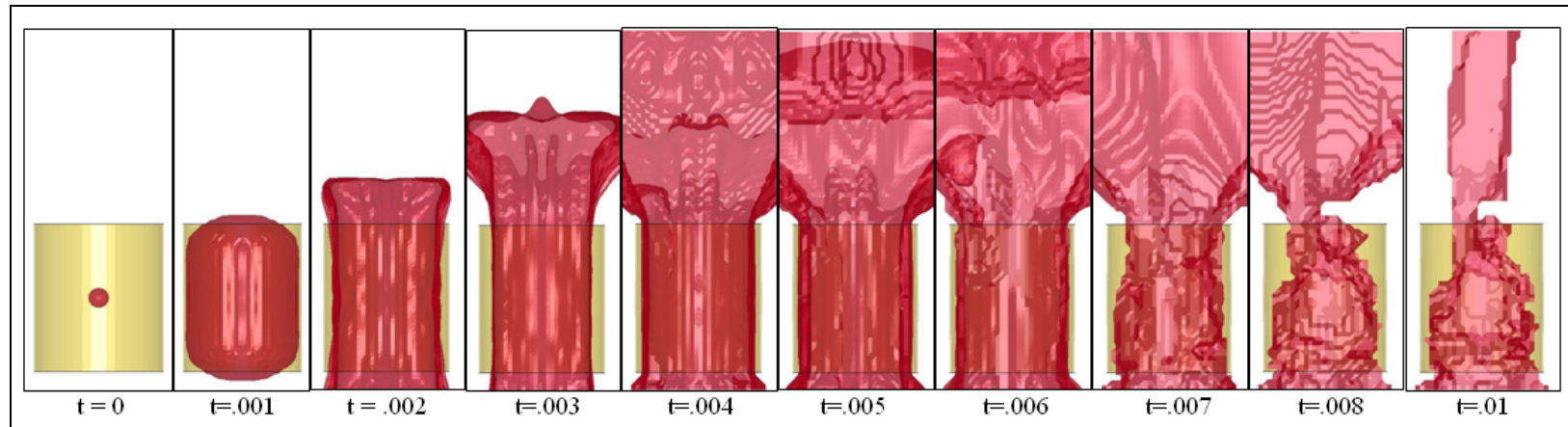


Figure 7.4. FE model animation of dominate fluid for 12.75 in diameter cylinder.

Snapshots of the high explosive event are shown in Figure 7.4 for 8 msec 10.75 in diameter model and in Figure 7.5 for 10 msec 12.75 in diameter model. The HE quickly escapes from the low profile, 15 in high cylinders. The 12.75 in diameter cylinder experiences what appears to be the early onset of volatile flow, most apparent at 5 msec. However, turbulent flow is a complex topic and this model does not account for the turbidity of air and HE. Even so, LS DYNA's numerical approximation of dominate fluid shows a shift in the behavior. This shift corresponds to the cylinder mid-line deformation rebounding outwards, see chart in Figure 7.5. This physical movement of the compartment wall may contribute to the chaotic nature of the rebounding shock waves. Unlike the 10.75 in diameter cylinder, the 12.75 in diameter cylinder experiences a period of concave deformation, where the mid-line elements receded into the center of the cylinder before bulging outwards. This behavior may be attributed to the specific size of the explosive compared to the compartment diameter and height. Referring back to Figures 7.4 and 7.5, the flow of the HE out of the compartment is more direct and linear for the larger diameter cylinder when compared with the 10.75 in diameter cylinder. This rapid flow of HE and air out of the compartment could create negative pressures that would suck the cylinder walls inward.

The compartment walls did not rupture for either cylinder. From Figure 7.5 it is apparent that the cylinder deformation at the termination of the numerical analysis is not the final plastic deformation of the cylinder. The following plot shows mid-line elements of the cylindrical mitigation compartments continuing to displace outwards.

The deformation plot should plateau to signify the final plastic deformation of the cylinder and equilibrium state.

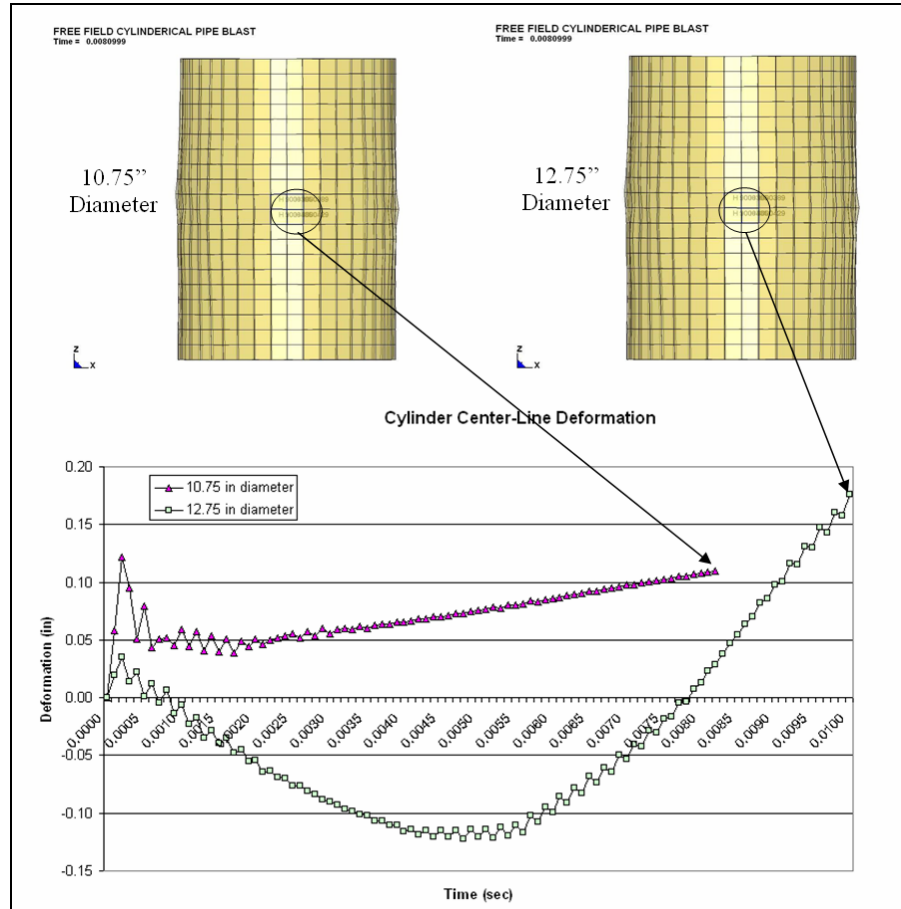


Figure 7.5. FE model center-line deformation plot for cylinders.

The time of arrival of the shock wave front and the magnitude of the incident pressure experienced at the open end of the compartment (Gage #1 location) versus through the side-wall (Gage #2/#3 location) shows the thickness of the cylinder wall is sufficient to redirect the shock waves through the open ends of the compartment, see Figure 7.6, without structural failure. The incident pressure experienced at 30 in stand-off without mitigation was calculated by running the numerical analysis after removing the cylinder from the simulation. The reduction in magnitude of the

incident pressure at the Gage #2 location was affected by the deliberate channeling of the shock wave through the compartment's open ends, reducing the effects by 350%. This channeling effect, however, doubled the overpressures witnessed at the Gage #1 location.

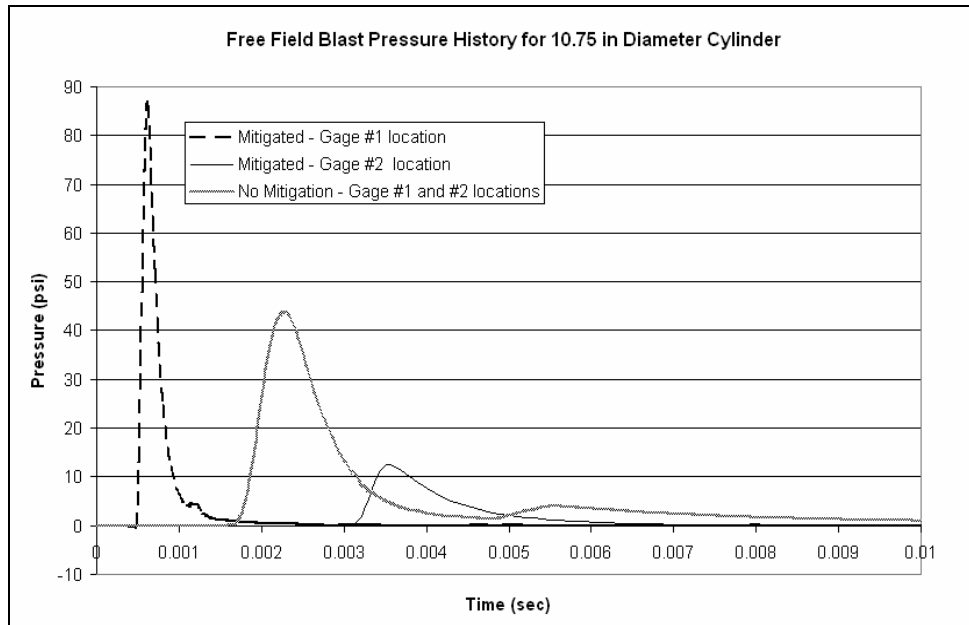


Figure 7.6. Pressure history for 10.75 in diameter cylinder.

The capacity for energy absorption is examined with kinetic energy plots for each cylinder. Figure 7.7 shows the kinetic energy history normalized by the mass of the mitigation compartment. The 10.75 in diameter cylinder reaches a much higher energy state and very quick returns to a lower energy state and eventually equilibrium. The 12.75 in diameter cylinder reaches approximately a third of the potential energy of the 10.75 in diameter cylinder. This larger diameter cylinder does not completely return to its state of equilibrium when the simulation ends at 10 msec. The lighter weight 10.75 in diameter cylinder, from review of the potential energy plots alone, appears to have more energy absorbing capability for this size explosive

and compartment height in the free field blast environment. This narrower size cylinder encloses the HE more closely, prohibiting a greater percentage of the shock wave front from escaping prior to interacting with the cylinder wall. Referring back to Table 7.1, the wall thickness of the 10.75 in diameter cylinder is slightly thinner, 0.134 in, compared to the 12.75 in diameter cylinder, 0.165 in. This small difference in wall thickness is not sufficient enough to affect the results when compared to the cylinder diameter effects for this particular blast scenario.

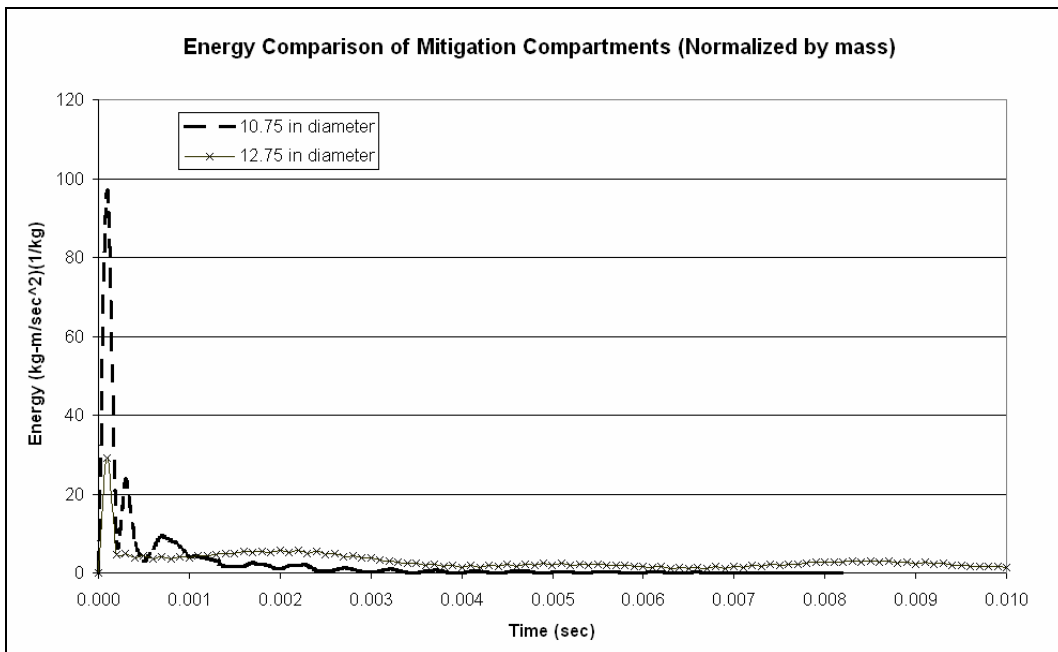


Figure 7.7. Kinetic energy plot for cylinders.

7.3 Experimental Approach

Field testing of schedule 5s mild steel cylinders was conducted for both the 10.75 in and 12.75 in diameter cylinders. The cylinders were 15 in tall. Unfortunately, only the 10.75 in diameter cylinder pressure data was successfully retrieved from the scopes.

Cylinders were positioned horizontally on a heavy 1 ft x 3 ft metal stand cushioned by a 1 in thick foam pad. Chains secured the cylinder to prevent roll off. Three side-on pressure gages were positioned 30 in from the center of the explosive charge, see Figure 7.8. As a precaution fragmentation poles were positioned 12.75 in from the cylinder wall between the cylinder and side-on pressure gages. The explosive charge was spherical in shape and included a small booster encased in an acrylic shell. The explosive charge was positioned in the center of the mitigation cylinder using foam supports, see Figure 7.9.



Figure 7.8. Field test set-up of 12.75 in diameter cylinder.



Figure 7.9. Explosive positioned on foam support.

While the pressure gage data was lost from the 12.75 in diameter test, the final deformation of the cylinder was recorded, see Figure 7.10. The 10.75 in diameter cylinder experienced a similar deformation pattern, see Figure 7.11. Figure 7.12 shows the pressure history for the three gages. These values are discussed in detail in the next section.



Figure 7.10. Post experiment center-line deformation of 12.75 in cylinder

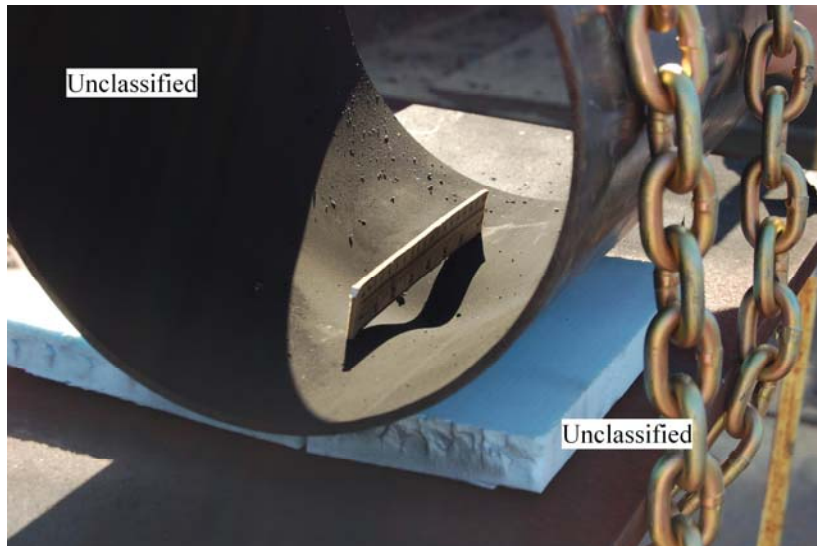


Figure 7.11. Post experiment center-line deformation of 10.75 in cylinder

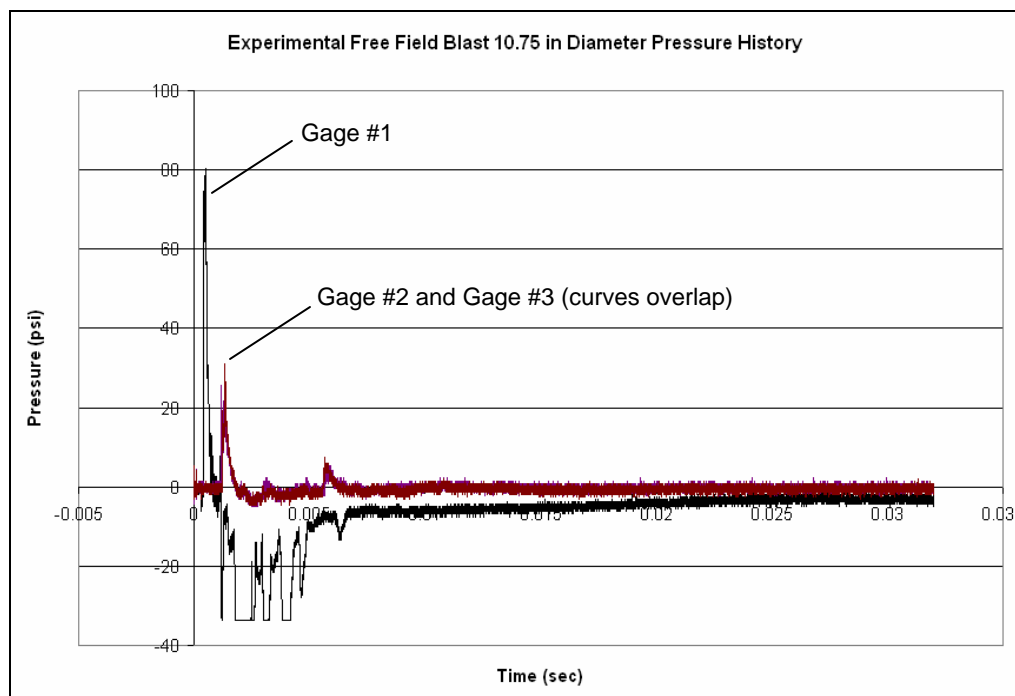


Figure 7.12. Pressure history for 10.75 in diameter free field experiment.

7.4 Comparison of Numerical Analysis and Experimental Data

The incident pressure measured at the open end of the cylinder, Gage 1 location, corresponds both in magnitude and duration between the numerical analysis and experimental data. See Figure 7.13. The time of arrival of the shock front for

Gage 1 is also nearly identical between the simulation and field test. The negative pressure values recorded in the experimental test are most likely due to the movement of gage stand after the initial loading.

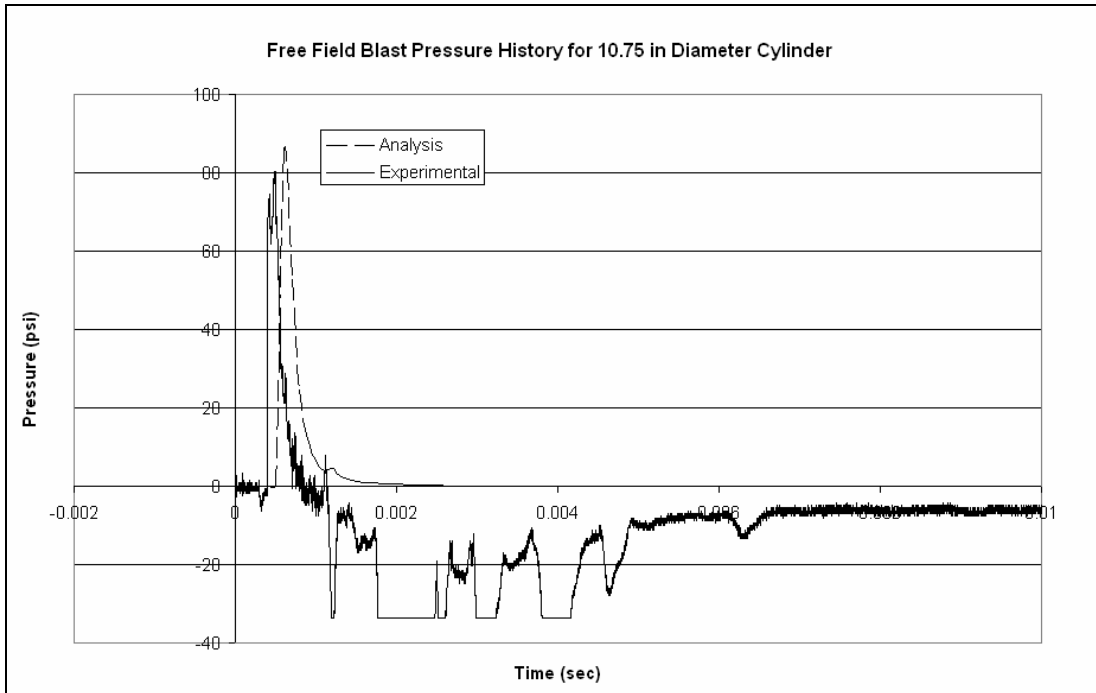


Figure 7.13. Pressure history comparison, Gage 1.

The side pressure measurements do not correlate as shown in Figure 7.14 and 7.15. This may be attributed to the complex nature of reflected pressures. The metal stand on which the compartment was secured, see Figure 7.8, extends beyond the length of the cylinder. This protruding metal structure provided an additional surface for the incident pressure to reflect. The potential for complex blast behavior is increased; with faster, higher magnitude reflected shock waves shown in the experimental pressure history plots, see Figures 7.14 and 7.15. Both side-on Gage #2 and Gage #3 experience a subsequent lower magnitude peak in the overpressure. The recording of identical subsequent peaks in overpressure between the side-on gages is

demonstrative of the secondary pressure waves in the laboratory environment due to the attenuation of the reflected shock wave front. The difference in magnitude of the overpressures recorded in the laboratory environment may equally be attributed to the position of the side-on gages on the pencil mounts, see Figure 7.8. If the side-on gages were slightly misaligned, the pressure readings would record magnified overpressures and not the incident overpressures, as calculated in the numerical analysis. Reflected overpressures can be 1 to 4.3 times greater in magnitude than the incident pressure depending on the angle of incidence. Additionally, if these pencil mount stands were positioned closer to the open ends of the compartment, even slightly, the time of arrival and magnitudes would be effected. Post-test, all pencil gage stands had moved from their original positions 1-2 inches. This movement is an additional contributor to the subsequent peaks shown in Figures 7.14 and 7.15.

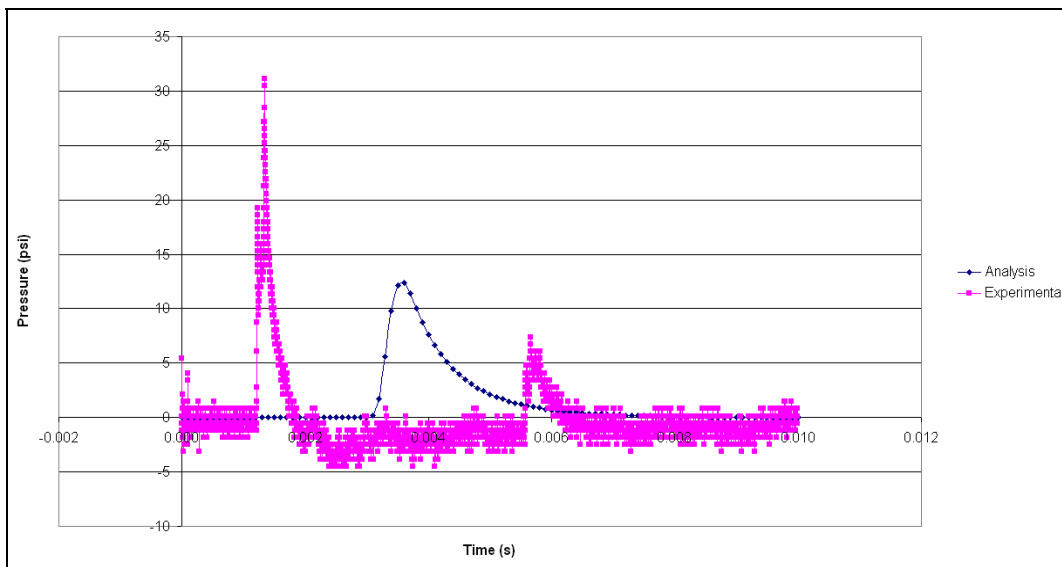


Figure 7.14. Pressure history comparison, Gage 3.

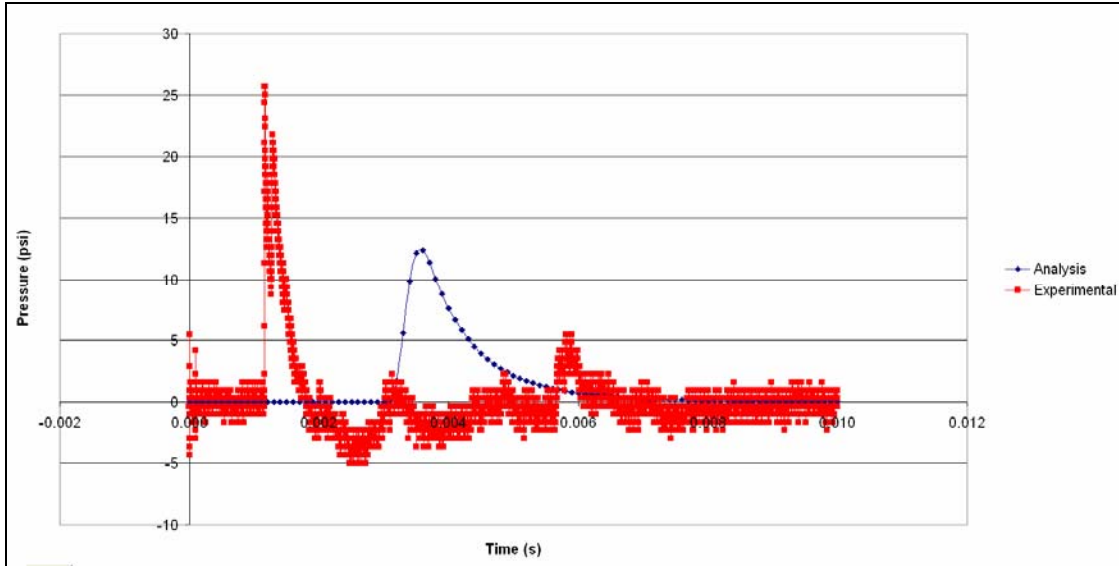


Figure 7.15. Pressure history comparison, Gage 2.

The deformation pattern of both the 10.75 in and 12.75 in diameter cylinders is similar to the numerical analysis. However, the numerical analysis runtime, 335 hrs, was not sufficient for the final deformation to be achieved for direct comparison. However, Table 7.3 shows the deformation trend between the FEA and experimental data to be within an acceptable margin for both cylinders.

	Numerical Analysis	Experimental Results
12.75 in diameter	0.17 in @ 0.01 sec	0.20 in
10.75 in diameter	0.11 in @ 0.008 sec	0.15 in

Table 7.3. Comparison of cylinder mid-line deformation.

7.5 Conclusion

The numerical analysis shows the lighter weight, thinner walled, 10.75 in diameter cylinder maintains its structural integrity while exhibiting greater energy absorbing capabilities when compared to the 12.75 in diameter cylinder. The channeling effect of the mitigation compartment has the potential to double the overpressures vented from the open ends of the cylinder for this particular sized HE

and compartment design. Thus, it is critical to use extreme caution when positioning the mitigation compartment openings or vent devices.

Only the 10.75 in diameter pressure data was successfully retrieved from the scopes. Therefore, direct comparison of pressures between numerical and field results is limited to this cylinder. The peak overpressure profiles show traditional shock wave behavior in both the numerical analysis and laboratory gage results. The unobstructed open end of the mitigation compartment provides excellent correlation in overpressures. Due to complex behavior of reflected shock wave fronts, the overpressures positioned normal to the cylinder walls, do not align as predicted in the numerical analysis.

The 10.75 in diameter cylinder appears sufficient for further testing in the confined environment without risk of fragmentation. Therefore this cylinder was selected for additional testing with its advantages of lighter weight per linear foot and more compact shape.

Chapter 8: Confined Blast of Cylindrical Compartment

From Chapter 7's numerical analysis and laboratory testing, the 10.75 in diameter cylinder was chosen for confined blast investigation and field testing. This schedule 5s mild steel cylinder demonstrated adequate free field blast performance, and is relatively lightweight and compact in shape, see Table 8.1.

Two different height cylinders, 15 in and 30 in were chosen for confined blast testing. The vehicle hull was simplified to a rectangular shape, with the dimensions 6 ft x 5 ft x 4.5 ft and constructed of two inch thick RHA walls. To simulate the mass of two human occupants, two 150 lb 29 in x 18 in x 1 in steel plates were positioned 18 in from chamber center, centered in their respective planes.

Outside diameter	Inside diameter	Thickness	Weight (lb/ft)
10.750 in	10.482 in	0.134 in	15.19

Table 8.1. Cylinder properties for confined field test.

The goals of this study were to evaluate the protective effectiveness of the selected mitigation compartments, gain greater insight into the behavior of dually confined blast within an occupied confined space and compare confined blast laboratory testing with a FEA.

8.1 Experimental Field Test Set-up

The rectangular RHA chamber rested on top of steel I-beams within the test pad. The door of the chamber was hinged with bolt locks. Mitigation cylinders centered within the chamber and suspended by steel cables, see Figure 8.1. One 150 lb steel plate was mounted to the rear chamber wall with four 1.5 in diameter steel

rods. This welded plate had a 4 in diameter access hole to allow for flush mounting a reflective pressure gage; the chamber wall behind this welded plate also had a 4 in diameter hole to accommodate the gage wires and stand. The second 150 lb steel plate was welded to a 5 ft long rod and rotated freely when hung on well lubricated saddles, see Figure 8.2. Two 4 in diameter holes were cut in the centers of the remaining two side chamber walls. One reflective pressure gage was flush mounted through one hole and the other hole accommodated a side-on pencil pressure gage, see Figure 8.3. The side-on pressure gage was positioned 18 in from the center of the explosive charge. A 3 in diameter hole was cut in the top center of the chamber, allowing the explosive charge to be lowered into the center of the chamber and mitigation cylinder, see Figure 8.4. The explosive charge was spherical in shape and included a small booster encased in an acrylic shell. Once the chamber was instrumented and secured the spherical shaped explosive was carefully suspended by wire into the confined space.

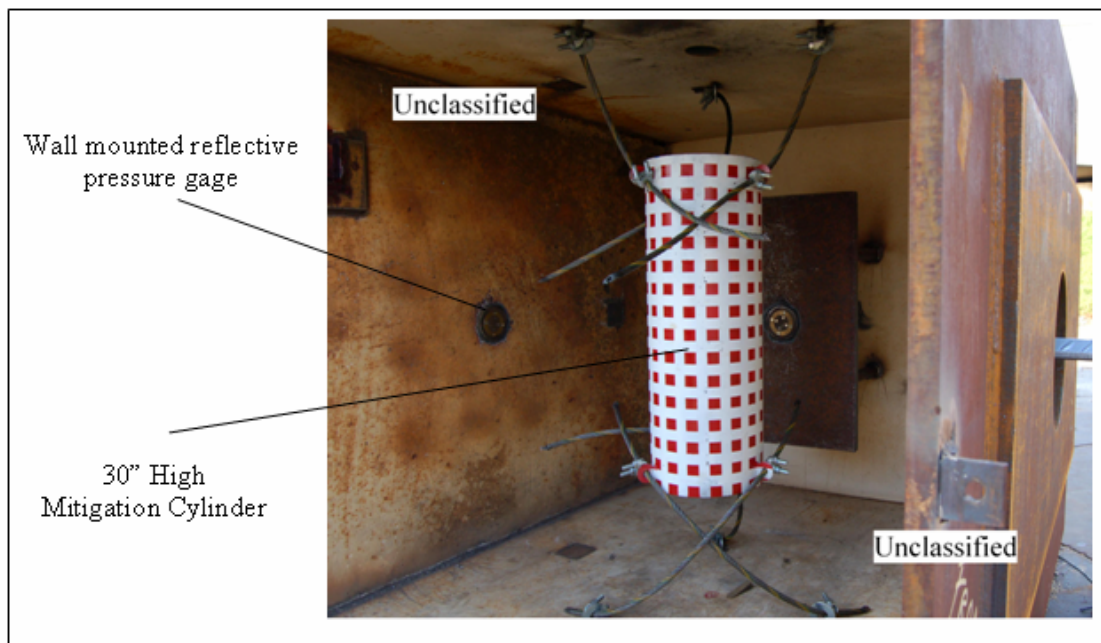


Figure 8.1. Chamber interior, 30 in tall cylinder; rotating plate removed.

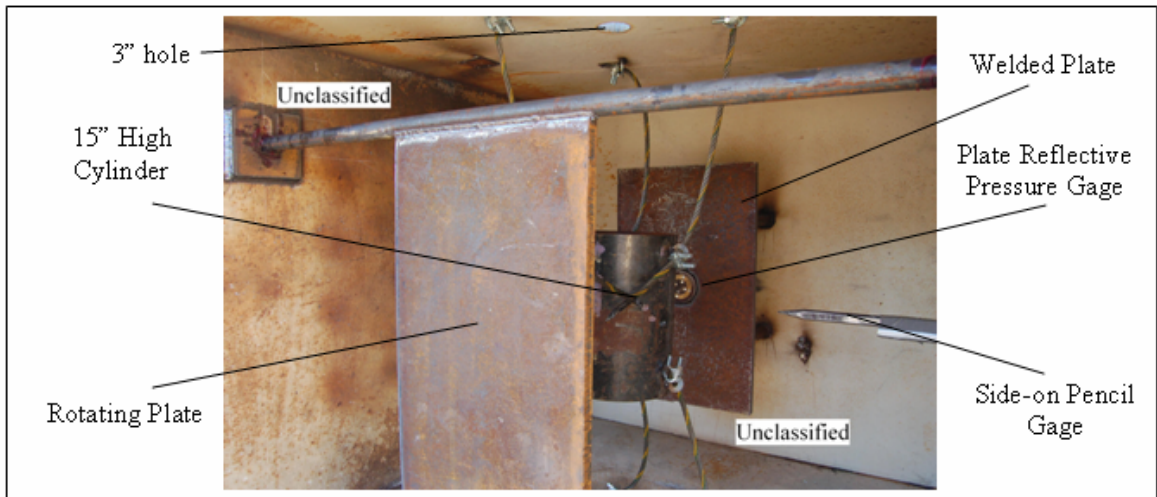


Figure 8.2. Chamber interior, 15 in tall cylinder.

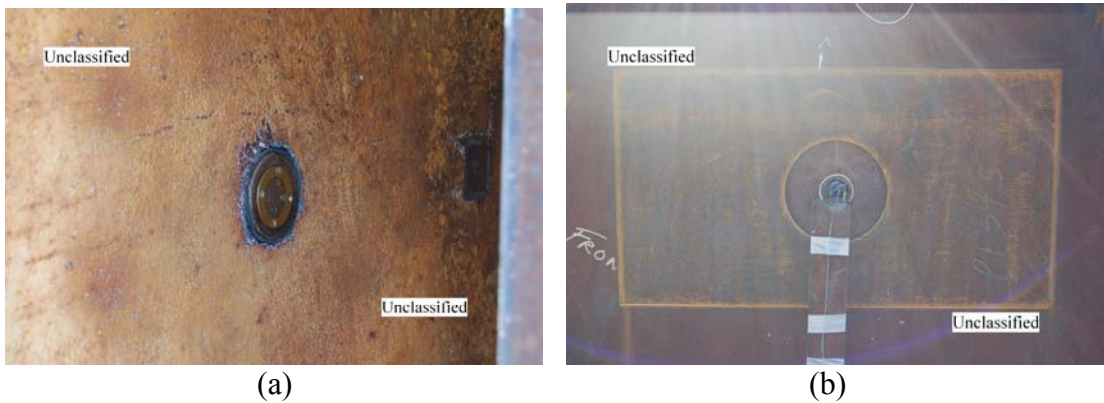


Figure 8.3. Gages (a) Wall flush mounted (b) Pencil gage exterior view



Figure 8.4. Access holes (a) Wall flush mounted, exterior view (b) HE access hole.

8.2 Experimental Field Test Results

Test #1 was conducted with the 15 in tall cylinder. Figure 8.5 shows the post-test shot of the chamber with the sheared door bolts and the chamber door, which was thrown 25 ft. The large movement of the chamber and the loss of the door prevented the pressure gages from collecting the confined blast history past the first few milliseconds of the blast event. Figures 8.6 and 8.7 show the degree to which the chamber moved compared to the original pressure gage stand locations. The wall flush mounted pressure gage was removed entirely from the chamber, see Figure 8.8.



Figure 8.5. Confined blast post-test #1 view of chamber and chamber door.

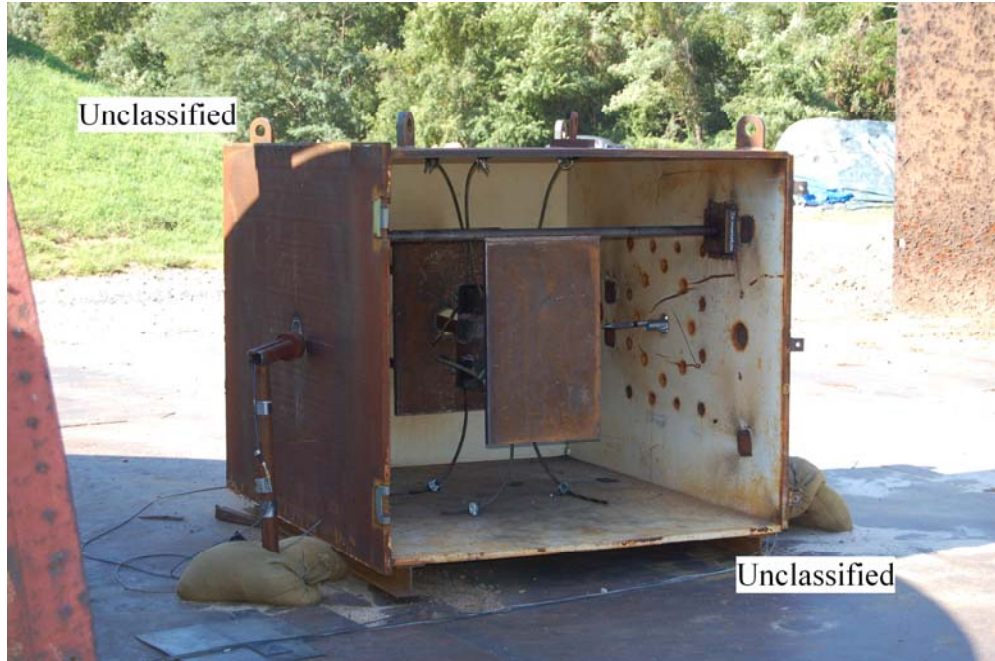


Figure 8.6. Confined blast post-test #1 view of interior.



Figure 8.7. Confined blast post-test #1 exterior view of gage stands.

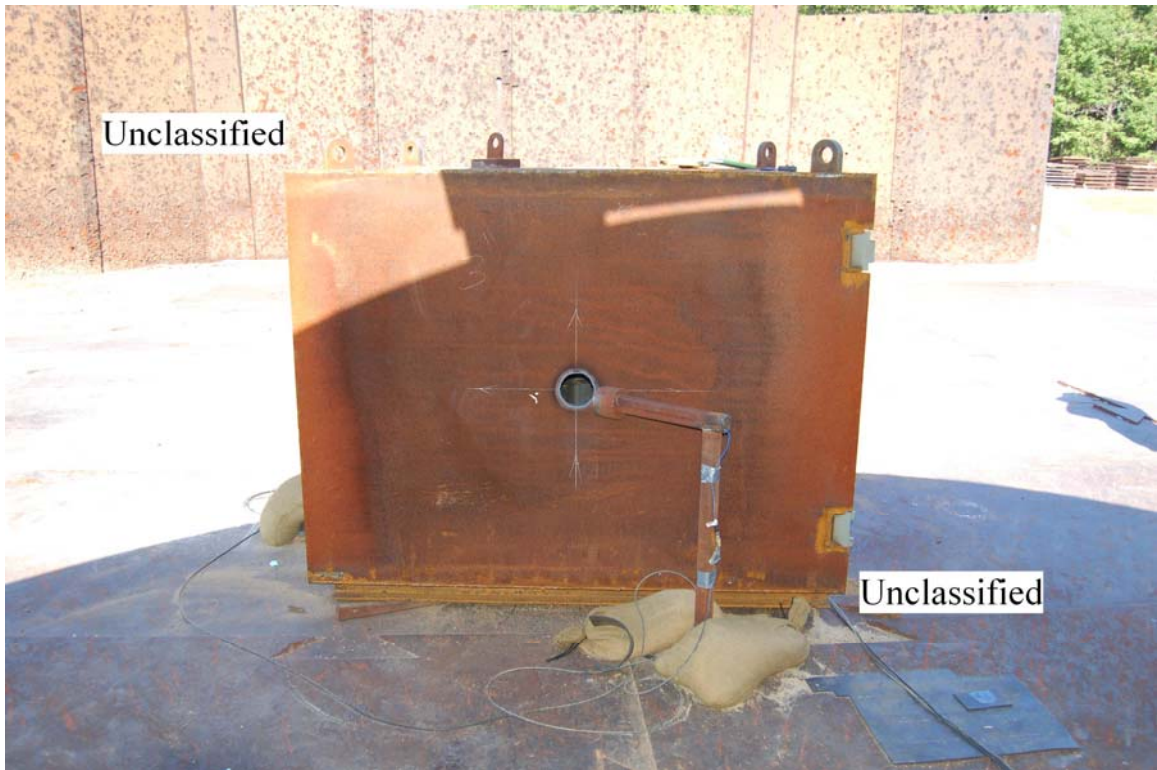


Figure 8.8. Confined blast post-test #1, wall flush mounted gage stand.

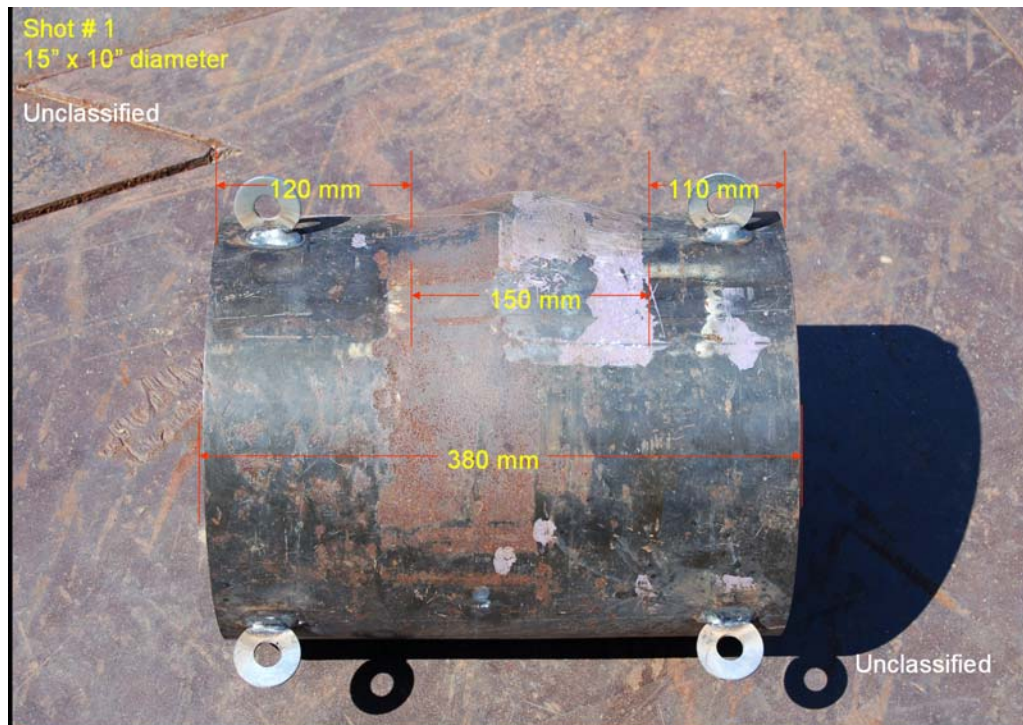


Figure 8.9. Confined blast post-test #1, view A of 15 in high cylinder deformation.



Figure 8.10. Confined blast post-test #1, view B of 15 in high cylinder deformation.

Without rupturing, the final cylinder deformation was a uniform bulge around the midline, see Figures 8.9 and 8.10. The peak overpressures were reached within the first 10 msec, see Figure 8.11. Recall the chamber door was located behind the large rotating plate; the plate appears to have been a sufficient structural obstacle to maintain the confined environment for the first few milliseconds. Figures 8.12-14, were truncated to better view the overpressure data occurring within the first 10 msec.

The shock front time of arrival for the plate is approximately 0.5 msec earlier than that of the side-on gage or chamber wall; recall the plate and side-on gages were equidistant from the charge and ground. From Figure 8.12, the initial peak incident overpressure measured by the side-on gage is approximately 22 psi, reaching its largest magnitude of 80 psi at 4 msec. From Figure 8.13, the initial peak reflected overpressure measured by the plate flush mounted gage is approximately 55 psi,

reaching its largest magnitude of 60 psi at 4 msec. The plate overpressures are expectedly larger in magnitude compared to the side-on pressures since reflective overpressures can be as much as 4 times the incident pressure depending on the angle of incidence and proximity. From Figure 8.14, the initial peak reflected overpressure measured by the chamber flush mounted gage is approximately 60 psi, reaching its largest magnitude of 120 psi at 3.5 msec. While the wall was an additional 12 inches from the HE, this additional stand-off is not sufficient to reduce the chamber wall overpressures for this size explosive and mitigation compartment design. Additionally, the 150 lb steel plates have the potential to act as additional structural surfaces for the development of complex Mach fronts. Overpressure values recorded after the initial shock front were affected by the displacement of the chamber.

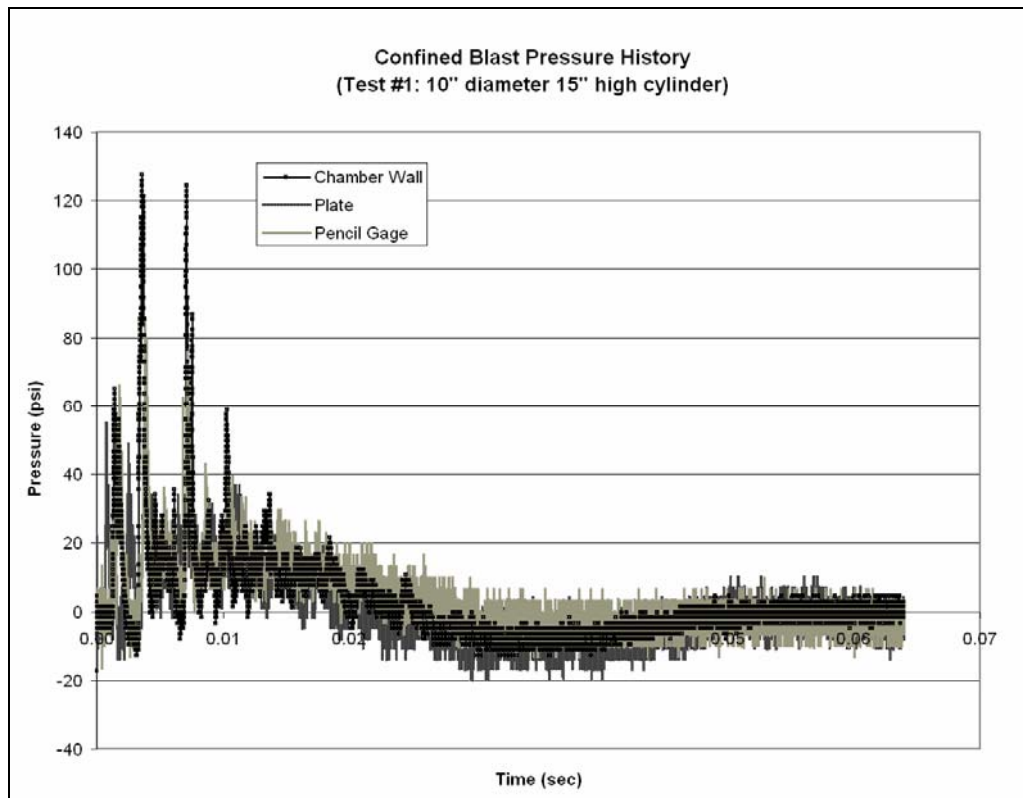


Figure 8.11. Pressure history of test #1

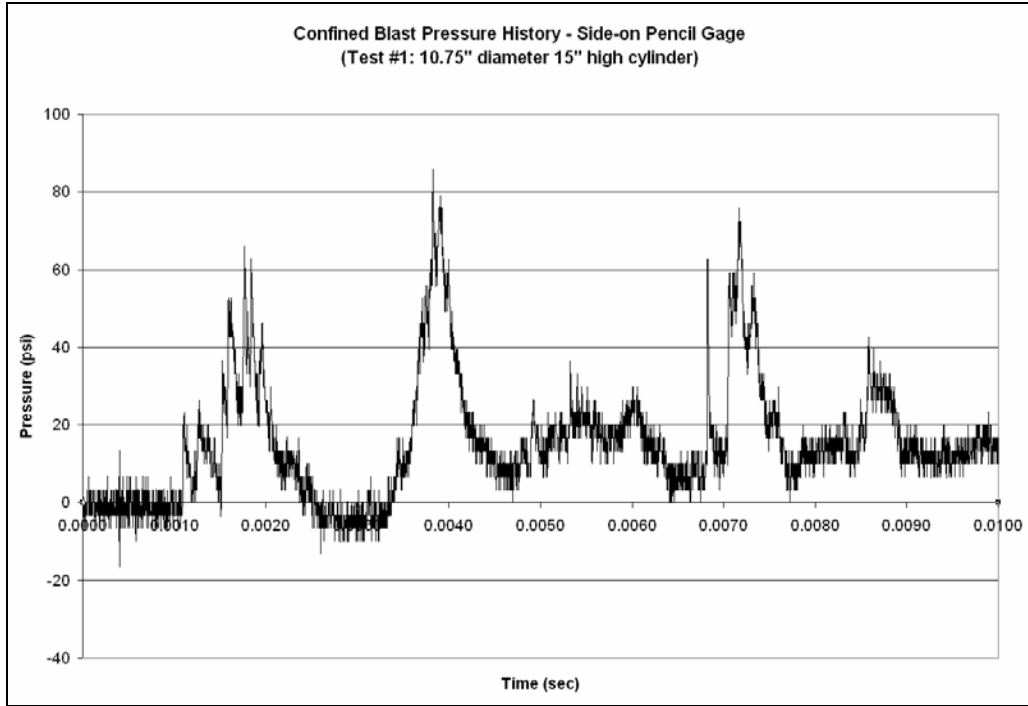


Figure 8.12. Pressure history of test #1, side-on pencil gage.

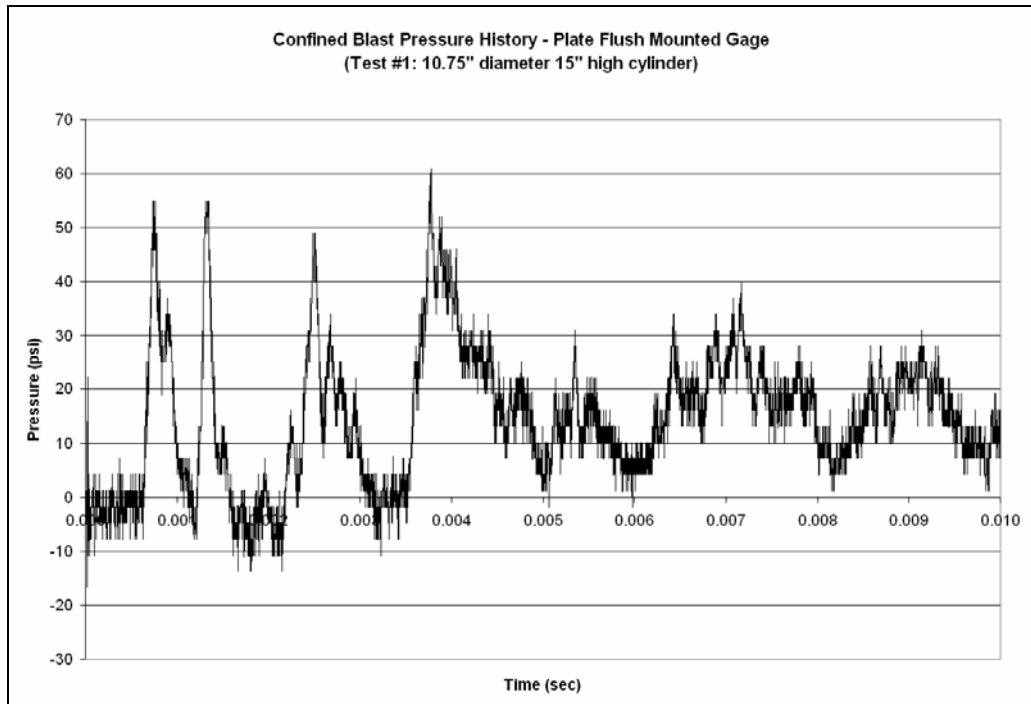


Figure 8.13. Pressure history of test #1, plate flush mounted gage.

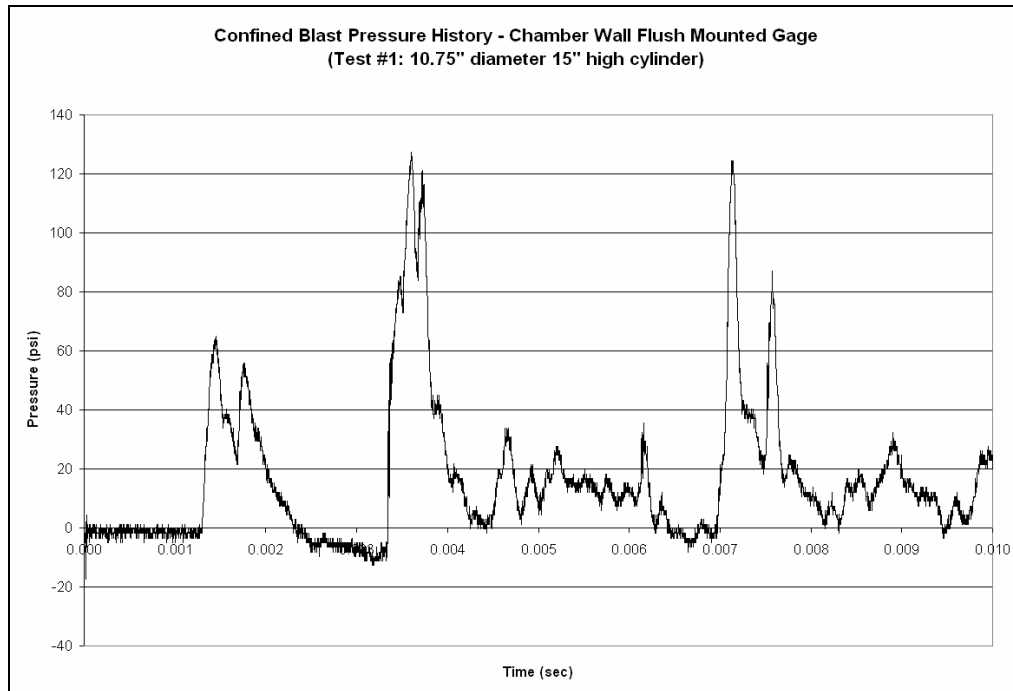


Figure 8.14. Pressure history of test #1, chamber wall flush mounted gage.

Test #2 was conducted with the 30 in high cylinder, with the modification of encircling the chamber with a long chain to keep the door from becoming a projectile and thrusting the chamber. Figures 8.14 and 8.15 show the chains used to secure the chamber door, the door hinge failure and the door permanent deformation. Note the minimal movement of the gages post-test, see Figure 8.17.

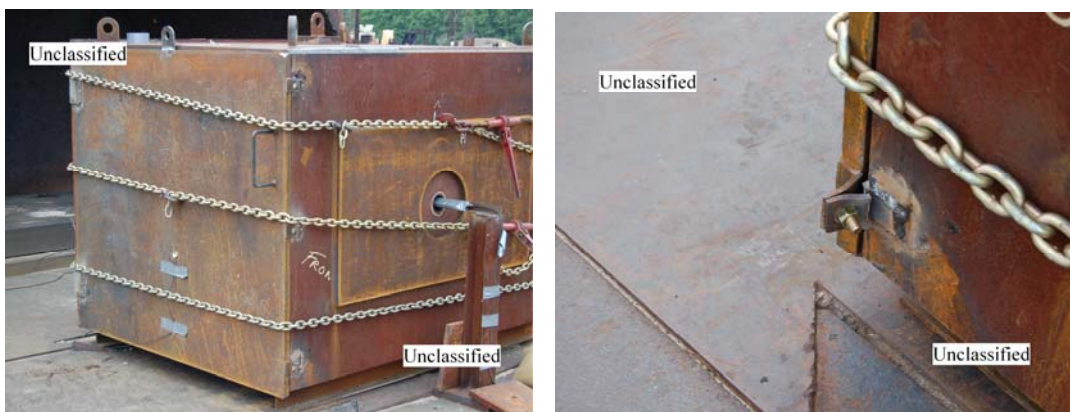


Figure 8.15. Confined blast post-test #2, exterior view and door hinge failure.



Figure 8.16. Confined blast post-test #2 post-test, chamber door deformation.



Figure 8.17. Confined blast post-test #2, pressure gage displacement.

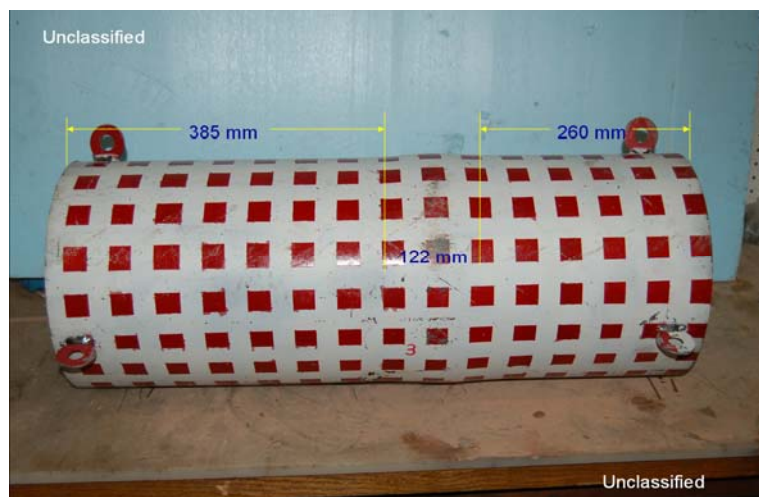


Figure 8.18. Confined blast post-test #2, view A of 30 in high cylinder deformation.

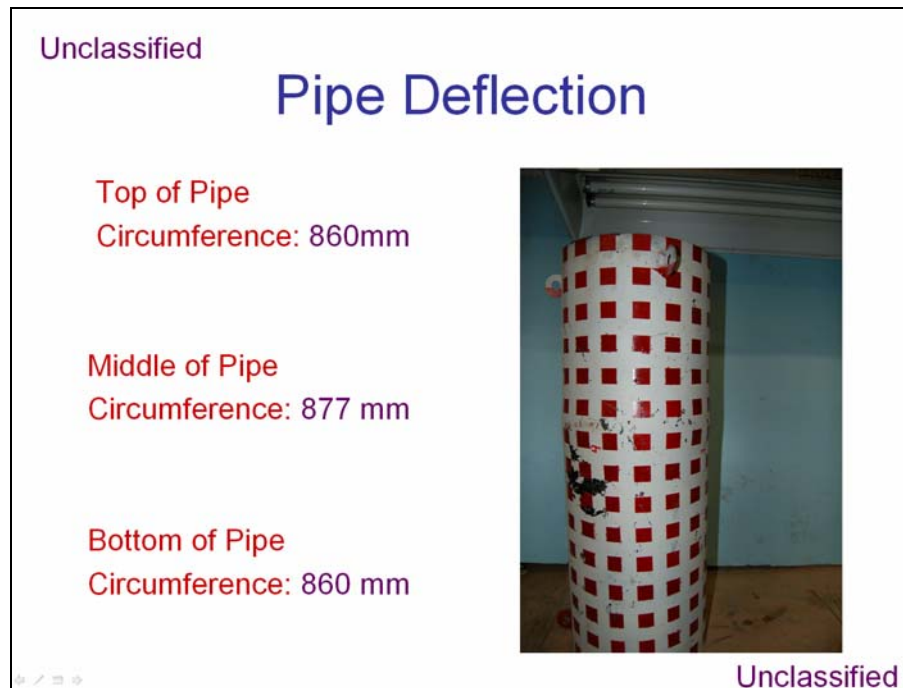


Figure 8.19. Confined blast post-test #2, view B of 30 in high cylinder deformation.

Without rupturing, the final cylinder deformation was a uniform bulge around the midline, see Figures 8.18 and 8.19. The peak overpressures were reached within the first 10 msec, see Figure 8.20. Figures 8.21-23, were truncated to better view the overpressure data occurring within the first 10 msec.

The shock front time of arrival for the plate is approximately 0.2 msec earlier than the side-on gage or chamber wall time of arrival; recall the plate and side-on gages were equidistant from the charge and ground. From Figure 8.21, the initial peak incident overpressure measured by the side-on gage is approximately 95 psi, reaching its largest magnitude of 210 psi at 3.5 msec. From Figure 8.22, the initial peak reflected overpressure measured by the plate flush mounted gage is approximately 35 psi, reaching its largest magnitude of 65 psi at 8 msec. The plate overpressures are unexpectedly smaller, by approximately 1/3 in magnitude, when

compared to the side-on pressures. It is difficult to determine if there is an error in magnitude stemming from the side-on gage or from the plate flush mounted gage. Since this variation is the exact opposite found in Test #1, additional testing is required to draw any conclusions to this unexpected response. From Figure 8.23, the initial peak reflected overpressure measured by the chamber flush mounted gage is approximately 37 psi, reaching its largest magnitude of 90 psi at 3.5 msec. Again, the additional stand-off distance of the chamber wall was not sufficient to reduce the wall overpressures for this size explosive and mitigation compartment design. Overpressure values recorded after the initial shock front were affected by the displacement of the pressure gage stands; therefore, the largest magnitude peak overpressures recorded for each gage included some disturbance error.

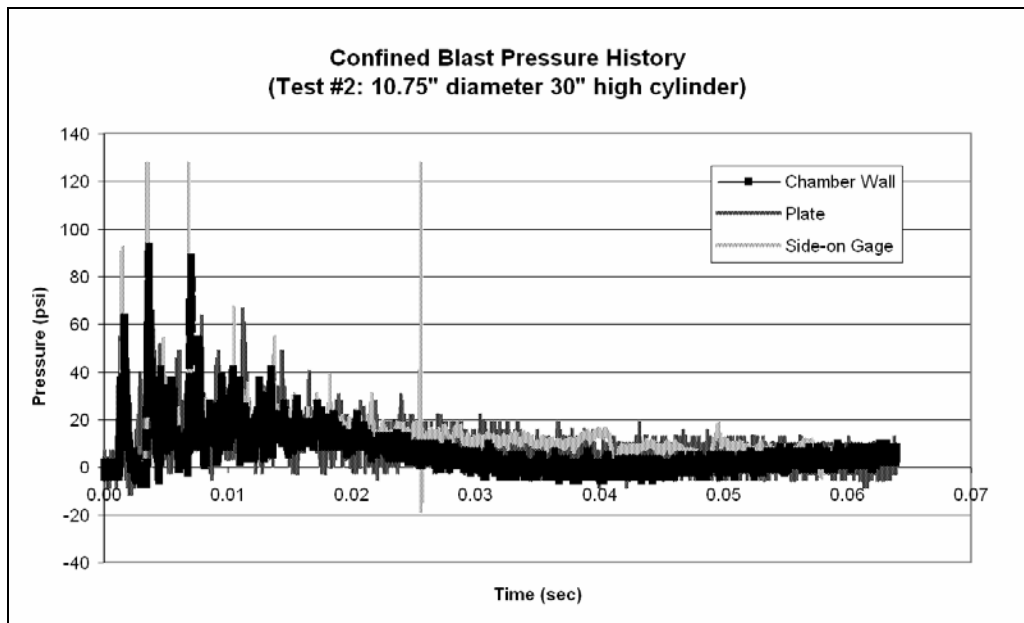


Figure 8.20. Pressure history of test #2.

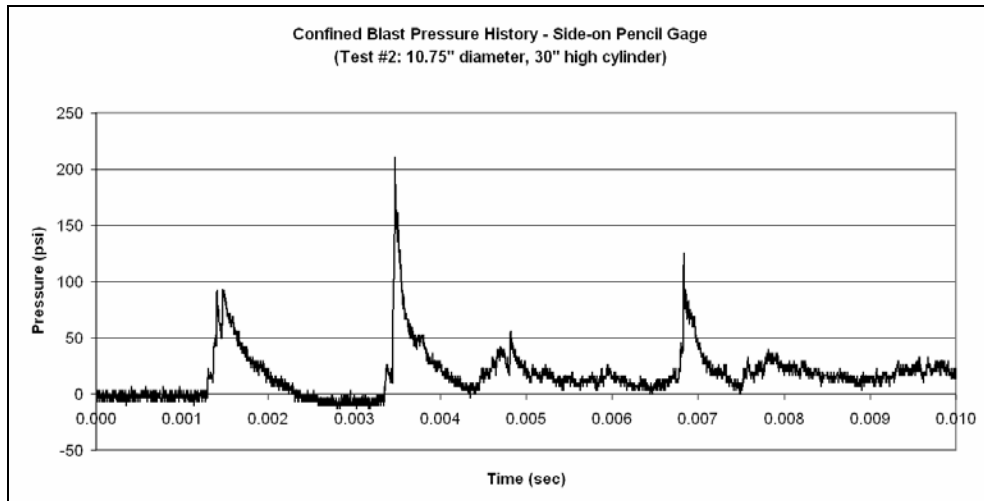


Figure 8.21. Pressure history of test #2, side-on pencil gage.

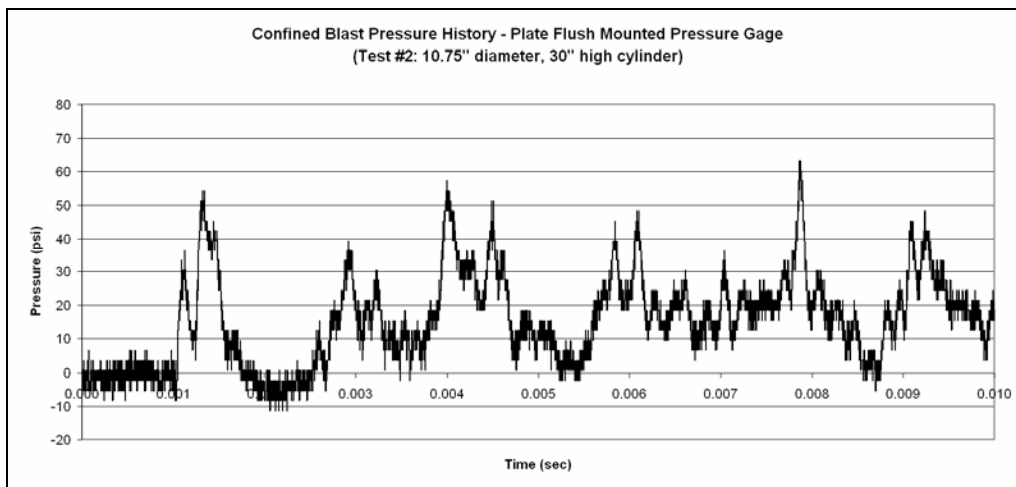


Figure 8.22. Pressure history of test #2, plate flush mounted gage.

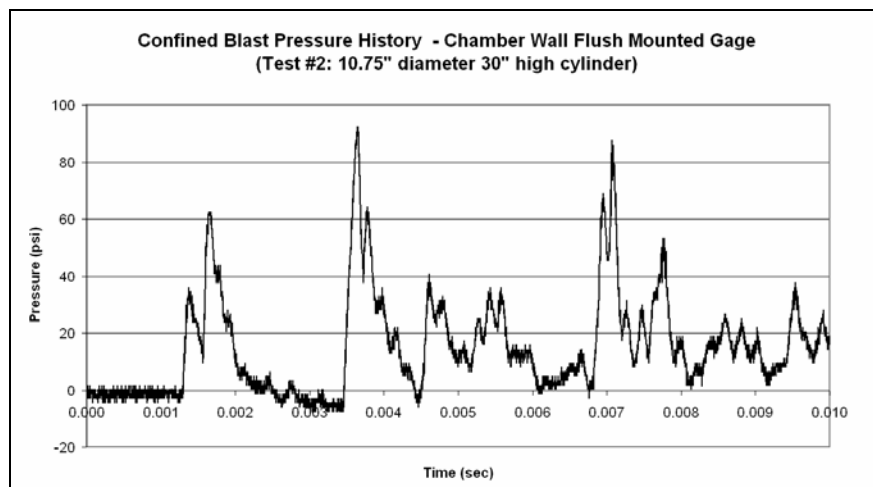


Figure 8.23. Pressure history of test #2, chamber wall flush mounted gage.

8.3 Numerical Analysis Model

The 30 in tall cylinder was selected for correlation FEA based on the successful laboratory performance of this compartment and the minimal movement of the chamber.

The Lagrangian elements (plates, chamber and cylindrical mitigation compartment) and multi-material ALE elements (HE and air) were coupled using LS DYNA's penalty-based algorithm `CONSTRAINED_LAGRANGE_IN_SOLID`. HE was modeled as `*MAT_HIGH_EXPLOSIVE_BURN` with the equation of state (EOS) defined as `EOS_JWL`. Air was modeled as `*MAT_NULL` defined by `EOS_LINEAR_POLYNOMIAL`. Chamber was modeled as `*MAT_PLASTIC_KINEMATIC` with the material properties for RHA. Plates and mitigation compartment were modeled as `*MAT_SIMPLIFIED_JOHNSON_COOK` with the material properties for mild steel. LS DYNA does not account for heat dissipation to reduce the energy momentum of the HE within the confined space.

The leakage attributed to the chamber door deformation is minimal in the first 10 msec; therefore the chamber was idealized and considered to be unvented with airtight boundaries. The mitigation compartment was free standing without supports, eliminating restrictions to movement or deformation. The structural joints of the mitigation compartment and chamber were modeled as continuous material, no weld or bolt failure criteria were used. The two large 150 lb steel plates were modeled with fixed edge boundaries.

Air ALE elements had an average edge length of 20 mm. The HE was spherical in shape; the ALE elements had a max edge element length of 10 mm. The

compartment and plate solid elements had edge lengths of 20 mm. Mesh densities are summarized in Table 8.2. The chamber walls were modeled as shell elements of two inch thickness with the overall interior dimensions of 6 ft x 5 ft x 4.5 ft. The ALE mesh extended from the center of the charge to at least 100 mm surrounding the chamber, see Figure 8.24.

A one-eighth symmetric model was run in LS DYNA, see Figure 8.25. A dual CPU considerably reduced the computational total run time (335 hours). The simulations were terminated after 10 msec, as the initial overpressure response within the chamber was adequately demonstrated after this time interval. Figure 8.26 shows the overpressure results for the three corresponding laboratory gage locations. These FEA results are discussed in detail in the Section 8.4.

ALE	No. Of Nodes	95273
	No. Of Elements	88254 (HE = 54)
	No. Of Materials	2
	HEXAGONS	88254
Chamber	No. Of Nodes	8105
	No. Of Elements	7949
	No. Of Materials	1
	QUAD. ELEMENTS	7949
Cylinder	No. Of Nodes	329
	No. Of Elements	139
	No. Of Materials	1
	QUAD. ELEMENTS	139
Plate	No. Of Nodes	1140
	No. Of Elements	522
	No. Of Materials	1
	QUAD. ELEMENTS	522

Table 8.2. FEM snapshot of the confined plate study, 1/8th symmetry.

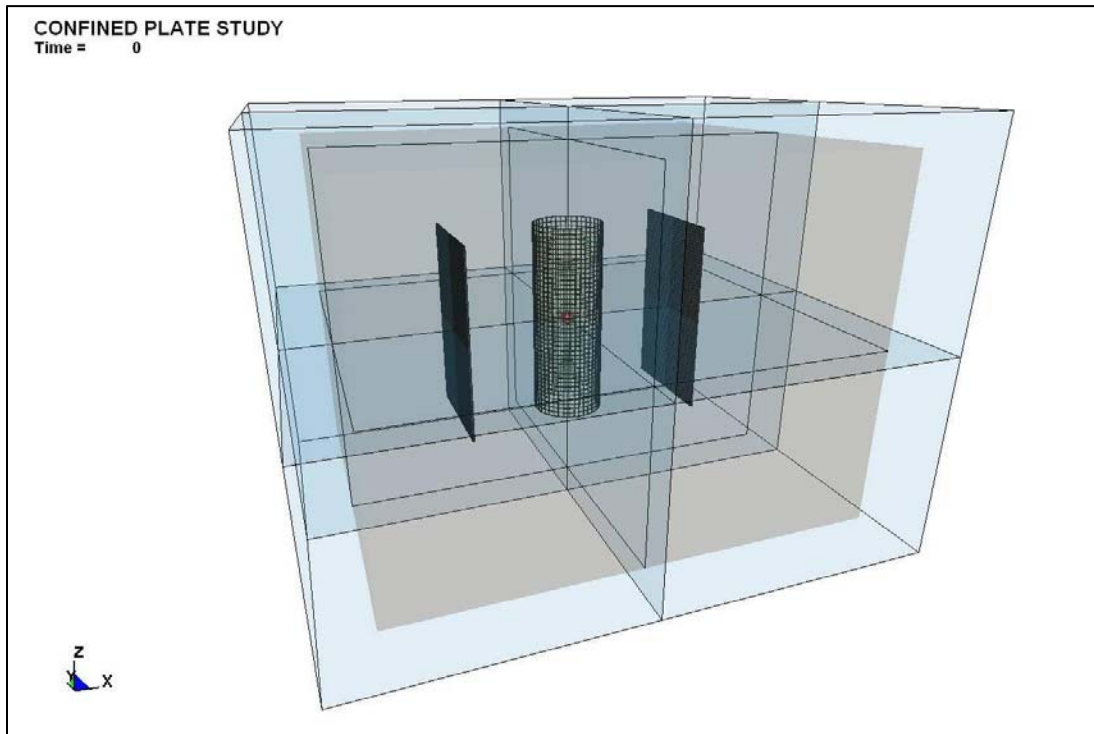


Figure 8.24. Confined blast full model, reflected about symmetric planes.

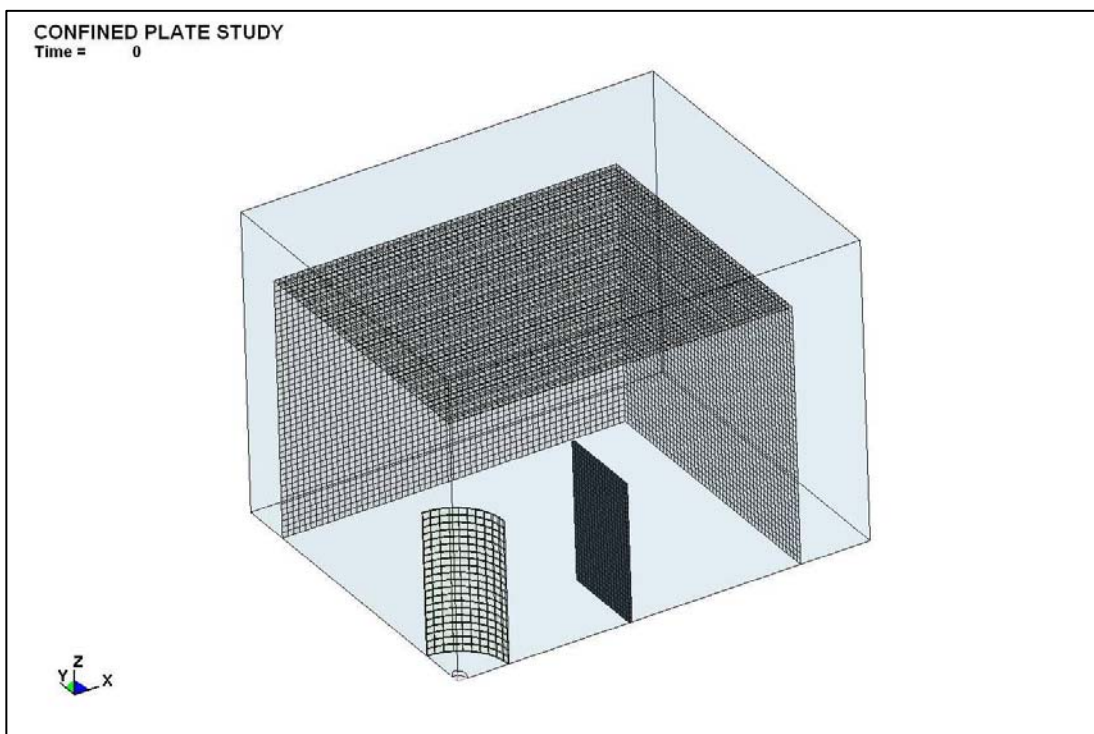


Figure 8.25. Confined blast 1/8th symmetry.

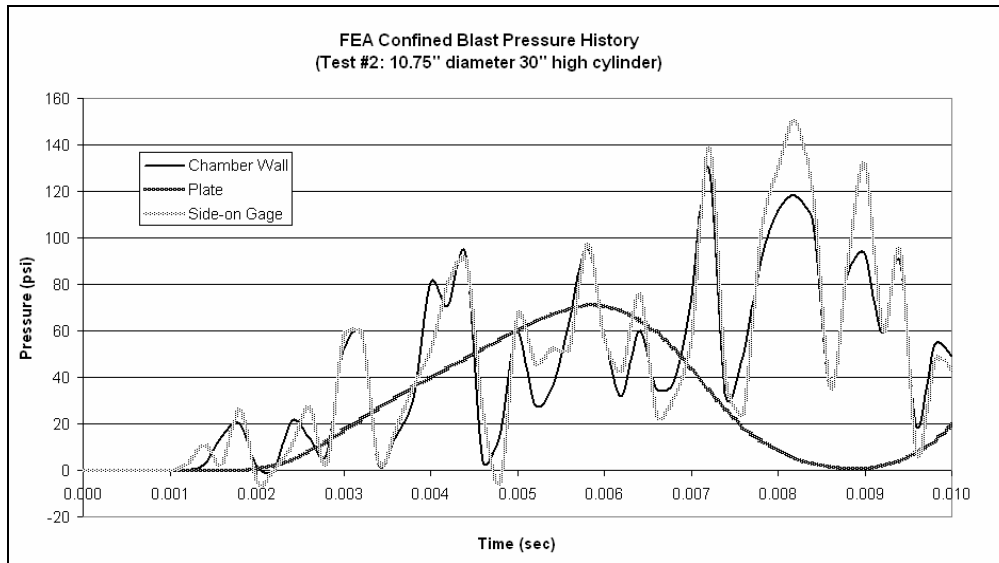


Figure 8.26. FEA confined blast pressure history.

8.4 Comparison of Results

The time of arrival for the shock wave front corresponds nicely between the numerical analysis and the experimental data for the chamber wall and side-on pressure gages, see Figures 8.27 and 8.28. The initial peak overpressure calculated in the FEA is a third of the measured experimental overpressure. Peak overpressures align more closely around 4 msec, but then deviate slightly in magnitude and duration. The overpressure profiles for the side-on pressure gages and plate mid-point experience higher deviations from one another. The lower FEA overpressures calculated for the side-on gage may be attributed to the limitations within the model of describing the complex, turbulent shock wave front occurring with the confined space at a point in the space of the air mesh. The subsequent overpressure peaks from the experimental side-on gages on the pencil mounts may have been affected by the movement of the gage stand. Misaligned gages would record magnified overpressures and not the incident overpressures, as calculated in the numerical

analysis. Both the chamber wall and side-on FEA overpressure plots have a pattern of longer duration and/or increased magnitude over the duration of the event. The FEA does not take into account the heat dissipation effects, additionally since the FEM was 1/8th symmetric, the rotating plate was considered fixed and thus created an additional structural surface for the entire FEA blast event.

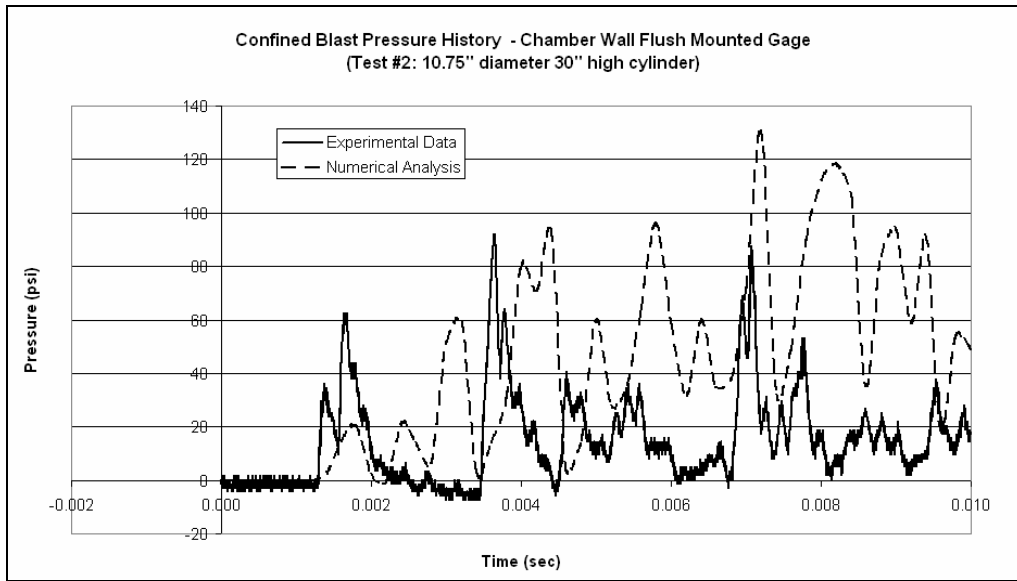


Figure 8.27. Pressure history comparison, chamber wall center.

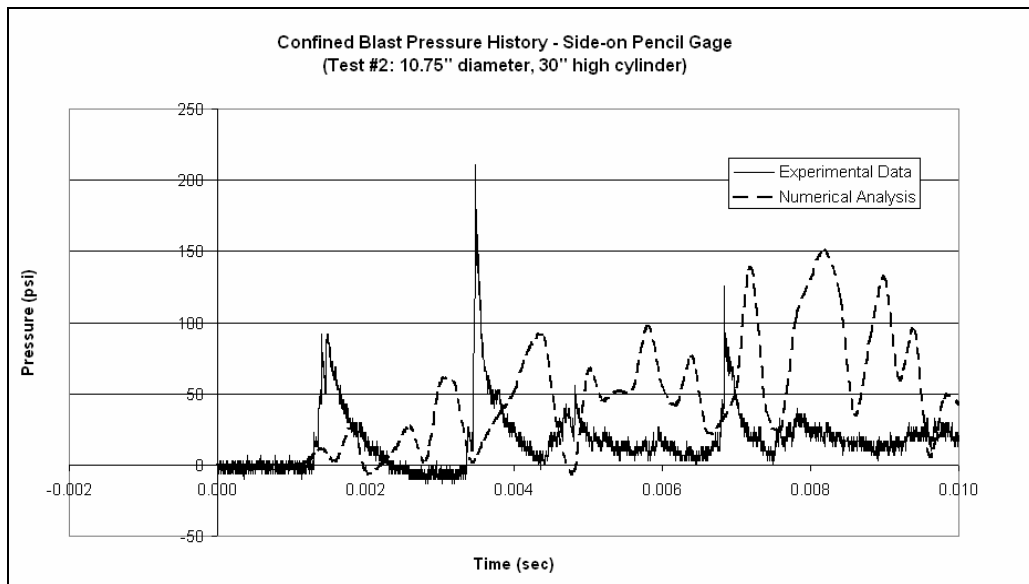


Figure 8.28. Pressure history comparison, side-on gage.

Figure 8.29, compares the overpressure profiles for the plate center. While the total impulse is nearly equivalent over the entire 10 msec, the time of arrival, oscillation pattern, duration of peak overpressures, etc vary greatly. As stated previously, the FEA may have some numerical error for this highly complex confined blast environment based on the fluid turbidity (not addressed in this study) exacerbated by the close proximity of the structures. Additionally, in the laboratory environment the movement of the pressure gages into the chamber wall and plate may also have contributed to the lower recorded overpressure values and additional noise

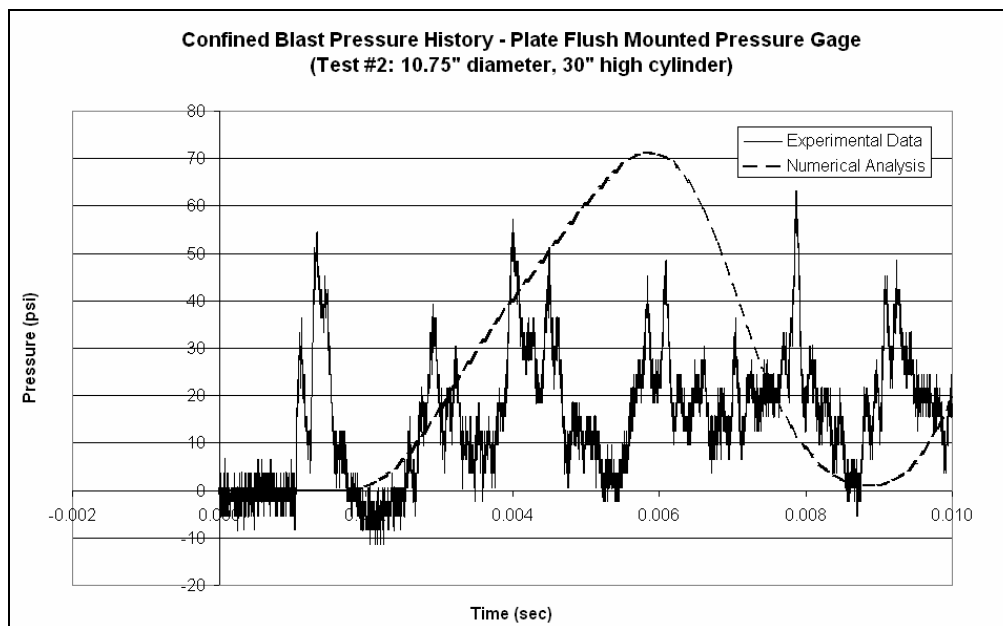


Figure 8.29. Pressure history comparison, plate center.

Furthermore, the peak overpressure profiles do not have the shock wave patterns as evident in the experimental results. The profiles are more rounded, bell-shaped versus the triangular profiles seen in the experimental results. The author found the 1/8th symmetric models demonstrated this phenomenon unexplainably.

Therefore, when possible, simulations should be conducted as full models with particular attention given to the shape of the overpressure profile.

Lastly, the final deformation of the cylinders was compared. Experimental measurements of the 30 in cylinder found the greatest deformation was 10.8 mm increase in diameter measured at 4 mm above center. The numerical analysis was terminated at 10 msec; the final deformation of the cylinder was not reached in this time. The numerical analysis diameter had increased by 7 mm at 10 msec at the exact center.

8.5 Conclusion

Two experimental tests of 10.75 in diameter schedule 5s cylinders of 15 in (Test #1) and 30 in (Test #2) heights were conducted with an explosive enclosed with a chamber fitted with two 150 lb hanging plates. The chamber door was blown off during the 15 in cylinder experiment. However, despite losing the door during experimental Test #1, initial peak overpressure recorded on the chamber wall was 55 psi compared to Test #2's initial peak overpressure of 35 psi. Initial peak overpressure recorded on the plate was 60 psi compared to Test #2's initial peak overpressure of 37 psi. These peaks all occurred within the first two milliseconds of the blast event. Therefore, even with a very large vent, in this case one entire wall, very high peak overpressures still occurred. Moreover, the loss of the door brings attention to the risks of structurally weak partitions within the existing vehicle hull design and the overall influence of boundary conditions on the total system performance during confined blast. Connecting the mitigation cylinder to a direct-to-

outside vent may further reduce overpressures within the chamber, but must be carefully constructed to prevent increasing the vehicle hull's external vulnerability.

The 30 in high compartment experimental values correspond in time of arrival and moderately correspond in overpressure history pattern to those calculated in the FEA for the chamber wall. Dissimilarity between the side-on gage and chamber wall FEA and experimental overpressure plots may be attributed to the modeling limitations of the complex, turbulent shock wave front, the experimental gage stand movement, and/or FEM symmetry unresolved errors. The peak overpressure profiles do not have the shock wave patterns as evident in the experimental results. The profiles are more rounded, bell-shaped versus the triangular profiles seen in the experimental results. The author found the 1/8th symmetric models demonstrated this phenomenon unexplainably. Therefore, when possible, simulations should be conducted as full models with particular attention given to the shape of the overpressure profile.

Chapter 9: Introduction of “Blast-Test” Dummy

Human survivability drastically decreases for an explosive event when the explosion occurs within a confined space. In this restrictive environment blast overpressures reflect and magnify with detrimental effects. The effects of blast mitigation must be examined to fully understand the appropriate design required to protect personnel and equipment located within a confined area. As shown in previous chapters, compartment performance alone is not an adequate indicator of the compartment’s mitigation abilities to protect structures or occupants within the confined space.

Human blast lethality depends on many factors. This study limits the injury criteria to head and chest accelerations as discussed in Chapter 3. It is important to note that while head and chest acceleration may be below the tolerance levels, high temperatures, toxic fumes, rupturing of critical arteries, crushing of bones and impalement from shrapnel and other debris can cause life threatening injuries along with many other fatal blast phenomenon. At the time of this study, the numerical dummy and FEA were not capable of measuring these more advanced and refined injuries. A calibrated direct blast-test dummy does not currently exist. Blast laboratory testing is restricted to simplified structures (150 lb steel plates, see previous chapters) due to the expensive and precarious nature of data acquisition dummies. Therefore, FEA provides a quick, relatively inexpensive opportunity to study confined blast on a dummy occupant.

For this analysis modifications were made to the HYBRID III – 50th percentile rigid dummy; see Chapter 4 for specific details. Four scenarios were examined:

dummy subjected to unmitigated free field blast, dummy subjected to mitigated free field blast, dummy subjected to unmitigated confined blast and dummy subjected to mitigated confined blast. The mitigation compartment used is this FEA the same 10.75 in diameter, 30 in high, schedule 5s mild steel tube as previously modeled and experimental tested in Chapters 7 and 8.

The goal of this study was to introduce and examine the use of a FEM blast-test dummy in free field and confined blast environments.

9.1 Numerical Model

The ALE mesh is comprised of a centrally located cubic HE, with a gradually decreasing air mesh density radiating outward from charge center, see Figure 9.1. At the time of this study a new ALE mesh transition tool debuted in the eta/VPG modeling software. Therefore, the shape of the charge was changed from the previously used spherical shape to cubic shape to take advantage of this tool and maintain uniform sized elements and smooth mesh transition zones. The mesh transition zone maintained a uniform element dimension extending to encompass the cylinder and the left half of the dummy model. The mesh density decreased past this transition zone as it extended out to the domain edges containing the entire chamber structure. No symmetry was used. Total run time (39 – 56 hrs) was greatly reduced using this mesh transition zone for optimized mesh densities. This dummy study is numerical only, therefore, a cubic shaped HE was permissible without experimental equivalent concerns.

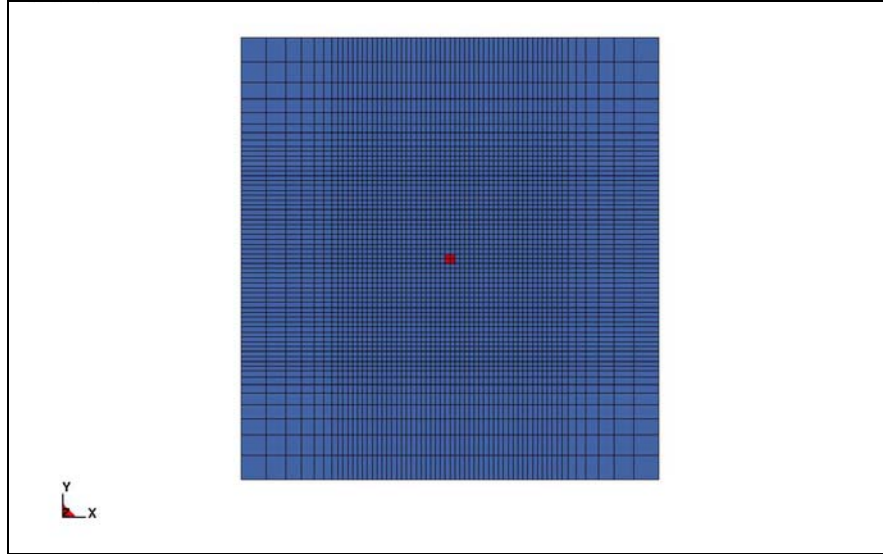


Figure 9.1. ALE mesh section cut of cubic charge.

Four FEM, see Figures 9.2-5, were developed to compare the effects of confinement and mitigation on head and chest accelerations. The first model consists of a free field explosive event of the dummy and the HE. The second model is identical to the first with the inclusion of the 10.75 in diameter, 30 in high, schedule 5s mild steel mitigation compartment surrounding the HE. The cylinder is tubular in design with an open top and bottom. The third and four models follow the preceding two models but enclosing the dummy, HE and cylinder within a ½ in thick RHA confinement chamber with overall interior dimensions of 6 ft x 5 ft x 4.5 ft.

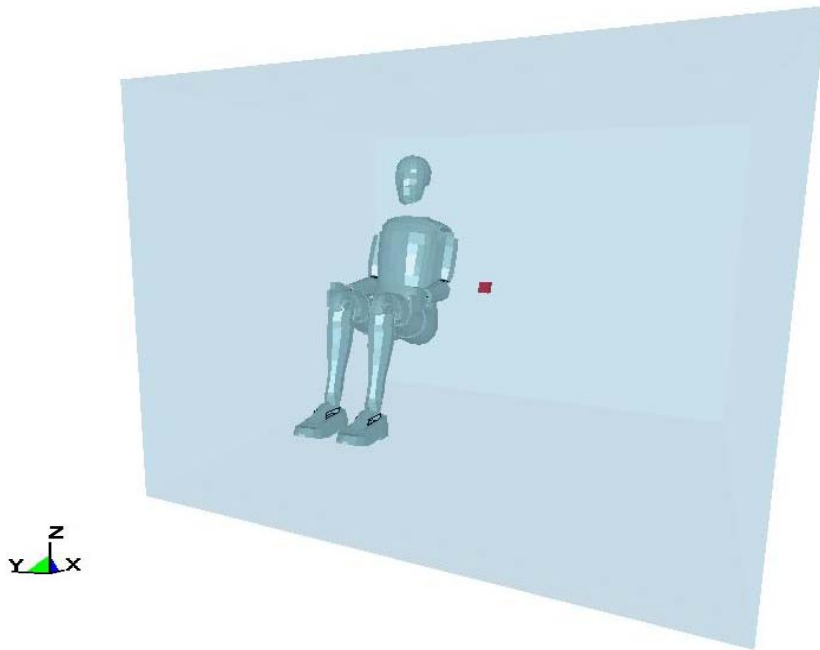


Figure 9.2. Model 1: Dummy free field blast, unmitigated.

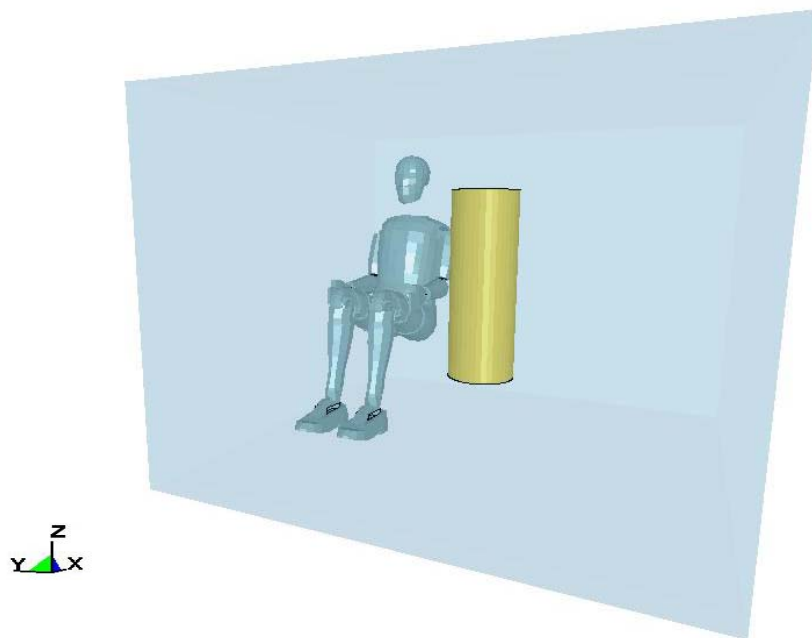


Figure 9.3. Model 2: Dummy free field blast, mitigated.

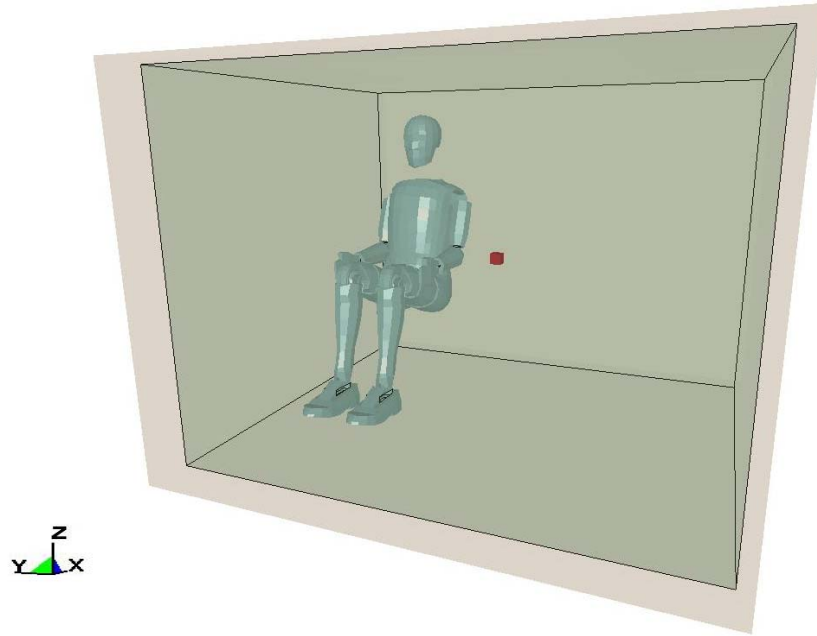


Figure 9.4. Model 3: Dummy confined blast, unmitigated.

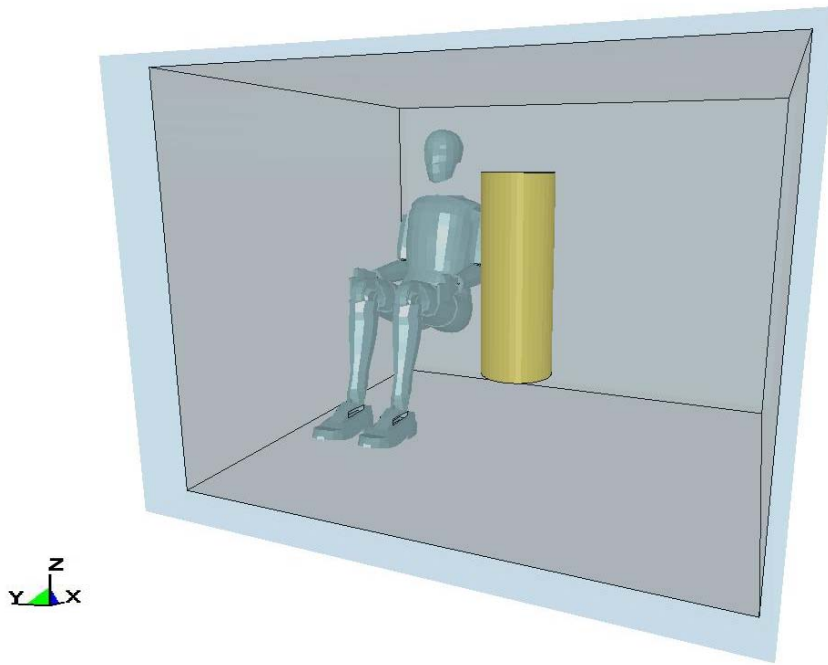


Figure 9.5. Model 4: Dummy confined blast, mitigated.

The seams of the RHA chamber were modeled as continuous material, no weld or bolt failure criteria were used. While this is a manufacturing impossibility, the effects of the confined blast on the chamber were not the focus of this study; the interest is focused on the confined blast effects on the dummy and mitigation compartment. The small access holes cut into the chamber walls for instrumentation wires in the laboratory set-up were not included in the chamber FEM. These small holes and the slight deformation of the chamber door have very little to no effect during the first 20 msec of the blast event.

The Lagrangian elements (cylinder, dummy and chamber) and multi-material ALE elements (HE and air) were coupled using the LS DYNA's penalty-based algorithm `CONSTRAINED_LAGRANGE_IN_SOLID`. The dummy contact was provided by extraction of a null-shell from the surface elements of the dummy model. This null-shell provided the "skin" for the contact definition between the other Lagrangian elements and the HE. HE was modeled as `*MAT_HIGH_EXPLOSIVE_BURN` with the equation of state (EOS) defined as `EOS_JWL`. Air was modeled as `*MAT_NULL` defined by `EOS_LINEAR_POLYNOMIAL`. Chamber was modeled as `*MAT_PLASTIC_KINEMATIC` with the material properties for RHA. Mitigation compartment was modeled as `*MAT_SIMPLIFIED_JOHNSON_COOK` with the material properties for mild steel. Mesh densities for each mitigation compartment are summarized in the Table 9.1.

Air ALE elements had a beginning edge length of 20 mm. HE ALE elements had a max edge element length of 20 mm. The compartment solid elements had an edge length of 20 mm. The chamber walls were modeled as shell elements of ½ inch

thickness with the overall interior dimensions of 6 ft x 5 ft x 4.5 ft. The ALE mesh extended from the center of the charge to at least 100 mm surrounding the chamber. The simulations were terminated after 20 msec, as the initial response of the dummy was adequately demonstrated within this time interval.

ALE	No. Of Nodes	203680
	No. Of Elements	193440 (HE = 8)
	No. Of Materials	2
Chamber	No. Of Nodes	23645
	No. Of Elements	7949
	No. Of Materials	1
Dummy	No. Of Nodes	16330
	No. Of Elements	46481
	No. Of Materials	215
Cylinder	No. Of Nodes	3279
	No. Of Elements	1600
	No. Of Materials	1

Table 9.1. FEM summary of the dummy models

9.2 Dummy Analysis Results

Snapshot views of the mitigated free field and mitigated confined events are shown in Figure 9.6. The chamber quickly reflects and redirects the shock front towards the dummy. The left ankle of the dummy shows clear fracturing in the confined model, this is also apparent in the free field event a few milliseconds later.

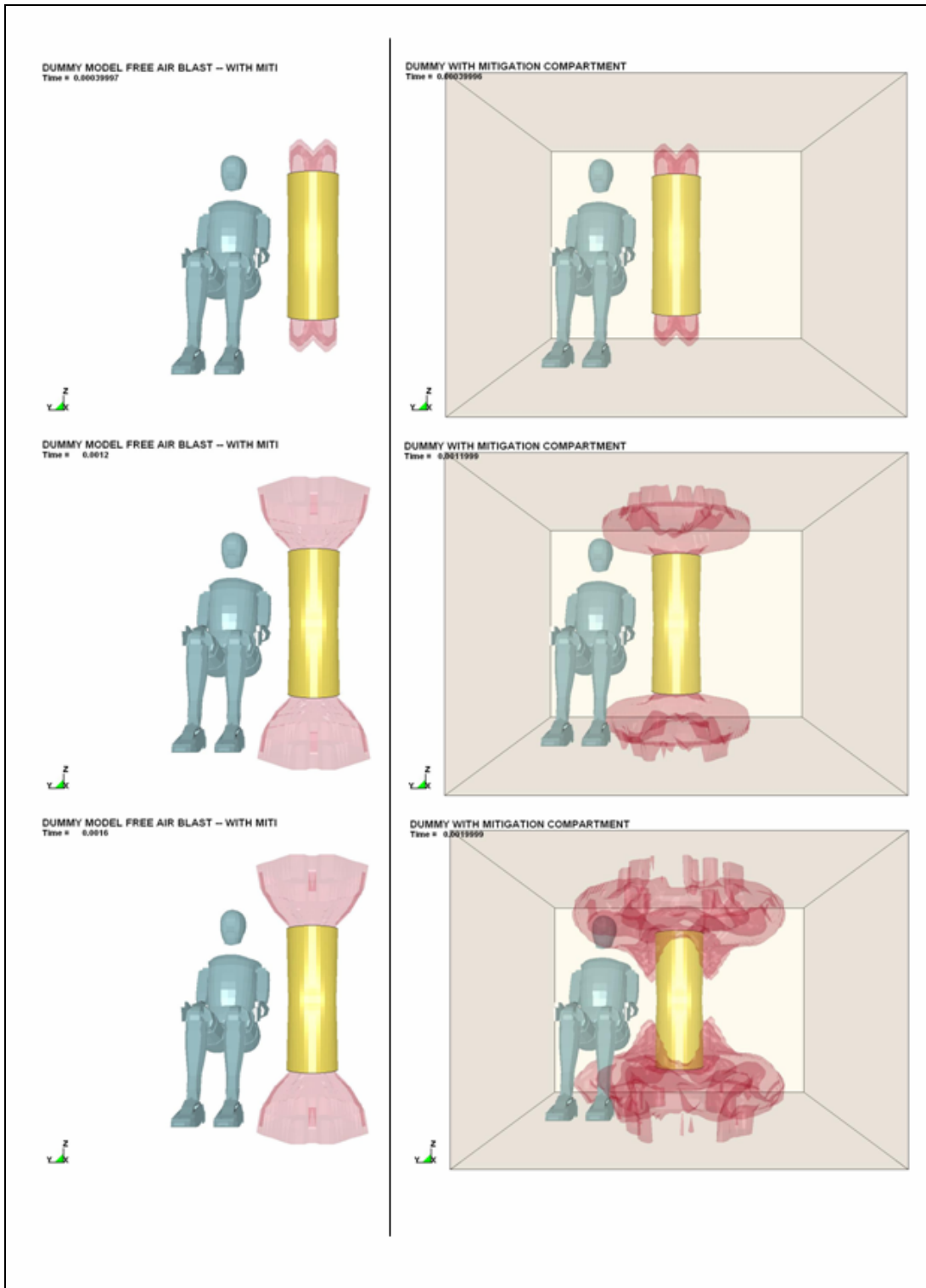


Figure 9.6. Snapshot of mitigated confined dummy and free field dummy events

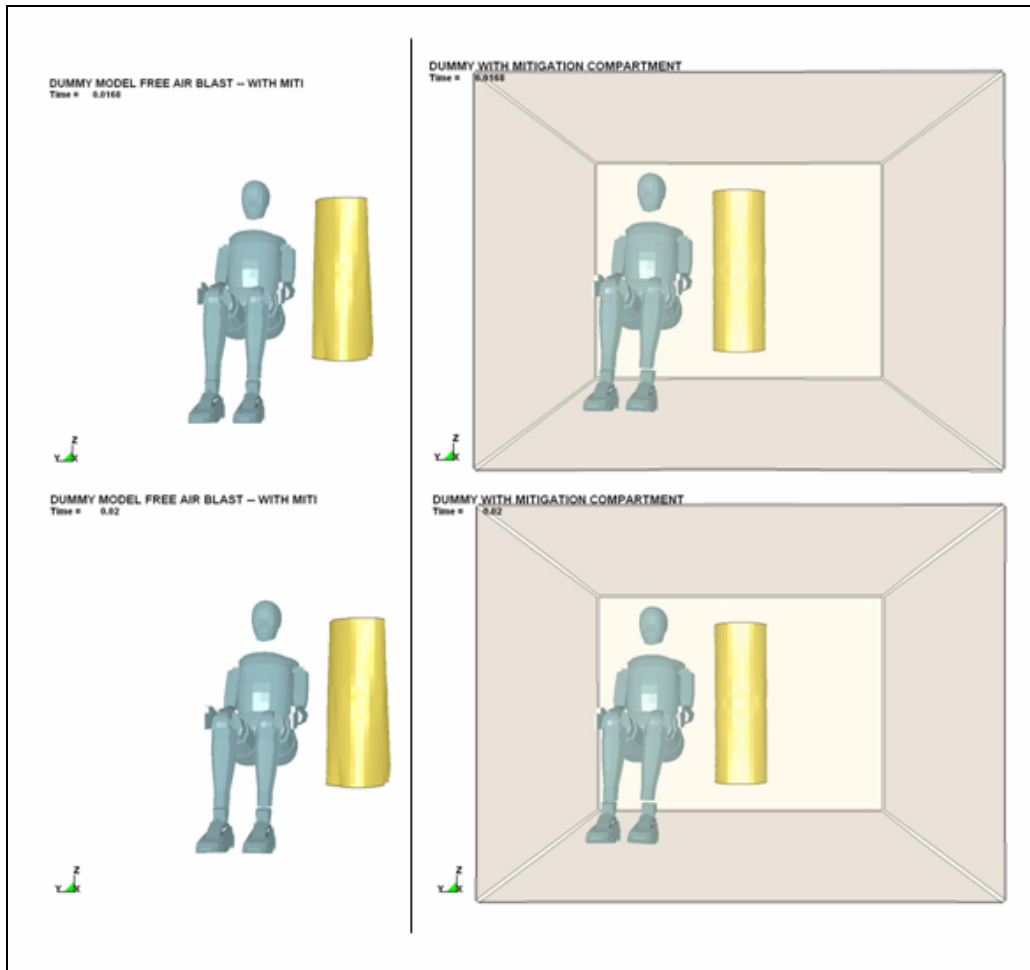


Figure 9.6. (continued)

Table 9.2 provides a key for the figure legends in this section. All head accelerations were below the 150 G injury threshold, see Figures 9.6 and 9.7, as described in Chapter 3. The mitigation compartment insignificantly delays the peak accelerations by approximately one millisecond; duration also remains relatively unchanged. Comparison of the four models shows the highest resultant head accelerations occur during unmitigated blast. In fact, the time of arrival, peak head acceleration and duration are nearly identical in the confined and free field unmitigated events. This is mostly due to the close proximity of the dummy to the HE, as the incident pressure wave impacts the head prior to any reflections or

interactions. Confinement within the chamber creates additional peaks in acceleration as experienced from reflected pressure waves, see Figure 9.7. For the mitigated FEA, the time of arrival is identical for the mitigated free field and mitigated confined blast models. However, the free field is a fourth of the confined peak head acceleration. The use of mitigation significantly reduced accelerations when used in the open environment of free field blast. The use of mitigation within the chamber provided minor reductions in head acceleration, but not as significantly as in the free field blast. If the mitigation cylinder had vented to the outside of the chamber, a more significant drop in head acceleration would most likely occur in the confined blast scenario.

Term	Abbreviation
Free Field	FF
Confined	C
With Mitigation	wM
Ra	Resultant Acceleration
Rx, Ry, Rz	X, Y, Z Acceleration

Table 9.2. Key for dummy result figure legends

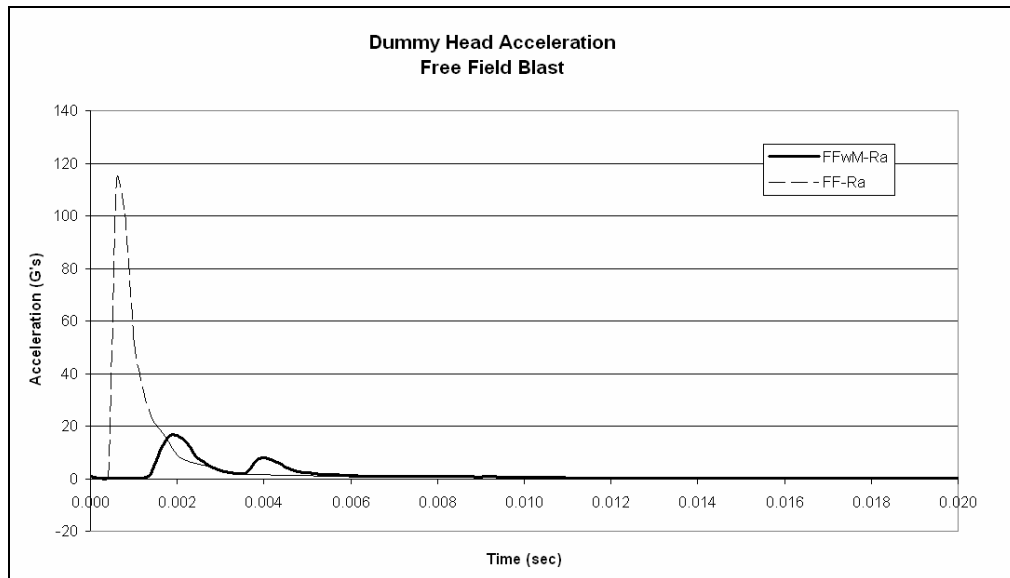
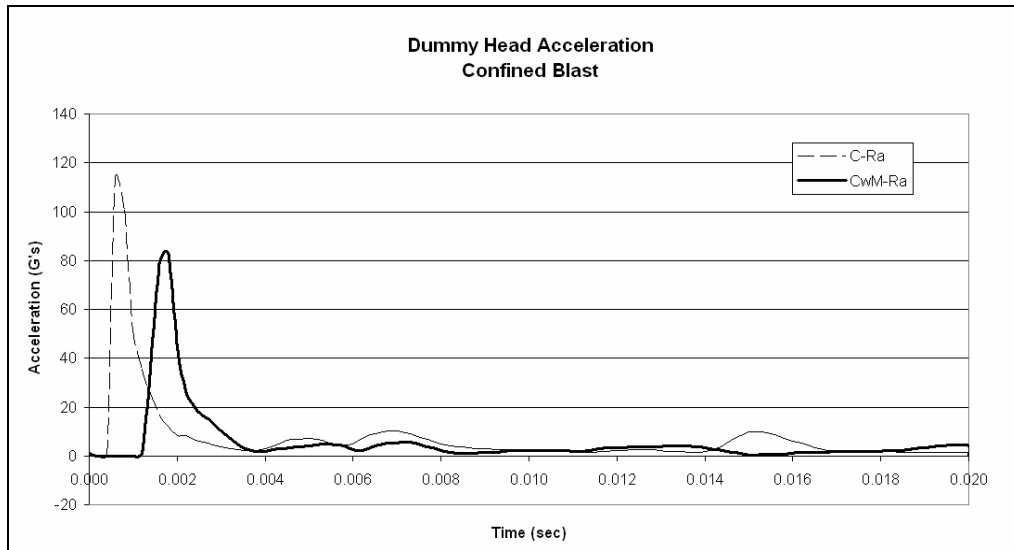


Figure 9.6 Head acceleration, free field blast.



Graph 9.7. Head acceleration, confined blast.

The chest accelerations show large oscillations, attesting to the violent behavior of the shock wave. Figures 9.8-11 show the chest accelerations for each analysis in all three directions. The injury threshold for chest accelerations is 60 G for 3 msec or 40 G for 7 msec. In all four events almost all of the chest acceleration in x, y, or z directions exceeded the injury threshold. The addition of a mitigation compartment provides minimal delay in the arrival of the shock front. Of grave concern is the effect of the mitigation cylinder in increasing acceleration magnitudes and durations both in the free field and confined events. The chest accelerations are significantly increased past 12 msec in the confined chamber. In effect the mitigation structure is providing a channeling effect, allowing the shock front to reflect and magnify numerous times before releasing out into the chamber and impacting the chamber walls and dummy. While the cylinder experiences some deformation, this deformation does not appear to absorb energy significantly enough to reduce chest accelerations.

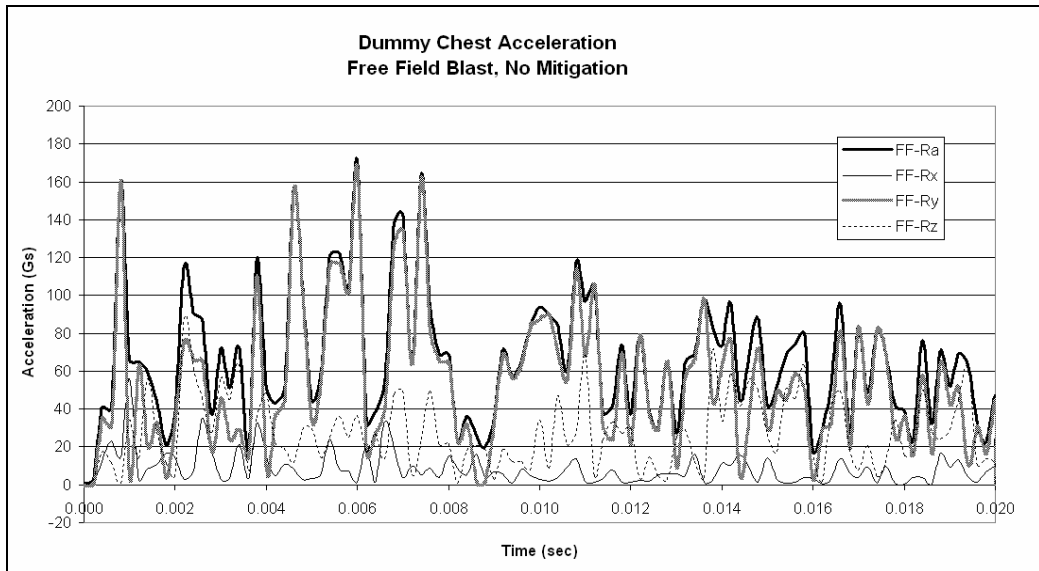


Figure 9.8 Chest acceleration, free field blast, no mitigation.

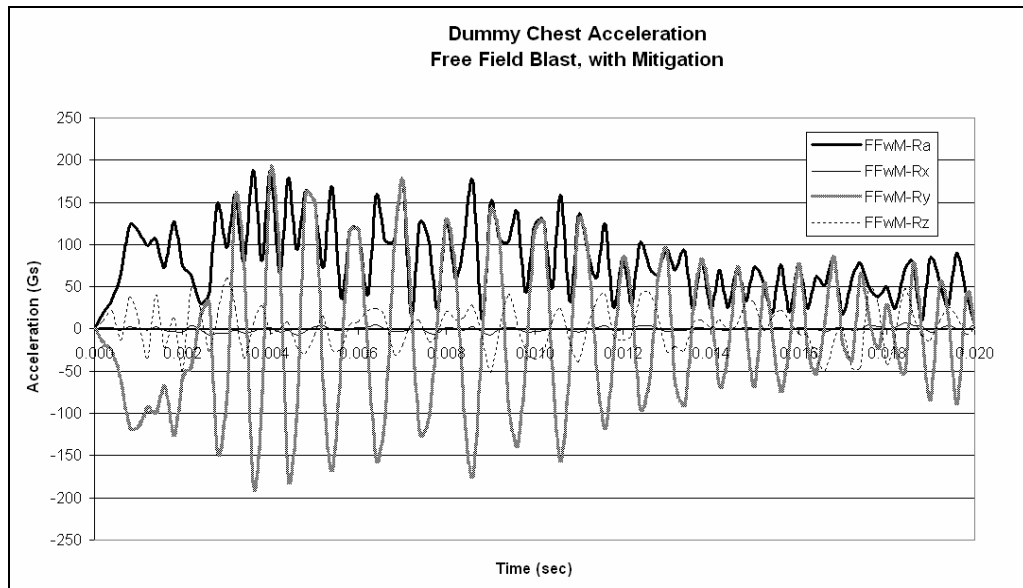


Figure 9.9 Chest acceleration, free field blast, with mitigation.

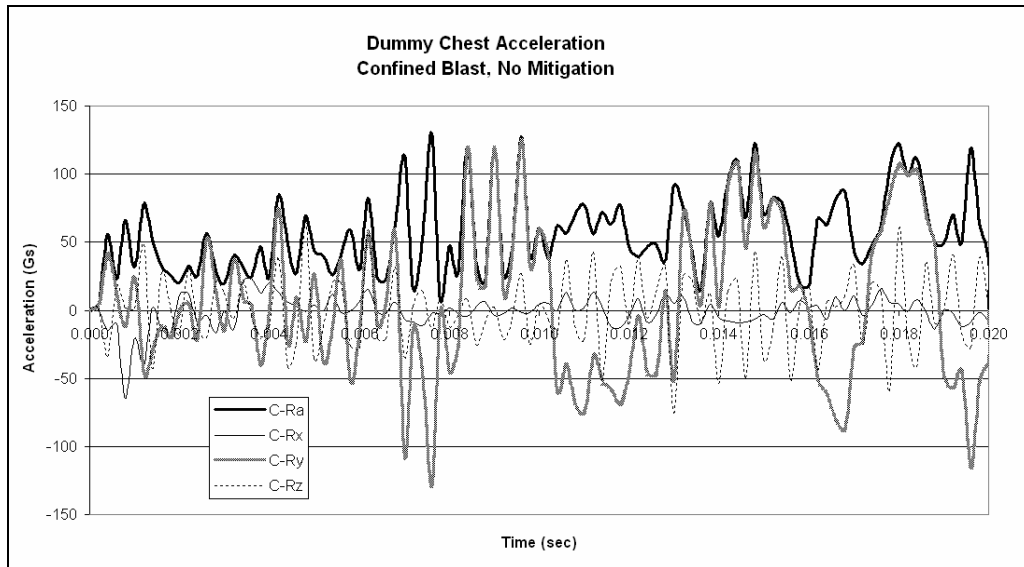


Figure 9.10 Chest acceleration, confined blast, no mitigation.

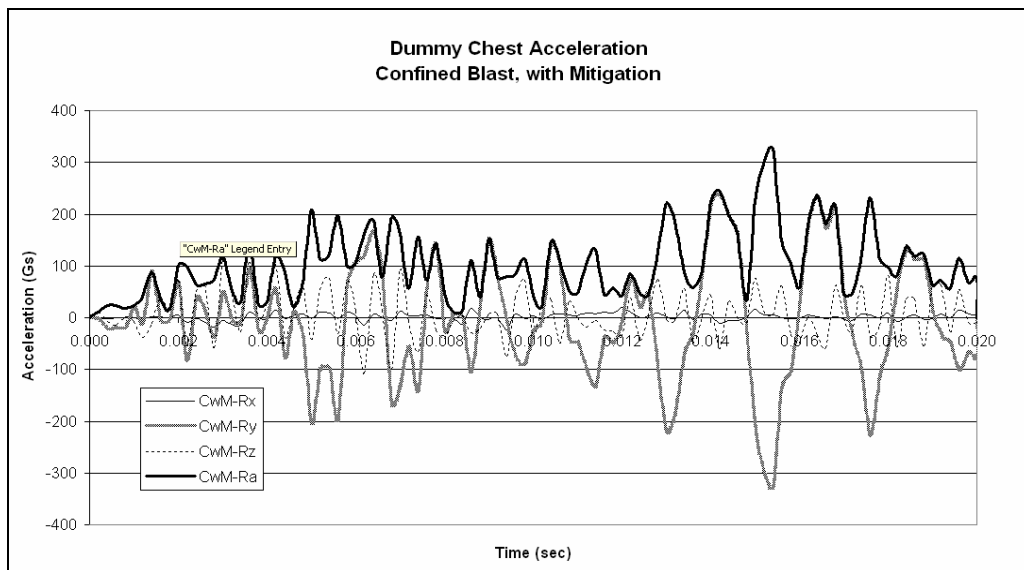


Figure 9.11 Chest acceleration, confined blast, with mitigation.

Chest accelerations for all events were greater than the head accelerations. The variation between the head and chest accelerations is not to be overlooked, as the disastrous effects on the human body from such behavior are surely lethal. Recall from Chapter 4 that the HYBRID III dummy neck is rigid and not designed to withstand lateral blast loads. The lack of oscillations in the head acceleration as

compared to the chest acceleration leads one to investigate that the neck was unable to withstand the shock overpressure and failed.

9.3 Comparison of Dummy and Confined Plate Numerical Results

From the previous numerical analysis presented in Chapter 8, a comparison can be made between the confined blast mitigated dummy and plate events, see Figures 9.12 and 9.13. Note that only one 150 lb dummy is contained within the chamber, versus two 150 lb steel plates.

Figure 9.14 compares the plate's center node, which is approximate to the location of the chest accelerometer, to the dummy's chest acceleration. The accelerations are remarkably similar. Deviation due to the lack of symmetry in the dummy event is evident starting at approximately 6 msec. The reflections off of a second plate would contribute to additional overpressure loadings. The overall behavior of the acceleration of the plate is comparable to that of the dummy. Additional variations of these two events are necessary to draw any clear connection and eliminate the possibility of coincidental findings.

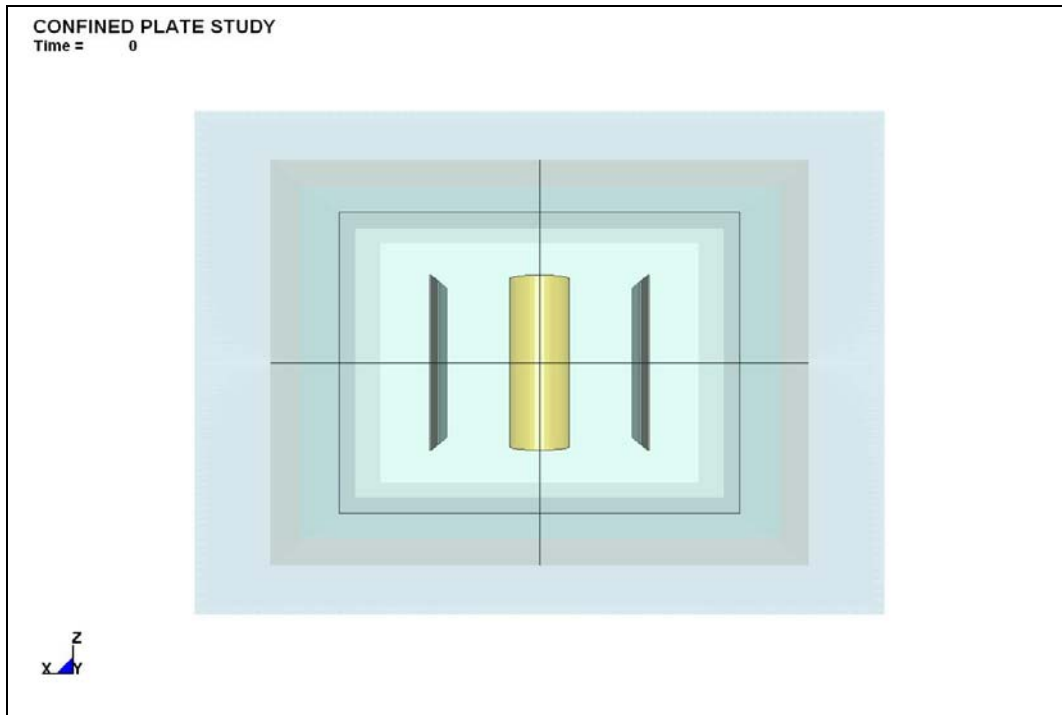


Figure 9.12. Confined blast, mitigation cylinder and plate FEM.

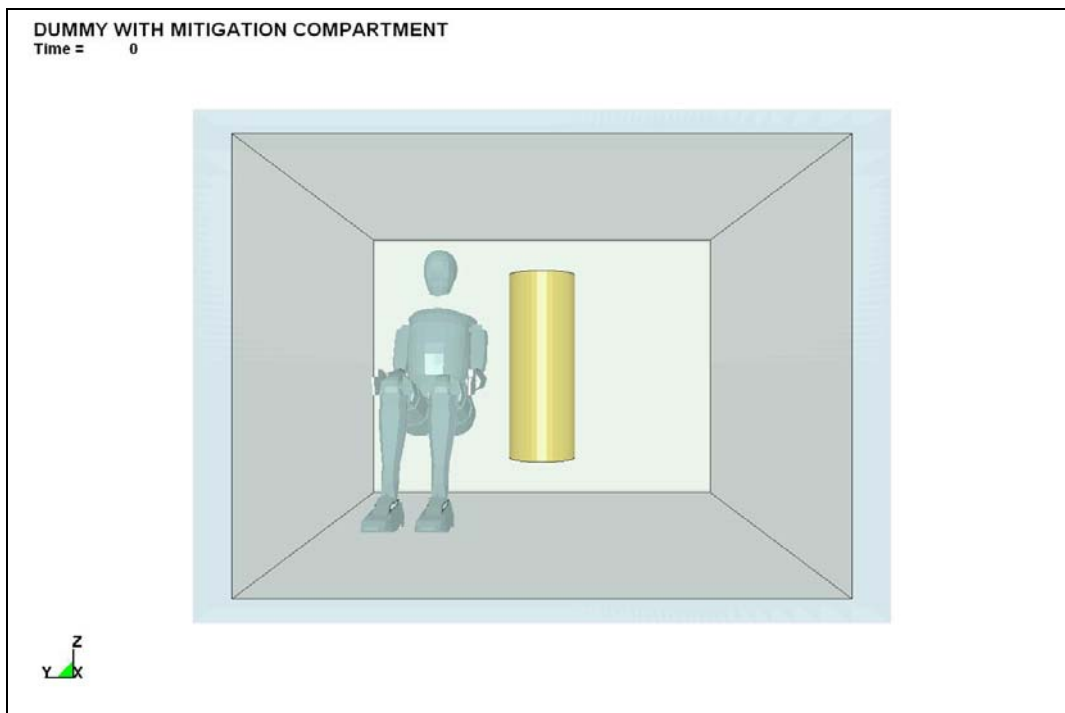


Figure 9.13. Confined blast, mitigation cylinder and dummy FEM.

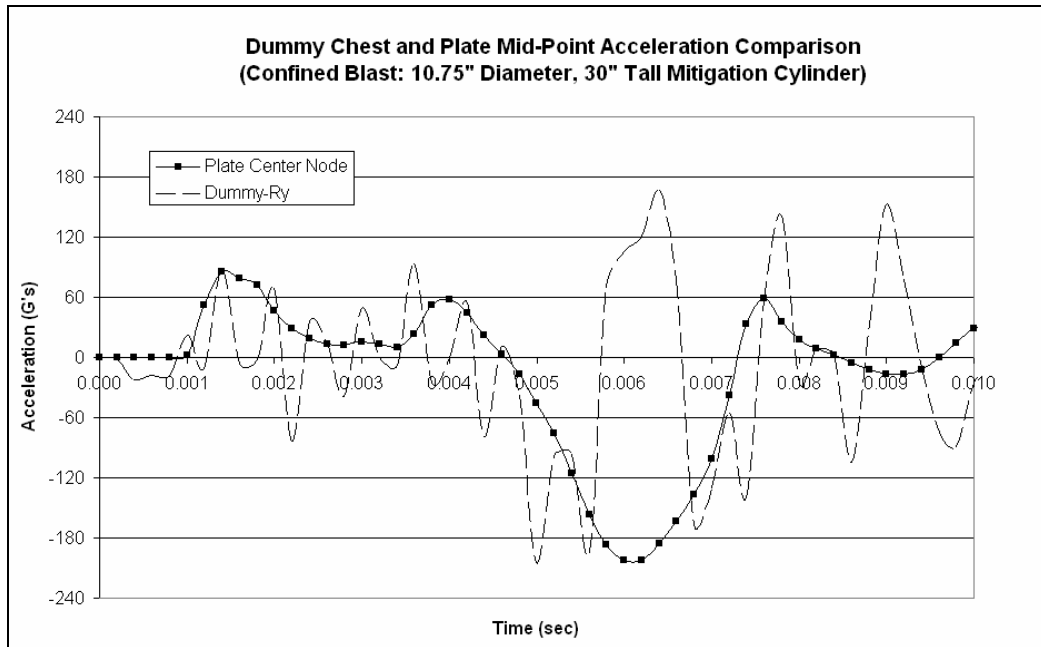


Figure 9.14. Comparison of dummy chest and plate center-node accelerations.

Unlike previous FEA, the new mesh transition modeling tool allowed for optimized mesh densities of this dummy FEM which in turn allowed the full model FEA to run to 20 msec. This additional run-time coupled with the change in the shape of the HE, from spherical to cubic, produced unexpected deformation variances in the mitigation compartment. Figure 9.15 shows the top view of the cylindrical mitigation compartments at 10 msec. The cylinder deformation in the cubic HE free field blast analysis is considerable compared to the other FEA results. This drastic deformation behavior of the cylinder was not seen with the previous FEA free field blast when the charge was spherical, nor in the free field laboratory experiments for the same weight, spherical HE, see Figure 9.16. Part of this behavior may be attributed to the confined environment of the chamber preventing the immediate loss of pressure within the compartment. The free field environment allows for the rapid escape of gases which creates negative pressures. To a greater extent, the ALE mesh and numerical

approximation methods for blast propagation, may be affecting the cylinder response as a direct result of the approximated shock wave front. Due to the limited scope of this study, this curious finding is suggested for additional investigation.

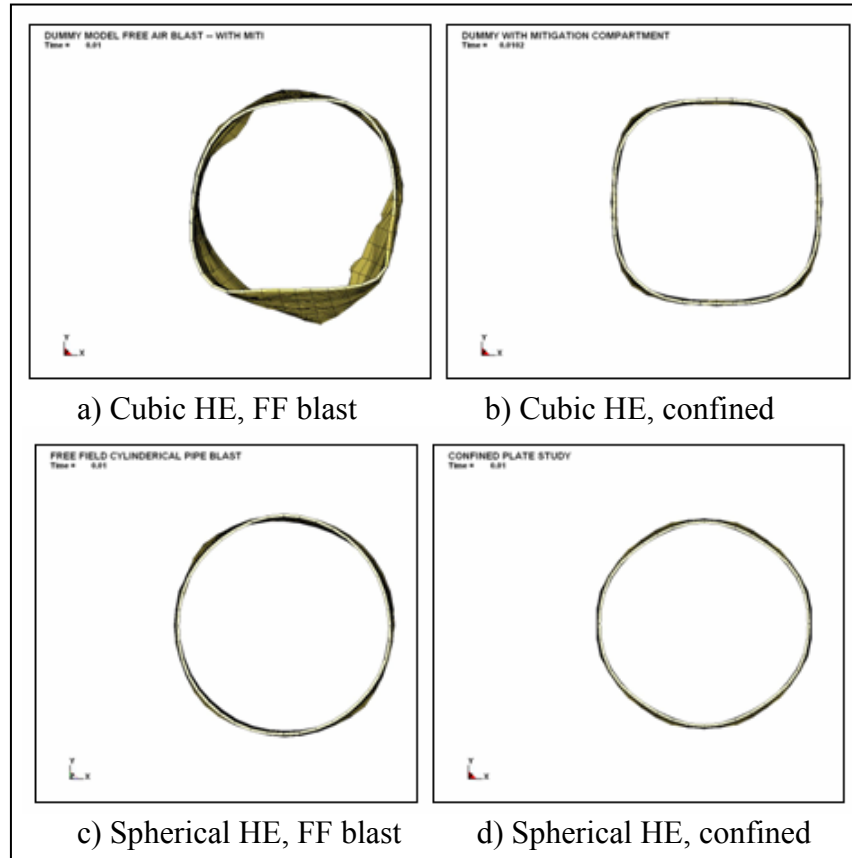


Figure 9.15. Cylinder mitigation compartment deformation at 10 msec.

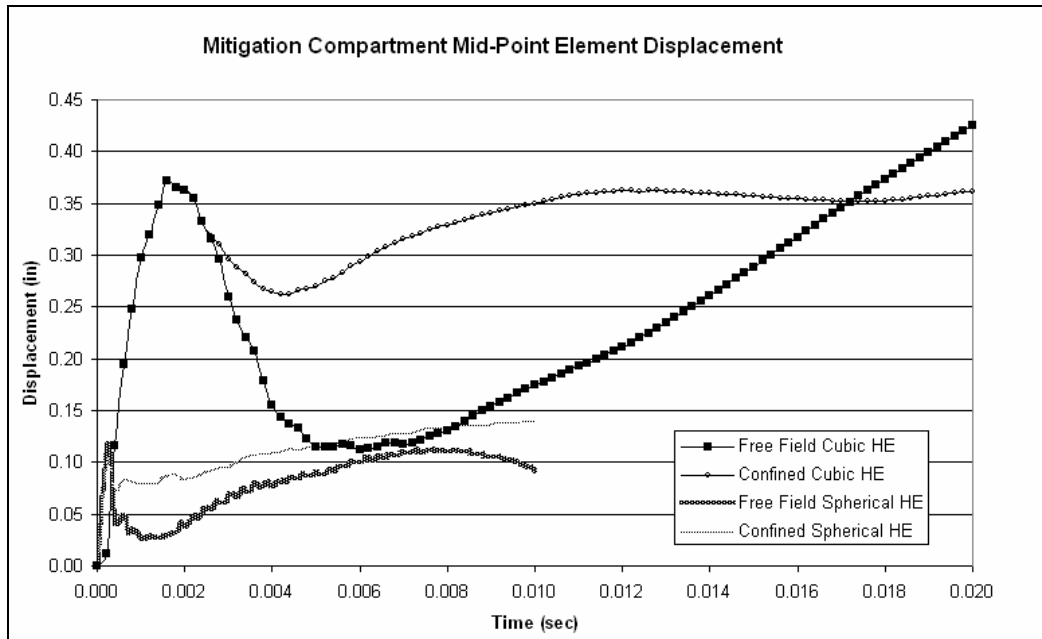


Figure 9.16. Cylinder mitigation compartment deformation.

9.4 Conclusion

The effects of confinement are two-fold on the FEM dummy head and chest accelerations. First, confinement contributes to reflected and magnified overpressures which impinge the dummy and increase accelerations. Secondly, confinement coupled with mitigation can further increase acceleration magnitudes and durations. The mitigation used in this study proved to be counter-intuitive, even if providing increased shielding, as the cylinder effectively became a tunnel and catalyst for increased overpressures and accelerations. While the compartment performance appears satisfactory for reducing head accelerations, chest accelerations were exacerbated. The dummy FEM appears to perform complimentary to the steel plates for confined blast when comparing chest accelerations. The failure of the dummy's neck and ankles calls attention to a more critical injury occurrence despite head or chest accelerations. Thus, with further development, a FEM blast-test

dummy, unlike a flat steel plate, has the potential to estimate other acceleration and overpressure injuries. This FEM dummy provides material for further research for direct blast events. The variations in mitigation compartment deformation due to HE shape and blast environment also require additional investigation beyond the scope of this research.

Chapter 10: Conclusion

The primary objective of this research was to use a robust computational approach to evaluate the confined occupant protective effectiveness of a light-weight mitigation compartment. The secondary objective of this research was to introduce the use of a numerical blast-test dummy.

10.1 Mitigation Compartment Design and Confined Blast Effects

The numerical analysis of cubic, cylindrical and spherical shaped mitigation compartments of equal wall thickness and volume showed compartment geometry has a greater impact on performance than compartment mass for a given size, spherical HE in a one cubic foot volume confined space. The peak pressure locations implied the results were highly dependent on the Eulerian mesh used, as the blast wave propagation through the Cartesian space of air resulted in small numerical approximations. The cubic compartment performed the poorest in energy absorbing capabilities; even while 11 lbs heavier than the best performing spherical compartment. This is most notably because of membrane action and corner effects compounded by reflected and magnified overpressures. The best performing spherical shape is plagued by difficult constructability and awkward shape for inclusion within a vehicle's internal design. The cylindrical geometry moved forward to the next stage of analysis with the focus of the mitigation compartment shifting from "containment" to "shielding" for protective effectiveness. Redirecting and lessening the blast effects, instead of complete enclosure of the HE, was required to achieve appropriate sized recordable effects on surrounding structures during a

laboratory test. Additionally, complete enclosure would be unachievable in a vehicle as access to the munitions stores/magazines would require openings. Numerical analysis showed the cylindrical compartment's wall thickness contributed the greatest to the energy absorption of the mitigation compartment. Most notable is the minimal advantage of doubling the cylinder height to reduce the plate mid-point accelerations. The diameter of the cylinders showed the greatest reduction in accelerations occurred with the combination of taller heights and conservative diameter cylinders. The thickness of the cylinder was more important in reducing accelerations than height. Venting effects also must be considered when comparing the mitigation capabilities of the cylinders, since the larger diameter cylinders allowed more of the initial shock front to escape without impinging the compartment walls. The mitigation performance of a compartment cannot be quantified solely on energy absorbing capabilities. This study showed the energy absorbing potential of the thin walled cylinders to be the greatest; yet, these cylinders performed the least favorable in protecting the plates from high accelerations and overpressures in the prescribed environment. This highlights the necessity to study blast effects on nearby structures and personnel in addition to evaluating the performance of the mitigation compartment itself.

Free field numerical showed the schedule 5s 10.75 in diameter cylinders outperformed the 12.75 in diameter cylinders in energy absorbing performance. This is most likely attributed to the smaller diameter's proximity to the HE, which prohibited a greater percentage of the radiant shock wave front from escaping prior to interacting with the cylinder wall. Note in Table 10.1 the 10.75 in diameter cylinder

walls are slightly thinner comparatively. This difference in wall thickness did not show the large divergence in energy absorbing capacity as found in the earlier numerical analyses for confined blast. The 10.75 in diameter cylinders additionally were much lower in total weight, offering the option of taller shielding heights without large mass increases. Experimental test confirmed the FEA overpressures recorded at the openings of the cylinder could reach nearly double the value as compared to unmitigated blast, thus care is necessary in positioning the mitigation compartment's openings to prevent channeling these large overpressures with detrimental effect. The 10.75 in diameter cylinder was chosen for additional confined blast testing based on its free field blast performance, lightweight and compact shape.

The confined blast FEA of the schedule 5s 10.75 in diameter cylinders resulted in higher accelerations at the mid-point of the 150 lb plate for the shorter 15 in tall (Test #1) when compared to the 30 in tall (Test #2) cylinder. Of concern is the large acceleration witnessed by the plate as calculated in the numerical analysis exceeds the injury thresholds. The plate accelerations are mass dependent; thus the injury thresholds used are for reference and do not predict the type or occurrence of human injury. However, when compared to the dummy model results (note: dummy simulations were run twice as long) the counter-intuitive findings showed higher accelerations for taller shielding heights. Despite losing the door during experimental Test #1, initial peak overpressure recorded on the chamber wall was 55 psi compared to Test #2's initial peak overpressure of 35 psi. Initial peak overpressure recorded on the plate was 60 psi compared to Test #2's initial peak overpressure of 37 psi. These peaks all occurred within the first two milliseconds of the blast event. Therefore,

even with a very large vent, in this case one entire wall, very high peak overpressures still occurred. Moreover, the loss of the door brings attention to the risks of structurally weak partitions within the existing vehicle hull design and the overall influence of boundary conditions on the total system performance during confined blast. Connecting the mitigation cylinder to a direct-to-outside vent may further reduce overpressures within the chamber, but must be carefully constructed to prevent increasing the vehicle hull's external vulnerability. The 30 in high compartment experimental values correspond in time of arrival and moderately correspond in overpressure history pattern to those calculated in the FEA for the chamber wall. Dissimilarity between the side-on gage and chamber wall FEA and experimental overpressure plots may be attributed to the modeling limitations of the complex, turbulent shock wave front, the experimental gage stand movement, and/or FEM symmetry unresolved errors (see the next section).

The dummy FEA of free field and confined blast dummy showed the 10.75 in diameter, 30 in tall mitigation compartment actually increase accelerations for the given size explosive and stand off distance. Thus, the mitigation used in this study proved to be counter-intuitive, even if providing increased blast shielding, as the cylinder effectively became a tunnel and catalyst for increased overpressures and chest accelerations. The compartment performance appears satisfactory for reducing head accelerations, but chest accelerations were exacerbated. The dummy FEM appears to perform complimentary to the steel plates for confined blast when comparing chest accelerations to the plate mid-point. The failure of the dummy's neck and ankles calls attention to a more critical injury occurrence despite head or

chest accelerations. Thus, with further development, a FEM blast-test dummy, unlike a flat steel plate, has the potential to estimate other acceleration and overpressure injuries. The dummy FEA highlighted variations in mitigation compartment deformation due to HE shape and blast environment.

10.2 Numerical Analysis Model and Experimental Correlation

The FEA run times conducted for this research ranged from 36 hrs to over 400 hrs. ALE mesh density and domain size were the greatest contributors to increase runtime. Additionally, it was found that spherical shaped charges presented modeling difficulties in reducing the ALE mesh density while maintaining relatively uniform shaped elements. Towards the end of this research endeavor, eta/VPG introduced a new ALE mesh-transition modeling tool. This tool along with a cubic shaped explosive charge, allowed for smoother, uniform mesh gradients. Therefore, to reduce the runtime for the dummy analysis, cubic shaped charges were used with high mesh densities surrounding the charge and mitigation compartment transitioning to lower mesh densities to the outside of the chamber. The reduction of the ALE mesh was particularly important for the dummy analysis since no symmetry was used to reduce the model size.

In general, the FEMs using symmetry do not have the shock wave patterns as evident in the experimental results. The overpressure profiles are more rounded, bell-shaped versus the triangular profiles seen in the experimental results. The author found the 1/8th symmetric models demonstrated this phenomenon unexplainably. Therefore, when possible, simulations should be conducted as full models with particular attention given to the shape of the overpressure profile. Investigation into

these symmetry effects was not included in the scope of this research. Full models, no symmetry, were attempted for all FEA where possible and particular attention was given to the behavior of the overpressure profiles.

Correlation between the LS DYNA analysis and field tests varied greatly. For the unconfined, free field blast the unobstructed open end of the mitigation compartment resulted in excellent correlation in overpressures. The overpressures positioned normal to the cylinder walls did not align as predicted in the numerical analysis. Two confined blast experimental tests of the 10.75 in diameter schedule 5s cylinders of 15 in and 30 in heights were conducted with spherical HE enclosed with a chamber fitted with two 150 lb hanging plates. During this confined blast the 30 in high compartment experimental values correspond in time of arrival and pressure history pattern to those calculated in the numerical analysis for the chamber wall and side-on pressure gages. The numerical analysis plate flush mounted pressure gage did not follow the pressure oscillation pattern as recorded in the laboratory. The experimental pattern may be attributed to the vibration of the flush mounted pressure gage stand against the plate or the effects of a slightly recessed pressure gage position resulting from the movement of the chamber.

10.3 Further Research

1. Numerical analysis inquiry into symmetry, mesh density and HE shape for uniform mesh transitions effects on correlation and runtime efficiency.
2. Numerical analysis inquiry into HE shape on shock wave propagation and structural loading/deformation.
3. Investigation of connecting one (or both) end(s) of the mitigation cylinder to the outside of the chamber.

4. Inclusion of a witness plate in the free field blast simulation and field tests.
5. Additional full-scale free field and confined blast laboratory tests with varying mitigation compartment design parameters.
6. Examination of additional structural elements within the cylindrical mitigation compartment e.g. baffles or cross beams.
7. Continuation in the development of the FEM blast test dummy.
8. Combined lethality effects of fire and toxic fumes on mitigation compartment performance and human survivability.

Bibliography

- [1] Anderson, C. (1987). "An Overview of the Theory of Hydrocodes." *International Journal of Impact Engineering*, 5, 33-59.
- [2] AGY. (2004). "S-2 Glass Armor Systems." Pub. No. LIT-2004-011
- [3] Alem, N. (1996). "Mine Blast Acceleration Injury Assessment: Methods, Criteria and Software." Report #97-04, USAARL.
- [4] Baker, W. E. (1960). "The elastic-plastic response of thin spherical shells to internal blast loading." *Journal of Applied Mechanics*. 27, 139.
- [5] Baker, W. E. (1973). "Explosions in Air." University of Texas Press, Austin, TX.
- [6] Baker, W. E. et al (1983). "Explosion Hazards and Evaluation." Elsevier, New York.
- [7] Baker, Q., Baker, W. and Spivey, K. (1989). "Blast loading from arrays of parallel line charges." Proc. Of 4th International Symp. On Interaction of Non-nuclear Munitions with Structures. Panama City, FL USA.
- [8] Blanc, G., Adoum, M., and Lapoujade, V. (2004). "External Blast Load on Structures - Empirical Approach." 5th European LS DYNA User's Conference, 5c-39.
- [9] Boh, J., Louca, L., and Choo, Y. (2005). "Energy Absorbing Passive Impact Barrier for Profiled Blastwalls." *International Journal of Impact Engineering*, 31(8), 976-995.
- [10] Bond, A. (2005). "MSc Lecture Notes: Composites." University of Manchester, UK.
- [11] Boyd, M., Marshall, T., Martin, F., and Noesen, S. (1981) "Explosion Pressures in Enclosures Compartmented by Porous Barriers." *International Symposium on Combustion*, 1683-1693.
- [12] Brode, H. (1955). "Numerical Solutions of Spherical Blast Waves." *Journal of Applied Physics*, 26, 766-775.
- [13] Bulson, P. (1997). "Explosive Loading of Engineering Structures." E & FN Spon, New York.
- [14] Burman, N., Saunders, D., Ritzel, D., and Buckland, M. (1993). "Deformation and Fracture of Compartments Subjected to Internal Blast Loading." *National Conference Publication - Institution of Engineers, Australia*, Vol. 2, 93(6), 533-540.

- [15] Cheng, W. and Quan, D. (1998). "Analysis of Munitions Systems Against Blast." ASME PVP (Publication), 377(1), 253-260.
- [16] Chin, E. (1999). "Army Focused Research Team on Functionally Graded Armor Composites." Materials Science & Engineering A: Structural Materials: Properties, Microstructure and Processing, A259(2), 155-161.
- [17] Chin, K., Lim, S., and Stillman, D. (1991). "Simulation of Projectile Penetration into Armor Ceramics." ASME Applied Mechanics Division, 127, 93-98.
- [18] Conventional Weapons Effects Program (ConWep). (1986). "Fundamentals of Protective Design for Conventional Weapons." US Dept of the Army, Technical Manual TM5-855-1.
- [19] Dang, X. and Chan, P. (2006). "Design and Test of a Blast Shield for Boeing 737 Overhead Compartment." Shock and Vibration, 13(6), 629-650.
- [20] Defense Update Online International. (2004) www.defense-update.com/images/armor-concept.jpg
- [21] DeHaan, J., Crowhurst, D., Hoare, D., Bensilum, M., and Shipp, M. (2001). "Deflagrations Involving Stratified Heavier-than-air Vapor/Air Mixtures." Fire Safety Journal, 36(7), 693-710.
- [22] Ellis, R. (1996). "Ballistic Impact Resistance of Graphite Epoxy Composites with Shape Memory Alloy and Extended Chain Polyethylene Spectra™ Hybrid Components." Master of Science in ME, Virginia Polytechnic Institute.
- [23] Esparza, E., Stacy, H., and Wackerle, J. (1996). "Proof Testing of an Explosive Containment Vessel." Los Alamos National Laboratory. 27th DoD Explosives Safety Seminar. 20-22 August 1996.
- [24] "Fire Dynamics Simulator (Version 4) Technical Reference Guide." NIST Special Publication 1018, Jul 2004.
- [25] "Fire Dynamics Simulator (Version 4) User's Guide." NIST Special Publication 1019, Mar 2006.
- [26] "Fire Dynamics Simulator/Smokeview Examples." <http://fire.nist.gov/fds/>, Mar 2005.
- [27] Flannery Associates. (2001). "Introduction to Fire Science Section 1, Unit 4 - Human Behavior and Fire"
- [28] Fredricksson, L. and Nilsson, L. (1994). "An Advanced Finite Element Data Base of the Hybrid III Dummy Phase I – Model Generation and Seld Test Validation." SAE International Congress and Exposition, Detroit.

- [29] Fredricksson, L and Nilsson, L. (1993). "The Hybrid III Dummy Finite Element Model." Structural Dynamics Conference. EURODYN, Trondheim.
- [30] Goodman, H. (1960). "Compiled Free-air Blast Data on Bare Spherical Pentolite." BRL Report 1092, Aberdeen Proving Ground, Maryland.
- [31] Gregory, F. H. (1976). "Analysis of the Loading and Response of a Suppressive Shield when Subjected to an Internal Explosion." Minutes of 17th Explosive Safety Seminar. Denver, Colorado.
- [32] Gupta, R., Yen, C., Bitting, R., Cheeseman, B. and Skaggs, R. (2007). "Evolving Technology: Multi-Phase, Multi-Material, ALE Approach for Buried Mine Blast Simulation." Army Research Laboratory, Aberdeen Proving Ground, ARL-TR-4046-Feb-2007.
- [33] Gupta, R., Yen, C., Bitting, R., Cheeseman, B., Skaggs, R. and McAndrew, B. (2007). "Multiphase, Multimaterial, Arbitrary Lagrangina Eulerian-Based Buried Mine Blast Simulation on a Blast Box Structure." Army Research Laboratory, Aberdeen Proving Ground, ARL-TR-4128-June-2007.
- [34] Gupta, R., Yen, C., Bitting, R., Cheeseman, B. and Skaggs, R. (2007). "Development and Guidelines of an Automated ALE based Multi-Phase, Multi-Material Fluid Structure Interaction Module." Army Research Laboratory, Aberdeen Proving Ground, ARL-TR-4046-Feb-2007.
- [35] Haroldsen, B., Didlake, J., and Stofleth, J. (2003). "Response of the Explosive Destruction System Containment Vessel to Internal Detonations." ASME PVP (Publication), 454, 123-132.
- [36] Held, M. (1999). "Effectiveness Factors for Explosive Reactive Armor Systems." Propellants, Explosives, Pyrotechnics, 24(2), 70-75.
- [37] Hosur, M., Vaidya, U., Haque, A., Kulkarni, M., Kulkarni, R., and Jeelani, S. (1999). "Evaluation of Ballistic Impact Damage of Fiber Reinforced Plastic Laminates Bonded by Polycarbonate Facesheets." ASME Noise Control and Acoustics Division (Publication), 26, 301-312.
- [38] Jacobson, M., Yamane, J., and Brass, J. (1977). "Structural Response to Detonating High-Explosive Projectiles." Journal of Aircraft, 14(8), 816-821.
- [39] Jane's International Defense Review. (2005). "Plasan Sasa offers HMMWV kit." Aug, 2.
- [40] Kim, A., Liu, A., and Crampton, G. (2004). "Explosion suppression of an armoured vehicle crew compartment." Progress in Safety Science and Technology: Proceedings of the 2004 International Symposium on Safety Science and Technology, Vol. 4, 1070-1074.

- [41] Kingery, C., Schumacher, R., and Ewing, W. (1975). "Internal Pressures from Explosions in Suppressive Structures." BRL Interim Memo Report No. 403, Aberdeen Proving Ground, MD. June.
- [42] Kingery, C. and Bulmash, G. (1984). "Airblast Parameters from TNT Spherical Air Burst and Hemispherical Surface Burst." Technical Report ARBRL-TR-02555. AD-B082 713. U.S. Army Ballistic Research Laboratory, Aberdeen Proving Ground, MD. April.
- [43] Kinney, G. and Graham, K. (1985). "Explosive Shocks in Air, 2nd ed." Springer-Verlag, New York.
- [44] Klein, H. and Vander Vorst, M. (2001). "Containment Devices for Small Terrorist Bombs for Law Enforcement, Final Report." Jaycor Report J4039-99-100.
- [45] Koh, C., Ang, K., and Chan, P. (2003). "Dynamic Analysis of Shell Structures with Application to Blast Resistant Doors." Shock and Vibration, 10(4), 269-279.
- [46] Koppert, J. and Beukers, A. (2000). "Full Composite Isotensoid Pressure Vessels or How Composites Can Compete with Steel." SAMPE Journal, 36(6), 8-16.
- [47] Kotzialis, C., Derdas, C., and Kostopoulos, V. (2005). "Blast Behavior of Plates with Sacrificial Cladding." 5th GRACM International Congress on Computational Mechanics, Limassol.
- [48] Langdon, G., Lemanski, S., Nurick, G., Simmons, M., Cantwell, W., and Schleyer, G. (2007). "Behaviour of Fibre-metal Laminates Subjected to Localized Blast Loading: Part I-Experimental Observations." International Journal of Impact Engineering, 34(7), 1202-1222.
- [49] Langdon, G., Lemanski, S., Nurick, G., Simmons, M., Cantwell, W., and Schleyer, G. (2007). "Behaviour of Fibre-metal Laminates Subjected to Localized Blast Loading: Part II-Quantitative Analysis." International Journal of Impact Engineering, 34(7), 1223-1245.
- [50] LeBlanc, G., Adoum, M., and Lapoujade, V. "External blast load on structures – Empirical approach." 5th European LS-DYNA Users Conference, 5c-39.
- [51] Lee, D. and O'Toole, B. (2004). "Energy Absorbing Sandwich Structures Under Blast Loading." 8th International LS DYNA Users Conference, 8, 13-24.
- [52] Liang, Y., Louca, L., and Hobbs, R. (2007). "Corrugated Panels Under Dynamic Loads." International Journal of Impact Engineering, 34(7), 1185-1201.
- [53] Liang, Y., McMeeking, R. and Evans, A. (2005). "Designs and Simulations of Ballistic-Resistant Metal/Ceramic Sandwich Structures." Ceramic Engineering

- and Science Proceedings, 29th International Conference on Advanced Ceramics and Composites, 26(7), 43-50.
- [54] Louca, L. and Pan, Y. (1998). "Response of Stiffened and Unstiffened Plates Subjected to Blast Loading," *Engineering Structures*, 20, 1079-1086.
- [55] Ma, G. and Ye, Z. (2007). "Analysis of Foam Claddings for Blast Alleviation." *International Journal of Impact Engineering*, 34(1), 60-70.
- [56] Mair, H. (1999). "Review: Hydrocodes for Structural Response to Underwater Explosions." *Journal of Shock and Vibration*, 6, 81-96.
- [57] Morka, A., Kwasniewski, L., and Wekezer, J. (2005). "Assessment of Passenger Security in Paratransit Buses." *Journal of Public Transportation*, 8(4), 47-63.
- [58] Mullin, M. and O'Toole, B. (2004). "Simulation of Energy Absorbing Materials in Blast Loaded Structures." 8th International LS DYNA User's Conference, 8, 67-80.
- [59] Nemat-Nasser, S. and Sarva, S. (2003). "Dynamic Compressive Failure of Alumina under High-velocity Impact." TMS Annual Meeting, *Electron Microscopy: Its Role in Materials Science*, 97-106.
- [60] Nickodemus, G., Erich, D., and Alme, M. (1995). "Effects of Tungsten Alloy Property Variations on Penetrator Performance for Spaced Armors." *Advances in Powder Metallurgy and Particulate Materials*, 3(10), 130-143.
- [61] Norris, C. H., Hansen, R. J., Holley, M. J., Biggs, J. M., Namyet, S., and Minami, J. K. (1959) "Structural Design for Dynamic Loads." McGraw-Hill, New York.
- [62] Novotny, W., Cepas, E., Shakarami, R., Vaziri, R., and Poursartip, A. (2007). "Numerical Investigation of the Ballistic Efficiency of Multi-ply Fabric Armors during the Early Stages of Impact." *International Journal of Impact Engineering*, 34(1), 71-88.
- [63] Ohyagi, S., Nohira, E., Obara, T., Cai, P., and Yoshihashi, T. (2002). "Propagation of Pressure Waves Initiated by Flame and Detonation in a Tube." *JSME International Journal, Series B*, 45(1), 192-200.
- [64] Ozel, T. and Zeren, E. (2006). "Finite Element Modeling the Influence of Edge Roundness on the Stress and Temperature Fields Induced by High-Speed Machining." *Int'l Journal of Advance Manufacturing Technology*.
- [65] Piggott, M. (2007). <http://homepage.mac.com/michaelpiggott>
- [66] "Occupant Crash Protection Handbook for Tactical, Ground Vehicles." Department of the Army, Washington, DC, Nov 2000.

- [67] Qidwai, M. and DeGiorgi, V. (2004). “Numerical Assessment of the Dynamic Behavior of Hybrid Shape Memory Alloy Composite.” *Journal of Smart Material Structures*, 13, 134–145.
- [68] Resonance Publications, Inc. (2007). “The Portal to Science, Engineering and Technology.” <http://www.resonancepub.com/mechanic.htm>
- [69] Robin, M. (2001). “FM-200: Theory of Fire Extinguishment.” Great Lakes Chemical Corporation Technical Information, <http://www.fm-200.com>.
- [70] Rupert, N., and Schoon, R. (1993). “Evaluation of High-density Ceramics for Ballistic Applications.” National Conference Publication - Institution of Engineers, Australia, 93(1), 199-205.
- [71] Sachs, R. (1944). “The Dependence of Blast on Ambient Pressure and Temperature.” BRL report 466. Aberdeen Proving Ground, Maryland.
- [72] Savage, S. (2004). “Defense Application of Nanocomposite Materials.” FOI – Swedish Defense Research Agency, User Report, Dec, FOI-R-1456-SE.
- [73] Smith, P., Mays, G., Rose, K., Teo, K., and Roberts, T. (1992). “Small Scale Models of Complex Geometry for Blast Overpressure Assessment.” *International Journal of Impact Engineering*, 12(3), 345-360.
- [74] Souli, M. Ouahsine, A. and Lewin, L. (2000). “Arbitrary Lagrangian Eulerian Formulation for Fluid-Structure Interaction Problems.” *Computer Methods in Applied Mechanics and Engineering*, 190, 659-675.
- [75] Sriram, R. and Vaidya, U. (2004). “Blast Impact on Aluminum Foam Composite Sandwich Panels.” 8th International LS DYNA User’s Conference, 14, 29-38.
- [76] Stiff, P. (1986). “Taming the Landmine.” Galago, Alberton, RSA.
- [77] Stoll, A. (1967). “The Role of Skin in Heat Transfer.” *Advances in Heat Transfer*, 4, 115–141.
- [78] Stoll, A. and Greene, L.. (1959). “Relationship between Pain and Tissue Damage due to Thermal Radiation.” *Journal of Applied Physiology*, 14, 373–383.
- [79] Tabiei, A. and Nilakantan, G. (2007). “Reduction of Acceleration Induced Injuries from Mine Blasts under Infantry Vehicles.” Department of Aerospace Engineering and Engineering Mechanics, University of Cincinnati, OH. atabiei@aol.com.
- [80] Tabiei, A. (2006). “Dummy Modeling in LS-DYNA – Course Notes.” Department of Aerospace Engineering and Engineering Mechanics, University of Cincinnati, OH. atabiei@aol.com.

- [81] Tedesco, J., McDougal, W. and Ross, A. (1999). "Structural Dynamics." Addison-Wesley, Menlo Park, CA.
- [82] Theobald, M. and Nurick, G. (2007). "Numerical Investigation of the Response of Sandwich-type Panels Using Thin-walled Tubes Subject to Blast Loads." *International Journal of Impact Engineering*, 34(1), 134-156.
- [83] Valdevit, L., Wei, Z., Mercer, C., Zok, F., and Evans, A. (2006). "Structural Performance of Near-optimal Sandwich Panels with Corrugated Cores." *International Journal of Solids and Structures*, 43(16), 4888-4905.
- [84] Wieczorek, C. and Dembsey, N. (2001). "Human Variability Correction Factors for Use with Simplified Engineering Tools for Predicting Pain and Second Degree Skin Burns." *Journal of Fire Protection Engineering*, 11(2), 88-111.
- [85] Williams, K., McClennen, S., Durocher, R., St-Jean, B, and Tremblay, J. (2003). "Validation of Loading Model for Simulating Blast Mine Effects on Armored Vehicles" 7th International LS DYNA User's Conference, 6, 35-44.
- [86] White, J., Trott, B., and Backofen, J. (1977). "The Physics of Explosion Containment." *Physics in Technology*. May, 94-100.
- [87] Yiannakopoulos, G. and Kiernan, P. (1999). "Pressure Transducer Mounts for Internal Blast Measurements on Thin Metal Walls." *Journal of American Institute of Physics*, 70(4), 2122-2126.
- [88] Zhao, H., Elnasri, I., and Girard, Y. (2007). "Perforation of Aluminum Foam Core Sandwich Panels Under Impact Loading - An Experimental Study." *International Journal of Impact Engineering*, 34(7), 1246-1257.
- [89] Zhu, L. (1996). "Transient Deformation Modes of Square Plate Subjected to Explosive Loading." *International Journal of Solids and Structures*. 33, 301-314.
- [90] Zukas, J. (1990). "High Velocity Impact Dynamics." Wiley, New York.
- [91] Zukas, J., Segletes, S., and Furlong, J. (1992). "Hydrocodes Support Visualization of Shock-Wave Phenomena." *Journal of Computers in Physics*, 6, 146-154.
- [92] Zukas, J. and Walters, W. (1998). "Explosive Effects and Applications." Springer-Verlag, New York.
- [93] Zuka, J. (2004). "Introduction to Hydrocodes." Amsterdam: ELSEVIER
- [94] Zyskowski, A., Sochet, I., Mavrot, G., Baily, P., and Renard, J. (2004). "Study of the Explosion Process in a Small Scale Experiment - Structural Loading." *Journal of Loss Prevention in the Process Industries*, 17(4), 291-299.